Chapter 3

Experimental Apparatus

3.1 The Bomb

The bomb is a spherical pressure vessel of internal diameter 160 mm, constructed from stainless steel and rated to 34 bar. It was made for British Gas. It was originally mounted on a drop-rig, which was used by Clarke (1994) to perform experiments in micro-gravity using an earlier vessel. After the preliminary tests with gaseous fuels, the bomb was transferred from the drop-rig to an optical bench, which also provides mounting for all the optics required, valves, vacuum pump, small gas cylinders, electronics including a PC and shelves for storage.

As is shown by the schematic in Figure 3.1, the bomb is constructed in two halves, held together by twelve steel bolts and sealed by a Viton O-ring. The windows are fitted into the bomb and are also sealed by O-rings. End caps bolted into flanges in the bomb hold the windows in. A ring of gasket material and a ring of brass are placed between the windows and the end caps to protect the quartz. As is shown in Figure 3.1, the windows and window end caps can be replaced by a blanking end cap. However, the schlieren system used meant that both windows were required.

The bomb has six fitting ports in the walls of the sphere. Two were used for the electrodes (Section 3.4.1), one for the pressure transducer (Section 3.6.1.2), one for the thermocouple (Section 3.6.2) and two to allow gases in and out of the vessel

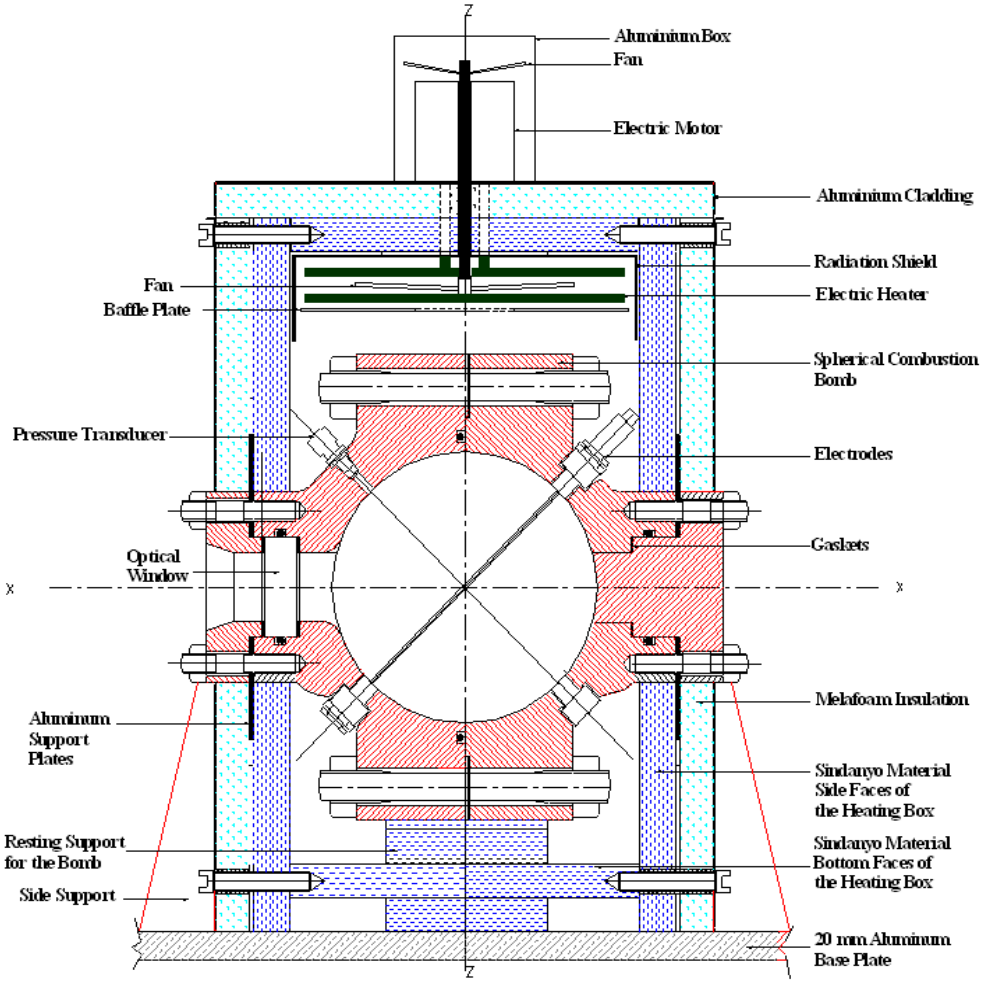

Figure 3.1: Cross-section of the bomb. From Saeed (2002).

(Section 3.3.4).

The bomb was mounted on a curved baseplate which fitted the curvature of the bomb and was bolted down to the optical bench to secure it.

3.2 Gaseous Fuels

For a chosen fuel, equivalence ratio and mixture preparation pressure, the required partial pressure of gaseous fuel can be calculated. For a fuel burned stoichiometrically in air:

$$\mathrm{C}_x\mathrm{H}_y + a\,(\mathrm{O}_2 + \tfrac{79}{21}\,\mathrm{N}_2) \longrightarrow b\,\mathrm{CO}_2 + c\,\mathrm{H}_2\mathrm{O} + a\tfrac{79}{21}\,\mathrm{N}_2 \tag{3.1}$$

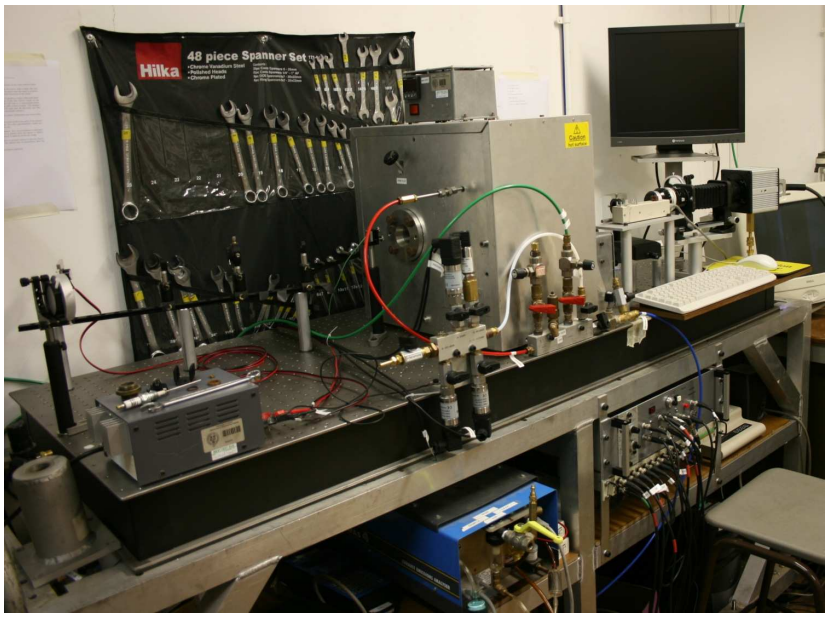

Figure 3.2: The experimental apparatus mounted on an optical bench.

Atom balances give:

$$C_xH_y + (x + \tfrac{y}{4})(O_2 + \tfrac{79}{21}N_2) \longrightarrow x\,CO_2 + \tfrac{y}{2}\,H_2O + (x + \tfrac{y}{4})\tfrac{79}{21}\,N_2 \tag{3.2}$$

Dalton's Law of Partial Pressures tells us that the ratio of the partial pressures of the fuel and the air will be equal to their molar ratio.

$$p_{\mathrm{f}} = \frac{n_{\mathrm{f}}}{n_{\mathrm{air}}} \times p_{\mathrm{air}} \tag{3.3}$$

$$p_{\mathrm{mix}} = p_{\mathrm{f}} + p_{\mathrm{air}} \tag{3.4}$$

$$n_{\mathrm{mix}} = n_{\mathrm{f}} + n_{\mathrm{air}} \tag{3.5}$$

$$p_{\mathrm{f}} = \frac{n_{\mathrm{f}}}{n_{\mathrm{air}}} \times (p_{\mathrm{mix}} - p_{\mathrm{f}}) \tag{3.6}$$

$$= \frac{n_{\mathrm{f}}}{n_{\mathrm{air}}} p_{\mathrm{mix}} - \frac{n_{\mathrm{f}}}{n_{\mathrm{air}}} p_{\mathrm{f}} \tag{3.7}$$

$$p_{\mathrm{f}}(1+\frac{n_{\mathrm{f}}}{n_{\mathrm{air}}}) = \frac{n_{\mathrm{f}}}{n_{\mathrm{air}}} p_{\mathrm{mix}} \tag{3.8}$$

$$p_{\mathrm{f}} = \frac{\left(\frac{n_{\mathrm{f}}}{n_{\mathrm{air}}}\right)}{\left(1+\frac{n_{\mathrm{f}}}{n_{\mathrm{air}}}\right)} p_{\mathrm{mix}} \tag{3.9}$$

$$= \frac{\left(\frac{n_{\mathrm{f}}}{n_{\mathrm{air}}}\right)}{\left(\frac{n_{\mathrm{air}}+n_{\mathrm{f}}}{n_{\mathrm{air}}}\right)} p_{\mathrm{mix}} \tag{3.10}$$

$$= \frac{n_{\mathrm{f}}}{n_{\mathrm{air}}+n_{\mathrm{f}}} p_{\mathrm{mix}} \tag{3.11}$$

For the above hydrocarbon it can be seen that for one mole of fuel:

$$n_{\mathrm{air}} = \left(x+\frac{y}{4}\right)\left(1+\frac{79}{21}\right) \tag{3.12}$$

$$= \frac{100}{21}\left(x+\frac{y}{4}\right) \tag{3.13}$$

$$p_{\mathrm{f}} = \frac{1}{\frac{100}{21}\left(x+\frac{y}{4}\right)+1} p_{\mathrm{mix}} \tag{3.14}$$

For a non-stoichiometric mixture, this is modified to:

$$p_{\mathrm{f}} = \frac{1}{\frac{100}{21\phi}\left(x+\frac{y}{4}\right)+1} p_{\mathrm{mix}} \tag{3.15}$$

So, for a stoichiometric mixture of n-butane (C_4H_{10}) at an initial pressure of 1 bar:

$$p_{\mathrm{f}} = \frac{1}{\frac{100}{21\times 1}\left(4+\frac{10}{4}\right)+1} \times 1 \tag{3.16}$$

$$= 0.0313 \text{ bar}$$

To increase experimental accuracy, p_{mix} is greater than the initial bomb pressure required so that more fuel has to be added and then some of the mixture removed. This reduces the error in the partial pressure of fuel being added, which is far smaller than

the pressure of air used.

This analysis has assumed that the gases have been added slowly so there is no temperature change in the bomb during the filling process. In actuality, any small temperature changes are taken into account, using the approach laid out in Section 3.3.1.2.

3.3 Liquid Fuel Delivery

3.3.1 Volume Calculation

3.3.1.1 Theoretical

The theory of partial pressures could still be used for liquid fuels, provided that all the liquid fuel was evaporated to vapour. However, this would require adding some liquid fuel, waiting for it to evaporate, checking the resultant pressure rise and repeating until the desired increase was observed. This is time consuming. An alternative is to have an external heated chamber in which the mixture can be formed and then transferred to the bomb via a heated line (Farrell et al., 2004). However this requires significant extra equipment. It was preferred to calculate the volume directly from the number of moles required and then to inject that volume of liquid.

$$\mathrm{C}_x\mathrm{H}_y\mathrm{O}_z + \tfrac{1}{\phi}(x + \tfrac{y}{4} - \tfrac{z}{2})(\mathrm{O}_2 + \tfrac{79}{21}\,\mathrm{N}_2) \longrightarrow x\,\mathrm{CO}_2 + \tfrac{y}{2}\,\mathrm{H}_2\mathrm{O} + \tfrac{1}{\phi}(x + \tfrac{y}{4} - \tfrac{z}{2})\tfrac{79}{21}\,\mathrm{N}_2 \quad (3.17)$$

Complete combustion is assumed, but having different products will make no difference, as the following calculations only rely on the ratios of the reactants. Hence for each mole of fuel:

$$n_{\text{air}} = \left(x + \frac{y}{4} - \frac{z}{2}\right)\left(1 + \frac{79}{21}\right)\frac{1}{\phi} \quad (3.18)$$

$$= \frac{100}{21\phi}\left(x + \frac{y}{4} - \frac{z}{2}\right) \quad (3.19)$$

Examining the composition of the whole mixture, including possible residuals:

$$n_{\text{mix}} = n_{\text{air}} + n_{\text{f}} + n_{\text{r}} \tag{3.20}$$

$$= n_{\text{f}} \left[1 + \frac{100}{21\phi} \left(x + \frac{y}{4} - \frac{z}{2} \right) \right] + n_{\text{r}} \tag{3.21}$$

$$n_{\text{f}} = \frac{n_{\text{mix}} - n_{\text{r}}}{1 + \frac{100}{21\phi} \left(x + \frac{y}{4} - \frac{z}{2} \right)} \tag{3.22}$$

The molar residual fraction is defined as:

$$x_{\text{r}} = \frac{n_{\text{r}}}{n_{\text{mix}}} \tag{3.23}$$

$$n_{\text{f}} = \frac{n_{\text{mix}} - x_{\text{r}} n_{\text{mix}}}{1 + \frac{100}{21\phi} \left(x + \frac{y}{4} - \frac{z}{2} \right)} \tag{3.24}$$

$$= \frac{n_{\text{mix}} \left(1 - x_{\text{r}} \right)}{1 + \frac{100}{21\phi} \left(x + \frac{y}{4} - \frac{z}{2} \right)} \tag{3.25}$$

Assuming that the fuel-air-residuals mixture is an ideal gas and T_0 is the required initial temperature for the experiment:

$$n_{\text{mix}} = \frac{p_{\text{mix}} V_{\text{bomb}}}{R_0 T_0} \tag{3.26}$$

$$n_{\text{f}} = \frac{p_{\text{mix}} V_{\text{bomb}} \left(1 - x_{\text{r}} \right)}{R_0 T_0 \left(1 + \frac{100}{21\phi} \left(x + \frac{y}{4} - \frac{z}{2} \right) \right)} \tag{3.27}$$

For the liquid fuel in the syringe:

$$n = \frac{m}{M} \tag{3.28}$$

$$\rho = \frac{m}{V} \tag{3.29}$$

$$V_\mathrm{f} = \frac{n_\mathrm{f} M_\mathrm{f}}{\rho_\mathrm{f}} \tag{3.30}$$

$$= \frac{p_\mathrm{mix} M_\mathrm{f} V_\mathrm{bomb} \left(1 - x_\mathrm{r}\right)}{\rho_\mathrm{f} R_0 T_0 \left(1 + \frac{100}{21\phi}\left(x + \frac{y}{4} - \frac{z}{2}\right)\right)} \tag{3.31}$$

3.3.1.2 Experimental

For the experimental procedure implemented in LabView, each stage uses measurements of the previous stage, rather than assumptions of what should have been done, in order to calculate the target for the next stage. This also allows measurements of actual equivalence ratio and residual fraction. The calculations are also complicated by the fact the air is added in two batches: one before the fuel and one after.

At each stage of the mixture preparation, the ratio of the pressure to the temperature is recorded. This is proportional to the number of moles n. Any residuals left in the bomb have air added to them, then the fuel is injected and finally more air is added:

$$n_1 = n_\mathrm{r} \tag{3.32}$$

$$n_2 = n_\mathrm{r} + n_\mathrm{air1} \tag{3.33}$$

$$n_3 = n_\mathrm{r} + n_\mathrm{air1} + n_\mathrm{f} \tag{3.34}$$

$$n_4 = n_\mathrm{r} + n_\mathrm{air1} + n_\mathrm{f} + n_\mathrm{air2} \tag{3.35}$$

$$= n_\mathrm{mix} \tag{3.36}$$

It is assumed that $T_4 = T_0$, the initial temperature for the experiment, hence:

$$n_4 = \frac{p_{\text{mix}}}{T_0} \tag{3.37}$$

$$\frac{p_{\text{mix}}}{T_0} = n_{\text{r}} + n_{\text{air1}} + n_{\text{f}} + n_{\text{air2}} \tag{3.38}$$

Hence not only is the ratio between n_{r}, n_{air} and n_{f} known, but also the target for their sum.

The number of moles of residuals is the residual mole fraction x_{r} multiplied by the number of moles of mixture.

$$n_{\text{r}} = x_{\text{r}} n_{\text{mix}} \tag{3.39}$$

$$= x_{\text{r}} \frac{p_{\text{mix}}}{T_0} \tag{3.40}$$

Hence the choice of mixture pressure, experiment initial temperature and residuals mole fraction gives the operator the number of moles of residuals. The current temperature then yields the partial pressure of residuals required. However the actual number of moles of residuals is recorded by the system. The number of moles of fuel then required can be obtained from the definition of the residuals mole fraction and the ratio between fuel and air from the chemistry.

$$x_{\text{r}} = \frac{n_{\text{r}}}{n_{\text{r}} + n_{\text{air}} + n_{\text{f}}} \tag{3.41}$$

$$x_{\text{r}} \left(n_{\text{r}} + n_{\text{air}} + n_{\text{f}}\right) = n_{\text{r}} \tag{3.42}$$

$$x_{\text{r}} \left(n_{\text{air}} + n_{\text{f}}\right) = n_{\text{r}} \left(1 - x_{\text{r}}\right) \tag{3.43}$$

$$x_{\text{r}} n_{\text{f}} \left(\frac{n_{\text{air}}}{n_{\text{f}}} + 1\right) = \tag{3.44}$$

$$x_{\text{r}} n_{\text{f}} \left(\frac{100}{21\phi} \left(x + \frac{y}{4} - \frac{z}{2}\right) + 1\right) = \tag{3.45}$$

$$n_{\text{f}} = \frac{n_{\text{r}} \left(1 - x_{\text{r}}\right)}{x_{\text{r}} \left(1 + \frac{100}{21\phi} \left(x + \frac{y}{4} - \frac{z}{2}\right)\right)} \tag{3.46}$$

Now the volume of fuel required needs to be calculated from the number of moles. For this it must be considered that the 'n' calculated so far is actually $\frac{p}{T}$, not a true number of moles. In reality, the situation, assuming a fully evaporated fuel acting as an ideal gas is:

$$n_\mathrm{f} = \frac{p'_\mathrm{f} V_\mathrm{bomb}}{R_0 T} \tag{3.47}$$

$$m_\mathrm{f} = n_\mathrm{f} M_\mathrm{f} \tag{3.48}$$

$$= \frac{p'_\mathrm{f} V_\mathrm{bomb} M_\mathrm{f}}{R_0 T} \tag{3.49}$$

where T is the current bomb temperature. In the liquid state in the syringe:

$$\rho_\mathrm{f} = \frac{m_\mathrm{f}}{V_\mathrm{f}} \tag{3.50}$$

$$V_\mathrm{fuel} = \frac{m_\mathrm{f}}{\rho_\mathrm{f}} \tag{3.51}$$

$$= \frac{p'_\mathrm{f} V_\mathrm{bomb} M}{R_0 T \rho_\mathrm{f}} \tag{3.52}$$

Hence the density and molar mass of the fuel is required. These were sourced from Daubert and Danner (1997) in the form of the liquid density Y:

$$Y = \frac{n}{V} \tag{3.53}$$

$$= \frac{\left(\frac{m}{M}\right)}{V} \tag{3.54}$$

$$= \frac{m}{VM} \tag{3.55}$$

$$= \frac{\rho}{M} \tag{3.56}$$

$$V_\mathrm{f} = \frac{p'_\mathrm{f} V_\mathrm{bomb}}{R_0 T Y_\mathrm{f}} \tag{3.57}$$

The advantage of using the correlation for liquid density provided by Daubert and Danner (1997) is that it is temperature dependent, so that if the temperature in the vicinity of the syringe is measured, it can be used to calculate the liquid density rather

than assuming the value given for a standard temperature of 298 K. The temperature in the laboratory does vary, and in addition the syringe will be affected by its proximity to the oven. Calculations show that a temperature deviation of 8 K would lead to a 1% error in density. A second thermocouple was used to measure the local temperature.

Coefficients A to D are defined for each fuel (see Section A.2), and the liquid density is calculated in real time from:

$$Y = \frac{A}{B^{\left(1+\left(1-\frac{T}{C}\right)^{D}\right)}} \tag{3.58}$$

There is the choice of calculating the actual number of moles of fuel either from the partial pressure rise measured during the injection process, or by assuming that all the fuel injected evaporates, and so actual number of moles is made equal to that intended.

$$n_{\text{air}} = \frac{100}{21\phi}\left(x + \frac{y}{4} - \frac{z}{2}\right) n_{\text{f}} \tag{3.59}$$

$$n_{\text{air2}} = \frac{100}{21\phi}\left(x + \frac{y}{4} - \frac{z}{2}\right) n_{\text{f}} - n_{\text{air1}} \tag{3.60}$$

Once the second portion of air has been added, the actual equivalence ratio and residuals mole fraction can be calculated by:

$$\phi = \frac{100}{21}\left(x + \frac{y}{4} - \frac{z}{2}\right) \frac{n_{\text{f}}}{n_{\text{air}}} \tag{3.61}$$

$$x_{\text{r}} = \frac{n_{\text{r}}}{n_{\text{r}} + n_{\text{air1}} + n_{\text{f}} + n_{\text{air2}}} \tag{3.62}$$

Next, two alternative liquid fuel injection systems will be considered: an injector and a syringe.

3.3.2 Injector

In previous work in Oxford (Saeed, 2002), liquid fuels have been injected into the bomb using an automotive electro-magnetic fuel injector. Liquid fuels can only be used in conjunction with the oven, so that they evaporate and form a homogeneous mixture with the air rather than forming liquid puddles in the pipework.

3.3.2.1 Injector Driver Electronics

In order to test this method, the existing injector driver circuit was reworked. It uses a 555 timer in conjunction with a power transistor to produce a voltage pulse of a set length to the injector. The length of the pulse is controlled by an RC circuit, with the resistance set by a multi-turn potentiometer. The capacitors were replaced and the circuit calibrated so that the fifteen turn dial gave the injector pulse duration in milliseconds i.e. 0–15 ms. A switch allowed for a second set of capacitors of the same value to be connected in parallel to double the possible duration up to 30 ms. The driver requires 12 V and a current of about 1 A, so is run off the 10 A power supply used by the ignition system.

3.3.2.2 Fuel Pressurisation

The use of an injector requires the liquid fuel to be pressurised so that when the injector opens the fuel will atomise sufficiently, helping it to evaporate. In a car this would normally be done by a fuel pump, either electrically or mechanically driven. As the fuel should be metered with high repeatability and the pressure varied over a wide range, a pump would require a power supply and pressure regulation of a flammable liquid. It is far easier to pressurise the fuel with a gas, whose pressure can easily be regulated and safely reduced by venting to atmosphere.

The fuel was held in an aluminium container with a feed at the top for pressurising the fuel and feeds at the bottom for fuel exit and draining, both with ball valves controlling the flow. The pressurising gas passes from the cylinder regulator to a sup-

plementary regulator, which vents excess pressure so that the pressure can be reduced without any disconnection of pipes or removal of fuel from the tank.

The choice of gas comes down partly to convenience of what is already available in the laboratory, but also, as the gas and liquid fuel will be in contact under pressure in the tank, it is imperative that the two do not interact in any way to alter the fuel that is injected into the bomb, which could alter the burning velocity. For this reason methane or similar gaseous hydrocarbons were rejected. An obvious choice is nitrogen, as it can be safely vented due to its inert nature. However, there could be concern over its solubility in the liquid fuel, especially as this would be pressure dependent.

Kretschmer et al. (1946) list Ostwald coefficients for nitrogen in iso-octane, one of the fuels under test, from which the percentage mass of dissolved nitrogen in the liquid can be calculated. They define the Ostwald coefficient k as the ratio of the concentration of the gas in the liquid to its concentration in the gas phase. So for a coefficient of one the concentration in mol cm^{-3} or g cm^{-3} of nitrogen would be equal in the nitrogen-only gas phase and the fuel liquid phase. The authors give the coefficient for N_2 at 25°C as being 0.2258. At a gas pressure of 1 atm:

$$\rho_{N_2(g)} = 1.251 \times \frac{273.15}{298.15} \tag{3.63}$$

$$= 1.146 \text{ kg m}^{-3} \tag{3.64}$$

$$\rho_{C_8H_{18}(l)} = 688 \text{ kg m}^{-3} \tag{3.65}$$

$$k = \frac{\rho_{N_2(l)}}{\rho_{N_2(g)}} \tag{3.66}$$

$$\rho_{N_2(l)} = k\rho_{N_2(g)} \tag{3.67}$$

$$= 0.2258 \times 1.146 \tag{3.68}$$

$$= 0.2588 \text{ kg m}^{-3} \tag{3.69}$$

Hence the percentage mass of dissolved N_2 in the iso-octane will be:

$$\frac{0.2588}{688} \times 100 = 0.0376\% \tag{3.70}$$

This was confirmed by reading values off a graph given of log of mole fraction of N_2 against $\frac{1}{T}$.

The relationship between solubility and pressure was investigated by Battino et al. (1984) by providing equations in terms of mole fraction x. For the temperature and pressures ranges 323–453 K and 0.1–0.68 MPa, they give:

$$\ln x = -4.98095 + 0.66840 \ln\left(\frac{T(K)}{100}\right) - 0.0051794P(\text{MPa}) + 0.99000 \ln P \tag{3.71}$$

So at 290 K, 2 barA:

$$x = \exp\left[-4.98095 + \left(0.6684 \times \ln\left(\frac{290}{100}\right)\right) - (0.0051794 \times 0.2) + (0.99 \times \ln 0.2)\right] \tag{3.72}$$

$$= 2.84 \times 10^{-3} \tag{3.73}$$

Converting this to a mass fraction:

$$n = \frac{m}{M_r} \tag{3.74}$$

$$\frac{m_{N_2}}{m_{C_8H_{18}}} = \frac{M_{N_2}}{M_{C_8H_{18}}} \times n \tag{3.75}$$

$$= \frac{2 \times 14.0067}{114.22} \times 2.84 \times 10^{-3} \tag{3.76}$$

$$= 6.97 \times 10^{-4} \tag{3.77}$$

$$= 0.0697\% \tag{3.78}$$

Hence it can be seen that the solubility at these fairly low pressures is roughly linear

with pressure. This makes sense from the definition of the Ostwald coefficient as doubling the pressure will double the gas phase concentration. Hence it is clear that the fuel can be pressurised at a few bar without the percentage mass of N_2 dissolved in the fuel exceeding 0.1%. This was deemed to be perfectly acceptable.

However, there are significant problems with maintaining a constant nitrogen pressure, as most regulators have significant hysteresis. It is also difficult to change between fuels, as the fuel resides in the injector, pipework and fuel tank. For this reasons, a simpler alternative was investigated.

3.3.3 Syringe

It was suggested that a syringe based system may be simpler and more accurate than an injector. The obvious advantage is that it has its own measurement system built-in. The disadvantage is that the fuel will emerge as droplets rather than an atomised spray, so extra care must be taken to ensure complete evaporation.

A ball valve was fitted to the injector port in place of the injector. Onto this valve was fitted a septum made of a disc of PTFE with a 0.83 mm diameter hole drilled in it (see Figure 3.3). In order to inject the fuel into the inner part of the injector boss, which is inside the oven, and hence ensuring evaporation of the fuel, a very long needle was required. Medical spinal needles of length 150 mm were acquired, with a Luer taper fitting. These fitted to Hamilton syringes of volumes 250, 500 and 1000 µl. A kdScientific Model 310 Plus syringe actuator was used to mount the syringes and control the volume and rate of injection. The resolution of the volume injected was 0.1 µl for the 1000 µl syringe and 0.01 µl for the 500 and 250 µl syringes.

The procedure to inject the fuel is to make sure there is no air in the needle and no drops of fuel on the syringe, then insert the needle into the septum, but not as far as the ball valve. Then open the ball valve and push the syringe all the way in. Withdrawing is just the opposite. This ensures that the mixing loop is always sealed. The PTFE wore eventually, especially at high temperatures, and was replaced periodically.

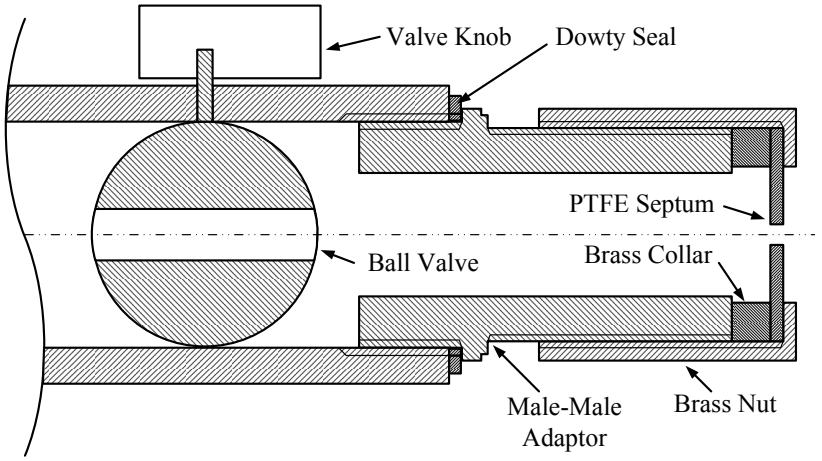

Figure 3.3: Cross-section of septum and ball valve arrangement, which allows injection of fuel into the bomb without leaks.

3.3.4 Pump

A low pressure pump was plumbed in-line with a mixing loop to pump the fuel-air mixture around in order to create a homogeneous mixture (see Figure 3.4). The rest of the time this pump was isolated from the bomb by two valves, so to avoid exposing it to high pressures later on in the process. An extended stem was made for the bomb valve so that it could be operated from outside the oven.

3.3.5 Bomb Volume

The volume of the bomb and various pipework was measured using instruments and data sheets. Although the bomb is a sphere, there are recesses for the windows. The mixing loop is dominated by the boss into which fuel is injected (see Figure 3.3). The volume of the bomb and pipework was 2195 ml and the mixing loop was 54 ml, giving a total of 2249 ml.

The bomb volume was checked using a wet volume flow meter. The volume to be measured was filled with pressurised air and left for the temperature to settle. Then the pressure was reduced by letting air out through the flow meter. The start and end temperatures and pressures were noted. It was found that the temperature did not vary. As the flow meter was wet, the volume reading had to be converted to a

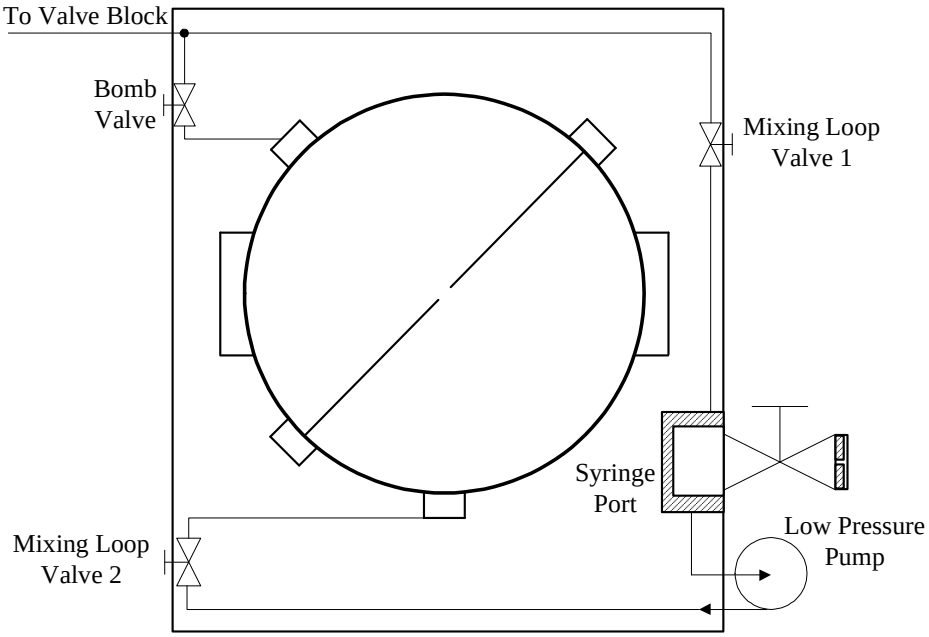

Figure 3.4: Schematic of the mixing loop.

dry volume using the atmospheric pressure and the saturation pressure of water at the temperature measured:

$$V_{\text{dry}} = V_{\text{wet}} \times \frac{p_{\text{atm}} - p_{\text{sat H}_2\text{O}}}{p_{\text{atm}}} \tag{3.79}$$

The isothermal pressure change measured was then used to find the volume of the bomb:

$$V_{\text{bomb}} = \frac{p_{\text{atm}}}{\Delta p} \times V_{\text{dry}} \tag{3.80}$$

The volume of the bomb and the mixing loop was measured as 2268 ml and then 2240 ml. Hence the instrument-measured value of 2249 ml was accepted.

3.4 Ignition

3.4.1 Electrodes

The mixture is ignited by two opposed, co-linear electrodes which form a spark gap in the centre of the sphere. These are sharpened to a point to enhance the electric field at the gap.

Images taken by the high speed camera were checked to ensure that the spark gap

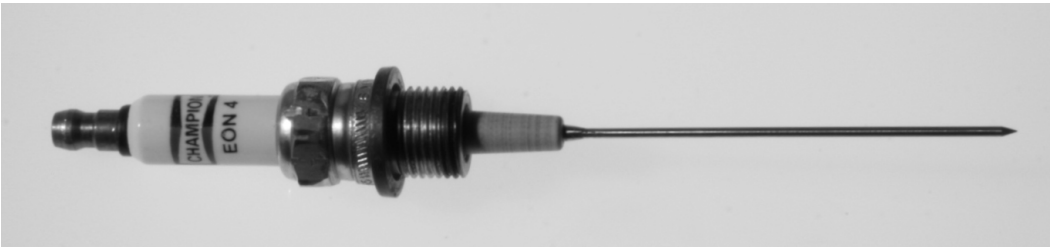

Figure 3.5: Modified spark plug showing reduced thread and extended electrode.

was in the centre of the bomb. For the tests done before the schlieren system was in place, photographs were taken through one window with squared paper behind the other window.

A jig was produced to enable easy manufacture of further electrodes from conventional automotive spark plugs. The normal electrode is removed, most of the thread is machined off and then the spark plug is screwed into one side of the jig. Stainless steel welding rod is placed through a hole on the other side of the jig co-axial with the first and secured by a screw on an intersecting axis. This then holds the plug and rod steady while they are welded together. The tip of the rod is then machined to a point (see Figure 3.5). The plug is sealed by a custom made copper washer. Washers of different thicknesses allow adjustment of the spark gap. The spark gap was set to approximately 1.2 mm.

The environmental chamber was modified so that the spark plug could be removed without removal of the chamber wall, which requires significant dismantling of pipework and optics. To reduce the size of hole required in the chamber wall, small socket size (16 mm) plugs were chosen. Plugs with 1 inch of thread were chosen so that more thread could be removed, increasing the distance from the electrode to the nearest earth and preventing shorting. The inside edge of the hole was also radiused.

The earth electrode is made of a brass section which screws in the bomb wall with a thin stainless steel electrode. The thread provides electrical contact to the bomb, which itself is grounded.

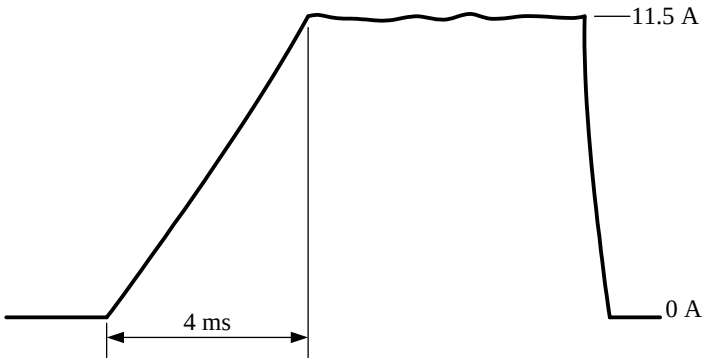

Figure 3.6: Schematic of coil current against time for charging.

3.4.2 Coil

Originally, a conventional Lucas-type inductive HT coil was used to create the spark. However this did not allow the spark energy to be varied easily. It was replaced with a Jaguar coil pack as would be fitted to one cylinder of a gasoline engine. This is triggered by a TTL pulse. The duration of the pulse sets the charging time of the coil pack. This makes it easy to change the spark energy.

The charging current was measured for a long TTL pulse (see Figure 3.6). The coil is modelled as a resistor and an inductor in series. The current in the circuit can be found from:

$$V = IR + L\frac{\mathrm{d}I}{\mathrm{d}t} \tag{3.81}$$

This gives the form of an increase tending exponentially to some asymptote. However, very early in the exponential curve the current is restricted by limiting circuitry in the coil pack. Furthermore, the resistance of the coil is very small. This means that the increase is near-linear before saturating. The energy supplied to the coil is represented by the area under the line, until saturation. After that, although additional electrical energy may be supplied, this would only be used to support a steady magnetic field in the windings and would not lead to an increase in spark energy.

The 555 timer originally intended for setting the injection duration of an automotive fuel injector (see Section 3.3.2.1) was reconfigured to provide a TTL output pulse varying from 0–4 ms. This would ensure that the charging current stopped before

saturation. Hence the coil energy would be equal to the area of the triangle under the line up until the dwell time. Clearly this area varies with the square of the length of the base of the triangle.

The maximum energy available (corresponding to a dwell time of 4 ms) was calculated by measuring the voltage across a 30 mΩ resistor on an oscilloscope. Such a small value of resistor was chosen so that the voltage drop across it would be small and not reduce the voltage across the coil pack significantly. The rise time was measured as 4 ms and the maximum charging current as 11.5 A. As the resistance is assumed to be small, the inductance can be calculated from:

$$V = L\frac{\mathrm{d}I}{\mathrm{d}t} \tag{3.82}$$

$$L = \frac{V}{\left(\frac{\mathrm{d}I}{\mathrm{d}t}\right)} \tag{3.83}$$

Since the relationship between current and time is assumed to be linear:

$$L = \frac{V}{\left(\frac{\Delta I}{\Delta t}\right)} \tag{3.84}$$

$$= \frac{12}{\left(\frac{11.5}{4\times10^{-3}}\right)} \tag{3.85}$$

$$= 4.17 \times 10^{-3}\ \mathrm{H} \tag{3.86}$$

The maximum coil energy is calculated as:

$$W = \frac{1}{2}LI^2 \tag{3.87}$$

$$= \frac{1}{2} \times 4.17 \times 10^{-3} \times 11.5^2 \tag{3.88}$$

$$= 0.276\ \mathrm{J} \tag{3.89}$$

This is only an indication of the electrical energy provided by the coil. The efficiencies of the coil and spark plug would both need to be determined to find the actual

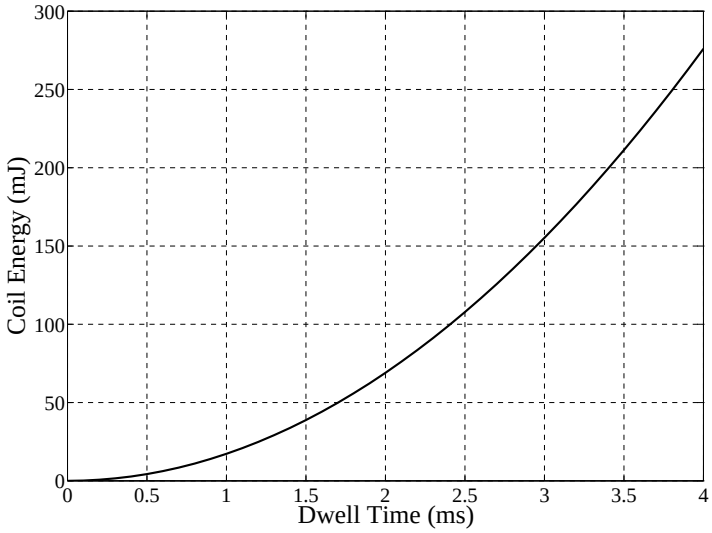

Figure 3.7: Coil energy against dwell time.

spark energy provided.

3.4.3 HT Measurements

To measure the HT energy, the voltage and current were measured and then multiplied and integrated. The voltage was measured using a special HT lead, which has a high impedance, low inductance 1000:1 potential divider in parallel with the spark plug, as shown in Figure 3.8. The output of the divider is then low enough to feed into the DAQ system to be recorded. A Pearson 411 current transducer forms a ring shape and has the HT lead thread through it. This generates an output voltage of 100 mV per A. This is then amplified by a factor of 500 using an instrumentation amplifier so that it can be measured by the DAQ.

The data recorded (see Figure 3.9) clearly shows the three main phases of operation. A rapidly increasing voltage forms across the spark gap. When it reaches the breakdown voltage of the gas in the gap, the spark occurs and the voltage drops. Current then starts to flow. In air at 1 barA this breakdown voltage is measured to be about 6 kV, but is so fast that the true peak may have been missed at the sampling rate used. Once the spark is set up, the voltage and current decrease. Finally the spark ends as the current falls to zero. The spark energy was found by multiplying the voltage and

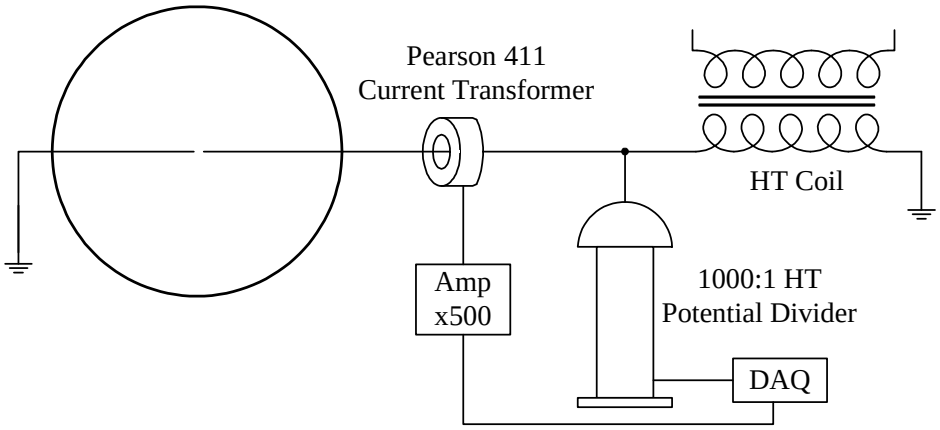

Figure 3.8: Circuit diagram of HT voltage and current measuring system.

current up to the end of the discharge phase. This power trace was then numerically integrated to give a total energy. This was done by both the trapezoidal and Simpson rule methods. The two agreed to 4 significant figures.

Measurements were made both for different pressures in the spark gap and different ignition system dwell times. It was found that pressure made little difference to the HT energy, but it increased with increasing dwell time. This is to be expected, as increasing the dwell time will increase the coil energy (see Figure 3.7), which will then increase the HT energy. For the 4 ms dwell time used for the experiments, the HT energy at a pressure of 1 barA was 68 mJ. This compares with a coil energy of 276 mJ, giving an efficiency for this stage of 25%. It should be noted that the HT energy is not the same as the spark energy delivered to the fuel-air mixture, as the spark plug will have an efficiency of its own, which is difficult to measure.

3.5 DAQ System

A National Instruments PCI-6024E DAQ card and break-out box were used to record the outputs of the system in conjunction with a PC, as well as aiding the mixture preparation process. The DAQ card has sixteen 12 bit analogue input channels with a maximum sampling rate of 200 kS s^{-1}. It also has two analogue outputs, eight digital input/output channels and two counter/timer channels. As a PCI card, the DAQ card

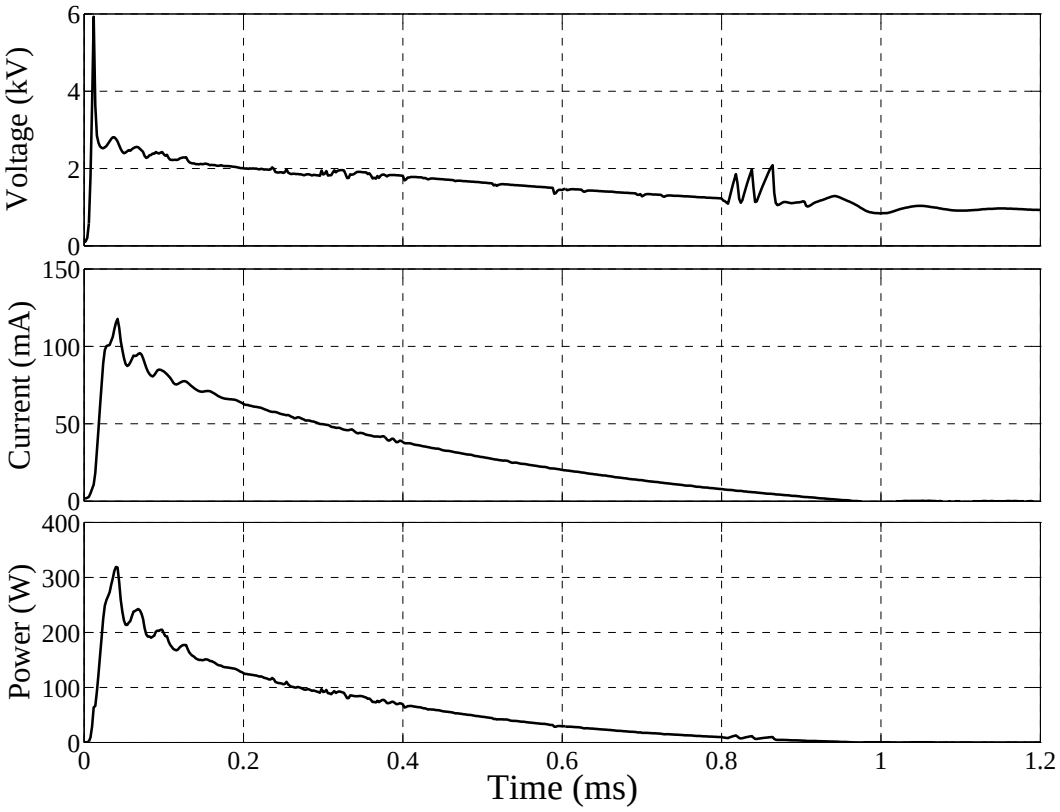

Figure 3.9: HT voltage, current and power for a spark in air at 1 bar with a dwell time of 4 ms. The energy was 68 mJ.

was mounted inside the PC. The breakout box was mounted with the other electronics on the front of the optical bench.

The card has software-selectable gain allowing input ranges of ±10 V, ±5 V, ±500 mV or ±50 mV. The range to use is calculated by the input scale (calibration curve) and maximum anticipated value for each channel. As an example, if we have a pressure sensor that gives an output of 0–5 V for a pressure range of 0–6 bar, it may have a calibration curve something like $p = 1.197V - 0.01$. The maximum pressure of 6 bar leads to a maximum actual voltage input of 5.02 V, meaning that the range used will be -10 to +10 V. As none of the sensors detailed below use negative voltages, and many of them can output more than 5V, at least half the input range is immediately wasted, reducing the system to only 11 or even 10 bits.

3.6 Sensors

3.6.1 Pressure Transducers

3.6.1.1 Mixture Preparation

As was described in Section 3.2, the air-fuel mixture is prepared by means of partial pressures. This requires pressure transducers to measure over the range from 0 barA to the maximum mixture preparation pressure, which was 4.2 barA. For this task, three Drück PMP1400 sensors were chosen, with pressure ranges of -1 to +1.6 barG, 0–6 barG and 0–250 mbarG respectively. The PMP1400 sensors have a combined non-linearity, hysteresis and repeatability error of 0.15%.

When experiments without residuals were being conducted, the bomb was flushed to ensure no remaining combustion products from the previous experiment. The pressure was reduced to approximately 35 mbar and then raised to approximately 5 bar. This was covered by the first two sensors. If this is repeated three times, then the concentration of gas remaining from the previous experiment will have been reduced to approximately:

$$\begin{aligned} \text{concentration} &= \left(\frac{35 \times 10^{-3}}{5}\right)^3 \\ &= 3.43 \times 10^{-7} \\ &= 0.343 \text{ ppm} \end{aligned} \tag{3.90}$$

These sensors also deal with the filling with air to the mixture pressure and reducing the pressure of the homogeneous mixture down to the final mixture pressure. The 250 mbar sensor is used to add the partial pressure of gaseous fuels. Since this has a smaller range, the fuel has to be added in its range i.e. just above atmospheric pressure.

These sensors require 9–30 V DC supply and have a 0–5 V DC output. They were calibrated with reference to a paraffin manometer for 0–60 mbarG, a mercury manometer for 0–2 barA and with a dead weight tester for pressures greater than

Table 3.1: Calibration parabola coefficients for the Kistler 7019 piezo-electric sensor used to measure pressure during combustion. The numbers relate the voltage in Volts to pressure in bar, as is shown in Equation (3.91).

Range (bar V^{-1})	a_0	a_1	a_2
5	0.0639	5.1138	-0.0159
2	0.0307	2.0676	-0.0040
1	0.0603	1.0356	-0.0008

2 barA. In all cases the coefficient of determination R^2 was better than 0.9999. An interface box was built to provide the sensors with power and provide BNC outputs suitable for connecting to the DAQ break out box.

Any zero error is removed by calibration against atmospheric pressure (measured using a Fortin barometer) twice per day.

3.6.1.2 Combustion

The pressure sensor in the bomb wall is required to have a wide pressure range, a very fast response time and resistance to high temperatures. For this a Kistler 701A piezo-electric sensor was used. This is connected to a Kistler type 5007 charge amplifier, which converts the charge to a voltage, which can then be fed into the DAQ system. The range in terms of Volts per bar can be altered on the charge amplifier, ensuring that the output makes best use of the voltage input range of the DAQ card. The sensor was calibrated using the dead weight tester and separate parabolic calibration curves were produced for charge amplifier ranges of 1, 2 and 5 bar V^{-1}. An example for 5 bar V^{-1} is shown in Figures 3.10 and 3.11. These curves are then inverted and multiplied by the charge amplifier range to give curves relating the voltage in Volts to the pressure in bar. This can then be entered into LabView, as a scale, with the form:

$$p = a_0 + a_1 V + a_2 V^2 \tag{3.91}$$

The coefficients used for the different ranges are shown in Table 3.1.

These ranges allow measurement up to 50 bar, which is greater than the maximum

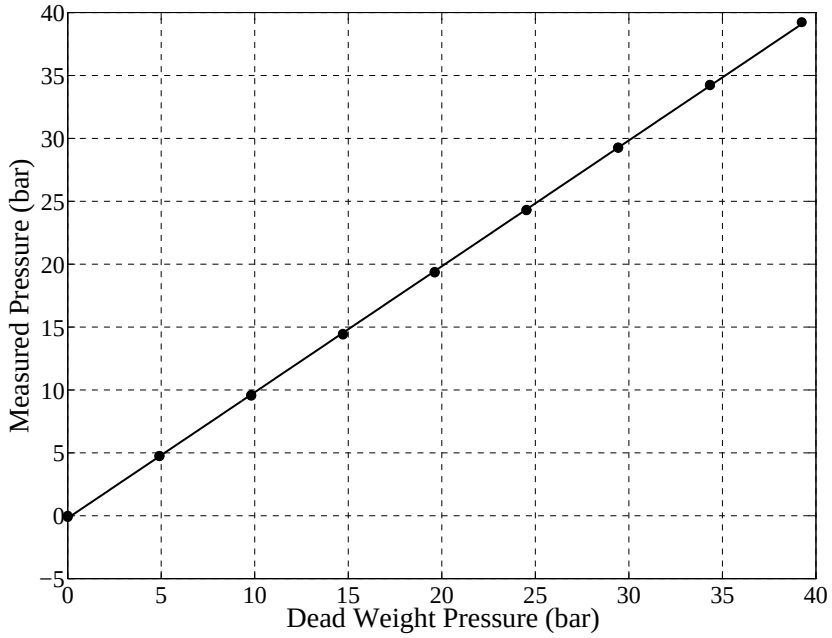

Figure 3.10: Kistler piezo-electric sensor calibration curve for a charge amplifier range of 5 bar V^{-1}. A linear fit gave $R^2 = 0.999946$ and a parabolic fit gave $R^2 = 0.999995$. The error between the points and the fits are shown in Figure 3.11.

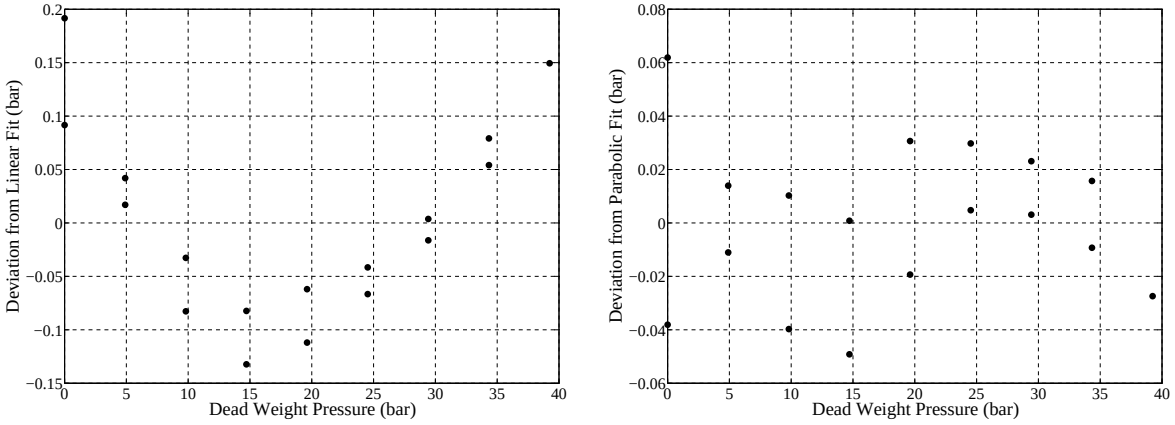

(a) Linear Fit

(b) Parabolic Fit

Figure 3.11: Error between the data points of Figure 3.10 and fitting functions, showing far smaller residuals with the parabolic fit, and no trend.

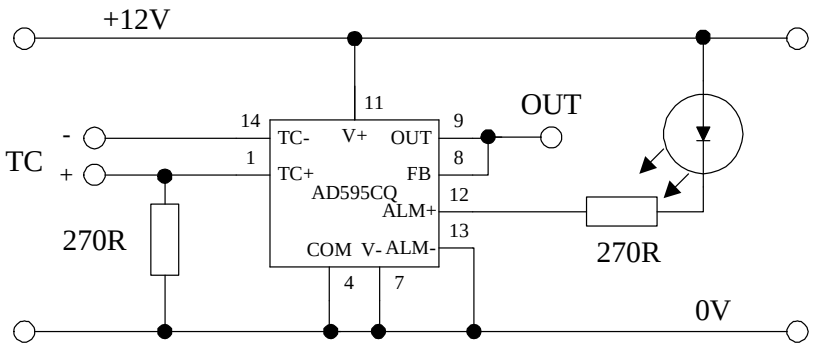

Figure 3.12: Thermocouple amplifier.

specified pressure of the bomb.

3.6.2 Temperature

3.6.2.1 Set-Up

The temperature of the bomb is required by the LabView program. It is also recorded during combustion, although this is for interest only, as the response time of the thermocouple is too slow to generate accurate data. A sealed thermocouple fitting is provided in the bomb, into which an exposed junction K-type thermocouple was placed. This was positioned to a depth so that the junction just protruded into the sphere. A second thermocouple was used to calculate the density of liquid fuels (see Section 3.3.1.2).

However, these thermocouples only produce a few mV output, so two AD595CQ ICs from Analog Devices were used to amplify the signal (see Figure 3.12). They contain cold junction compensation and convert from the K-type voltage to a a voltage output of 10 mV per °C. The LED lights if the thermocouple goes open circuit.

The thermocouples were calibrated against a mix of ice and water and against boiling water. The AD595CQ has a typical accuracy of ±1 K and the thermocouple ±1.5 K

3.6.2.2 Thermocouple Response

The response of even an exposed junction thermocouple is far too slow to be of use during combustion. Furthermore, there is the limited rate of heat transfer from the

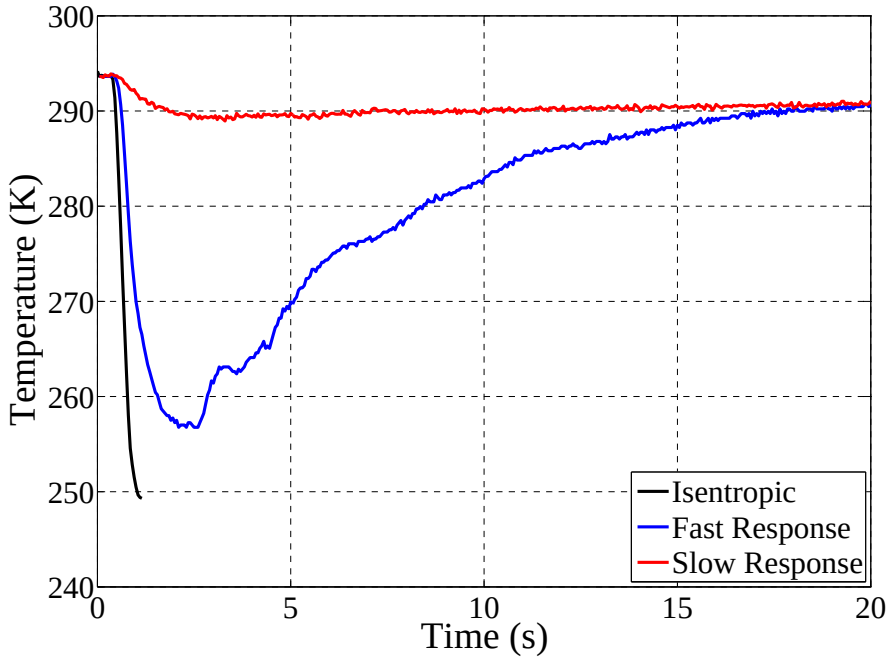

Figure 3.13: Temperature response of thermocouples to a sudden reduction in pressure.

gas to the sensor through the boundary layer (Garforth, 1976). The response during mixture preparation was also considered. Even though gases were added slowly, some isentropic temperature rise will occur during filling, meaning that fewer moles of gas than required are added. Hence the bomb thermocouple is used to measure any temperature rise and modify the pressure target accordingly. However, a slow response could leave the temperature reading lagging behind the actual temperature.

To test this, the exposed junction thermocouple was plumbed into a different chamber along with a pressure transducer and a fast response thermocouple made from 50µm wire. The latter has a faster response, but would be damaged by combustion in the bomb. Air was admitted to the vessel at a few bar and then let out suddenly for approximately a second by the opening of a ball valve. This sudden expansion causes an isentropic temperature drop. This was measured by the two thermocouples, as well as the pressure transducer. From the pressure trace, an isentropic temperature was calculated, assuming a ratio of specific heats at ambient temperature of 1.40.

Figure 3.13 shows the three measurements. Since the isentropic temperature is dependent on the response time of the pressure transducer, which is relatively fast, it will be the quickest to respond. The fast response thermocouple is not far behind. The

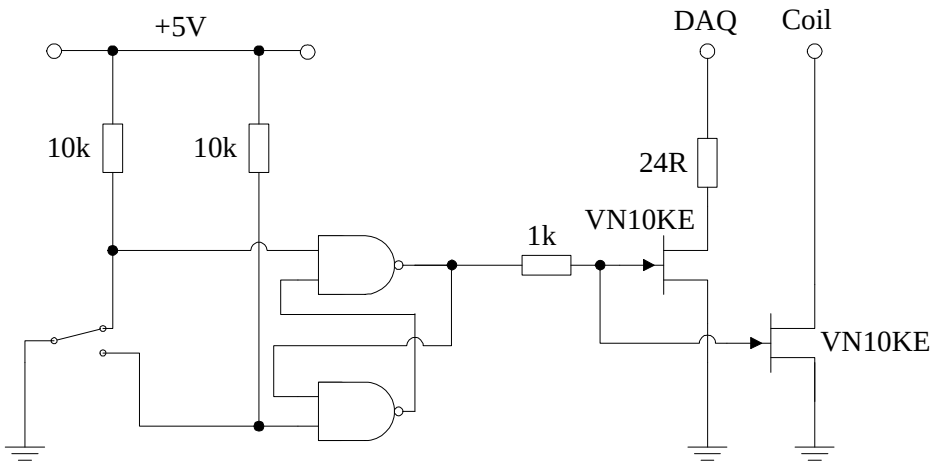

Figure 3.14: Lucas trigger unit.

exposed junction thermocouple is far slower to respond, but within 15 s there was only a few Kelvin disagreement. During the experiments, the gases are added slowly so that the change in temperature is no more than 1 K (a difference of approximately 0.2 % in absolute temperature), so any errors associated with the time response are very small.

3.6.3 Triggering

3.6.3.1 Lucas System

To provide a time base for the recorded pressure data, the data acquisition is started at the same time as the spark and the camera. The original Lucas coil pack for the inductive HT system already included a remote switch to fire the coil. When the push to make button is pressed, the magnetic field in the coil is set up. When the button is then released, this field rapidly collapses, causing a large voltage to be induced in the secondary winding, causing the spark. The voltage across this button could be used to trigger the DAQ, as it would drop to zero when pressed, and then rise again when released. Hence the DAQ would be triggered on the rising edge. However, it was found that when the button was pressed, significant switch bounce occurred, causing the voltage to drop, but then rise again momentarily, triggering the system before the button had been released i.e. before the spark had occurred. To combat this, a de-bounce circuit was produced.

This uses a bi-stable latch made from two cross-connected NAND gates. When the button is pushed, it shorts one input of one of the NAND gates to ground and the output goes to +5 V. When it is released, it shorts one input of the other NAND gate to ground, so the output goes to 0 V. However, even if the switch bounces on its contact, the output will not change, as this would require it to bounce as far as the other contact, which will not happen. So as long as the switch hits the correct contact once, the output transition occurs. This switches both the coil circuit and the DAQ digital edge trigger by the use of two FETs. Two must be used as the two circuits being switched use different voltages.

This output was also fed into an inverter to produce a positive TTL pulse to trigger the high speed camera.

3.6.3.2 Jaguar System

After successful use of the Lucas system for initial tests, it was decided that a system with variable spark energy would be useful in order to find the effect of spark energy on burning velocity. A new system was made, using a Jaguar coil pack. This unit has a coil and spark plug in one integrated unit. It is designed to provide the spark for one cylinder of a Jaguar V8 engine. Its main advantage is that the charging duration of the coil pack is controlled by the duration of a TTL pulse. A variable length pulse was generated by using the 555 timer circuit originally intended to control the fuel injector (see Section 3.3.2.1). However the power transistor was no longer required, as a TTL output was sufficient.

The push button to start the timer pulse was replaced by the inverted output of the de-bounce circuit. Hence when the trigger switch was pressed, the output of the 555 timer went high for a period determined by the RC circuit. The FET for the DAQ trigger was left unchanged, but the FET for the coil was discarded as the new coil had a TTL input. The output was, however, buffered to ensure that having three outputs connected in parallel did not reduce the output voltage of the 555 timer. A third (inverted) output was added to trigger the camera on the rising edge.

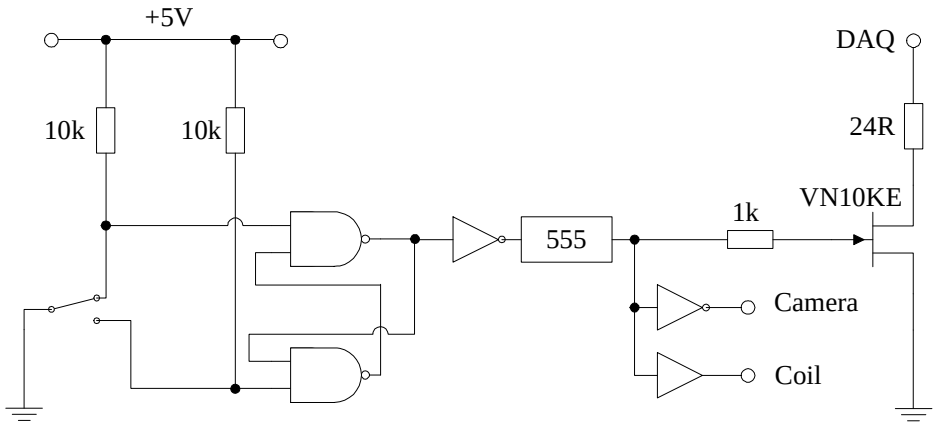

Figure 3.15: Jaguar trigger unit.

Table 3.2: Specified accuracy of the ECM AFRecorder lambda sensor in different lambda ranges.

λ	Accuracy
1	± 0.006
0.8–1.2	± 0.008
Elsewhere	± 0.009

The potentiometer was left unchanged, but the capacitors in the 555 timer were changed to alter the maximum pulse duration from 15/30 ms to 5/10 ms (low and high ranges). A digital oscilloscope was used to check the pulse duration.

3.6.4 Lambda Sensor

It was necessary to ensure that the fuel-air mixture was of the correct equivalence ratio. After completion of an experiment, the combustion products were fed past an ECM AFRecorder lambda sensor and were then safely removed from the laboratory. The lambda sensor has claimed accuracies as shown in Table 3.2. It only has 2 dp output display, which adds an extra error of ± 0.005.

The lambda sensor was calibrated with lab air, nitrogen and two calibration gases. The CalGas consists of 6.29% oxygen in nitrogen, with a 2% tolerance. This is used to test the lean condition. The lambda value for this was calculated assuming an H/C ratio of 1.8. The MOT Mix contains 1970 ppm propane, 3.5% carbon monoxide and 14% carbon dioxide. The balance is again nitrogen. This is used to test the rich

Table 3.3: Comparison of the ECM AFRecorder lambda sensor against four calibration gases.

	% Volume O_2		λ	
Gas	Nominal	Measured	Nominal	Measured
Air	20.95	20.98	-	-
Nitrogen	-	-	1	0.99
CalGas	6.29 ± 0.13	6.10	1.443–1.469	1.42 ± 0.014
MOT Mix	-	-	0.888–0.890	0.93 ± 0.013

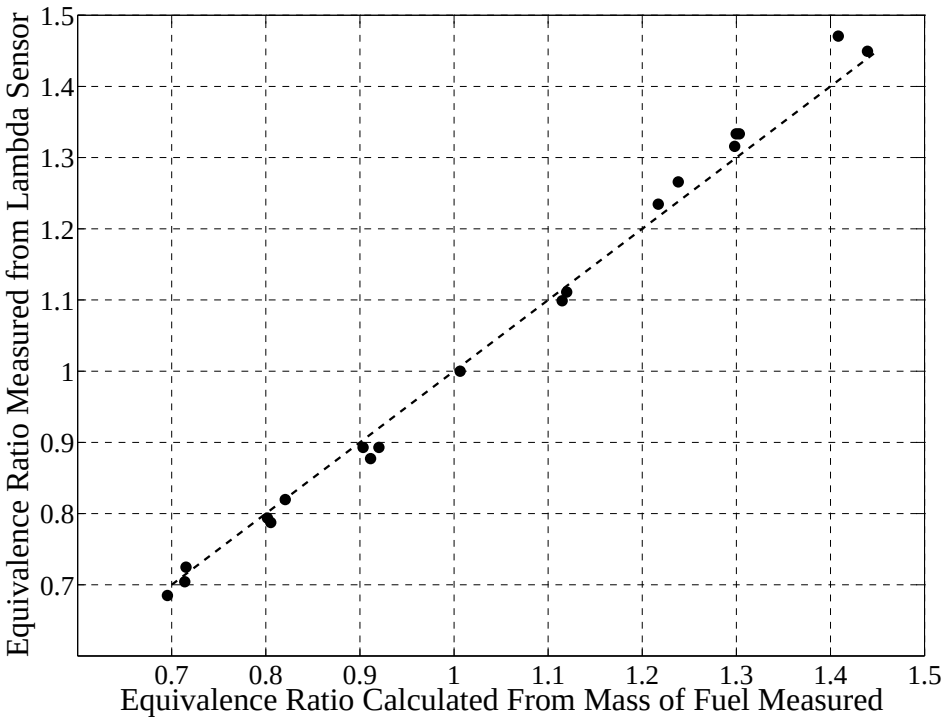

Figure 3.16: Equivalence ratio given by the lambda sensor against that calculated from the mass of fuel injected for tests with toluene. Dashed line shows ideal $y = x$ relation.

condition. The tolerance on each of the constituents is 1%, which leads to a maximum error in lambda of 0.14%. The results from these tests are given in Table 3.3.

The lambda sensor was also tested by comparing its output with the theoretical lambda derived from the mass of fuel injected, measured by weighing the syringe before and after injection. Figure 3.16 shows good agreement, although there may be slightly different trends in the rich and lean regimes. Further details of these tests are given in Section 5.1.2.2.

3.7 Environmental Chamber

The bomb sits on a layer of Sindanyo insulation material and can be covered by a box of Sindanyo with Melafoam insulation and aluminium cladding. It has a one piece top and sides and two end pieces which fit over the windows of the bomb. Connections and holes are provided in the chamber for the thermocouple, pressure transducer, HT lead, valves and pipework. On top of the chamber is a fan heater and controller which controls the temperature in the bomb (see Figure 3.1). The large heat capacity of the system requires heating for several hours to reach the higher test temperatures. The maximum rated temperature of the bomb is 200°C. The controller is a West 5600, which has a set-point resolution of 1°C and can control the temperature of the bomb to ±0.5°C. For convenience a LabView program is used to monitor the warm-up process (see Section 3.8.3).

3.8 LabView

The readings from the DAQ system are read into the National Instruments *LabView* software. Here the voltages from each channel are subject to polynomial calibration transformations to produce the correct units. A LabView program was written to display the data, calculate relevant parameters and then store the pressure trace during combustion. This program is split into two tabs. The first aids mixture preparation and the second is for experiment execution.

3.8.1 Mixture Preparation

To save calculating the partial pressure or volume of fuel required for every experiment by hand, the program will work it out for the user, and use virtual graphs and dials to ensure that the correct quantity is added (see Figure 3.17). These values were checked by hand calculations and a spreadsheet. The fuel is selected from a drop-down box. It then shows how much air is required to top-up the mixture, using the temperature

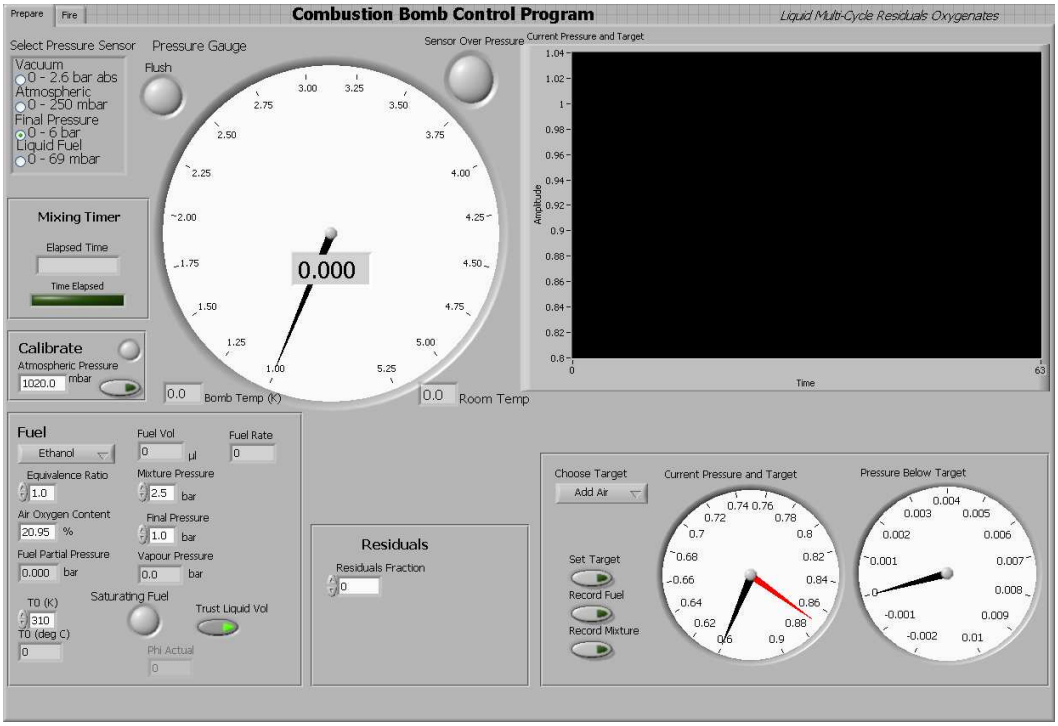

Figure 3.17: The LabView mixture preparation tab.

data from the thermocouple as well as the pressure sensors to ensure that even if the mixture changes temperature, the correct number of moles of air will be added by assuming an ideal gas. The program also calculates the actual value of equivalence ratio from the moles of air and fuel added, times the mixing process (5 minutes) to ensure homogeneity, and guides the user to the final pressure.

Throughout the liquid delivery process, care was taken to ensure that the fuel evaporated fully. The LabView program helps in this by calculating the vapour pressure of the fuel in real time. To do this it uses a correlation and data from Reid et al. (1987). This requires the critical pressure and temperature of the fuel along with four fuel-specific constants for the polynomial and the current temperature of the bomb (see Figure 3.18):

$$a = 1 - \frac{T}{T_c} \tag{3.92}$$

$$p_{vp} = p_c \times \exp\left((1-a)^{-1}\left(Aa + Ba^{1.5} + Ca^3 + Da^6\right)\right) \tag{3.93}$$

If the vapour pressure is less than required partial pressure of fuel, a red light is illu-

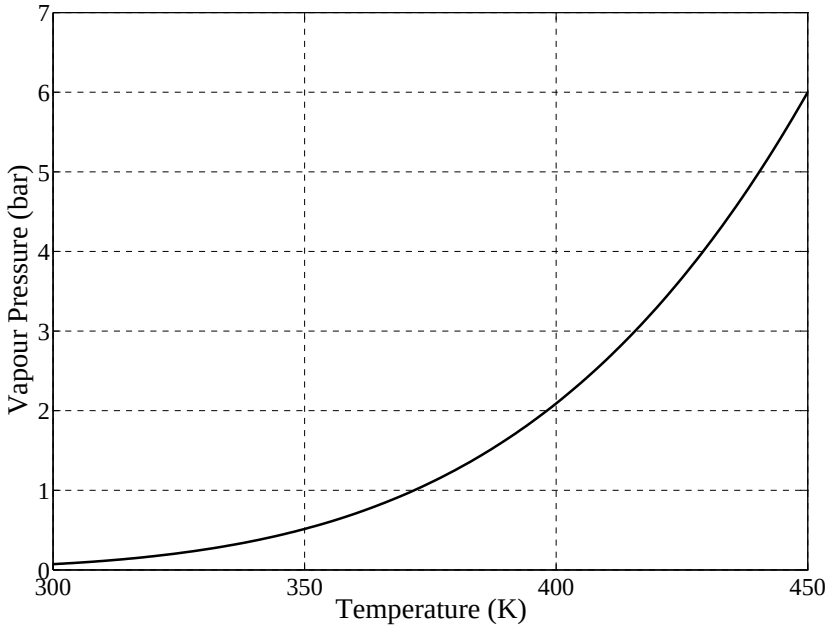

Figure 3.18: Vapour pressure of iso-octane plotted using the correlation of Reid et al. (1987).

minated to warn that condensation could occur. In practice this only became relevant at lower temperatures. At the higher temperatures the vapour pressure was often a hundred times the partial pressure of fuel.

For experiments with residuals, there is the further problem of water vapour in the residuals from the dummy or previous experiments condensing during the preparation of the mixture for the next experiment. This would lead to an inhomogeneous mixture, but also, if the water is in the liquid phase, the pressure of the residuals will decrease and no longer be proportional to the number of moles of residuals, as the equation of state will no longer apply.

For these reasons the saturation temperature of the water vapour needs to be calculated to ensure that the bomb temperature does not fall below this value during preparation for the following experiment. Equation (3.93) can also be used for water, and is valid from 275 K up to the critical temperature (T_c = 647.3 K). The partial pressure of the water in the residual gases can be calculated from the output of the BOMB program:

$$p\prime_{H_2O} = \frac{\%H_2O}{100} \times p_{end} \times \frac{T_0}{\bar{T}_{end}} \tag{3.94}$$

Here, $\%H_2O$ is the percentage by moles of water vapour in the products. $\bar{T}_{\text{end}}$ is the mean of the end temperatures (the temperature when mass fraction burned is equal to one) across all zones.

However, entering these values for every experiment would be time consuming. Hence a worst case approach was taken for each fuel. The BOMB program was run for different initial conditions to find which caused the highest partial pressure of water vapour as given by Equation (3.94). This was found to occur for a rich, high initial pressure experiment with no residuals and a low initial temperature. If the partial pressure is greater than the vapour pressure, then saturation will occur.

However, it is temperature, not pressure, that can be controlled and so what is ideally required is T_{sat}, the temperature at which the partial pressure of water equals the saturation pressure. Rearrangement of Equation (3.93) in terms of T is impossible, so an iterative solver is required to operate in real time, calculating T_{sat} when $p_{\text{vp}} = p\prime_{H_2O}$. This can be carried out in LabView by the use of Mathscript, whereby LabView runs a MATLAB compiler, allowing the execution of MATLAB scripts in LabView. Finding the solution of this equation can be achieved in MATLAB using the *fzero* function. However, this was found to slow down the LabView program to an unacceptable level. Hence it was decided that a warning light based on the estimated partial pressure of water vapour in the residuals exceeding the vapour pressure would suffice.

3.8.2 Combustion

The second tab (see Figure 3.19) allows the user to alter the number of samples recorded, as some mixtures will burn far faster or slower than others. Also shown is data about the experimental conditions, which is appended to the written data file along with a user comment. Once the user is ready to proceed with combustion, they click on 'Ready to Fire' which changes the mode of the program from real time data collecting to high speed (currently 10 kS s^{-1}) data acquisition. The program now waits for a rising edge which comes from the trigger unit (see Section 3.6.3) into channel PFI0

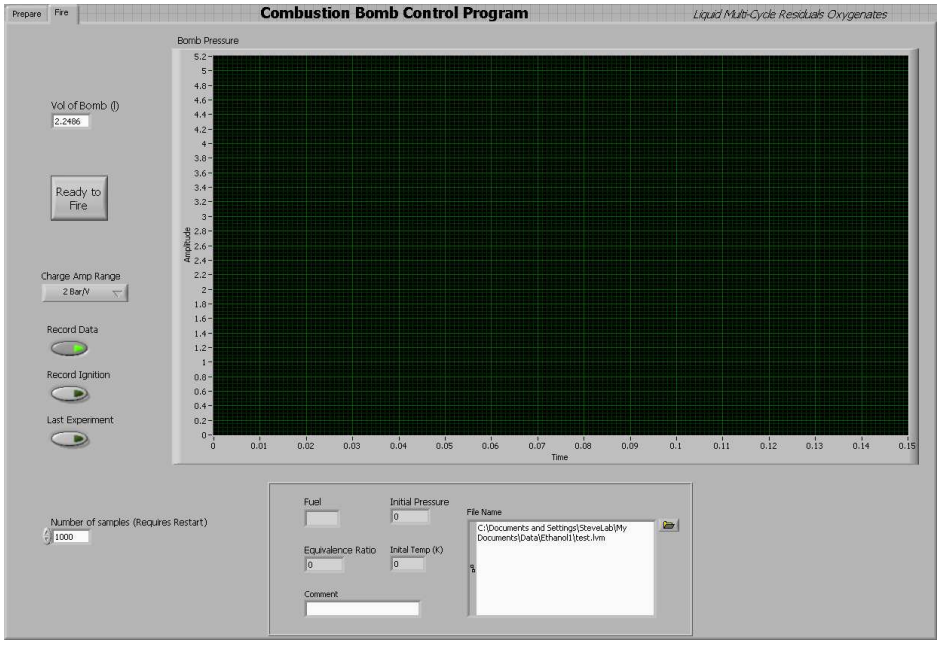

Figure 3.19: The LabView data acquisition tab.

of the break out box. This indicates that the ignition push-button has been released and so the spark is occurring. The DAQ system then records data for the specified number of samples and prompts the user to save in an .lvm file, which can be read by either Microsoft Excel or MATLAB. The pressure record is then displayed to allow the user to see if a successful combustion event has occurred. The program then reverts to the mixture preparation mode in readiness for the next experiment.

3.8.3 Warmup

A second LabView program has been written to aid with preparation of the environmental chamber. This is a simple program which monitors the temperature of the bomb at a slow sampling rate. A high or low set-point can be specified in terms of Kelvin or degrees Celsius and when the set point is reached, a light will turn on and the program ends. Additionally, there is an option for the program to send an e-mail to a specified address, stating the temperature that has successfully been reached. This saves the user from having to check the temperature if a change of temperature is being made between experiments.

3.9 Mixtures

Mixtures were specified in terms of liquid volumes e.g. 50% iso-octane, 50% ethylbenzene. They were mixed using a 25 ml pipette. Mixtures in the proportions 75%/25% and 87.5%/12.5% were mixed by successive dilution. Time was allowed for throrough mixing.

Most of the properties required for the fuels (e.g. molecular mass, specific heat capacity) are molar properties. Hence liquid volume fraction had to be converted to molar fraction. Rearranging Equation (3.30) gives:

$$n = \frac{\rho V}{M}$$

This can be calculated for each of the pure components A and B, setting V to the appropriate percentage volume. The mole fraction of component A is then found from:

$$x_{\mathrm{A}} = \frac{n_{\mathrm{A}}}{n_{\mathrm{A}} + n_{\mathrm{B}}} \tag{3.95}$$

This was then used to interpolate the molecular mass, the number of C, H and O atoms and the enthalpy and entropy (see Section 4.3.1.1), using the known properties of the pure components.

The liquid density was found from the model of Davy and Kowsari (2010) for iso-octane/ethylbenzene and from the experimental data of Ku and Tu (2005) for the iso-octane/ethanol mixture. The relation being used to calculate specific heat capacity (see Equation 4.11) was a polynomial, hence the polynomial for the mixture was found by interpolating each coefficient using the molar fraction. Finally, as a check only required at low temperatures, the coefficients required to calculate vapour pressure were set to be equal to those of the worst-case component (i.e. that with the lowest vapour pressure).

A slightly modified LabView program was produced, which allowed direct entry of data rather than relying on data entered into a table. This was deemed to be faster

when changing between different fuels.

3.10 Schlieren System

3.10.1 Reasons for Construction

Preliminary results showed a large amount of noise in the calculated values of burning velocity during the early stages of combustion, due to the very small flame radius leading to error in interpolation and differentiation. Section 2.9 explains that a schlieren photography system allows imaging of the flame front for diameters up to that of the bomb windows i.e. 40 mm. Schlieren provides a far sharper edge than normal photography of the visible chemiluminescence from the flame front. Conventional photography can also give incorrect results as the radius at which illuminance first occurs is some way behind the real flame front (Rallis and Garforth, 1980). Hence it was decided to design and build a schlieren system for use with the bomb. This system can also be used to detect cellularity.

3.10.2 System Design

Systems such as that shown in Figure 2.20 which use lenses tend to end up being very long. An alternative is the Z-type system using two parabolic or spherical mirrors, as was shown in Figure 2.21. The mirrors are oppositely tilted to reduce the effect of coma — an aberration caused in such systems because the direction of reflected light depends on the point on the mirror it is reflecting off (Holder and North, 1963).

The system had to fit onto an existing optical bench with the bomb sitting in the middle. To fit the optics into the remaining space, folding mirrors were used to create two further 'Z's, as seen in Figure 3.20.

Although the off-axis angle of the spherical mirrors must be kept as low as possible, the angle of the plane folding mirrors can be altered to suit the space available.

A plate was made to mount the bomb to the optical bench with the central axis in

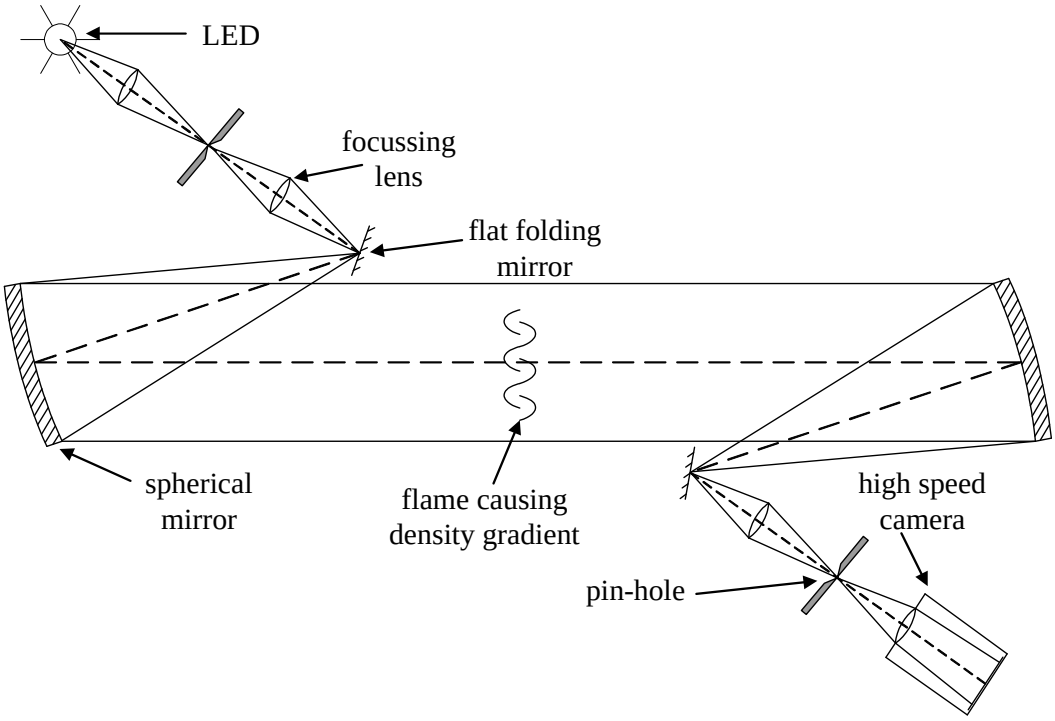

Figure 3.20: Folded Z-type schlieren system

line with one of the lines of holes in the bench used for mounting components accurately. This set the height of the bomb and hence the height of the optical axis (i.e. a line through the centre of the windows) at 223 mm above the bench. Hence all the optics would need to be in this horizontal plane. Rails mounted on posts ensured alignment of lenses, pin-holes and the light source. The optics were mounted on short posts held by carriages which can slide up and down the rail, allowing for easy 1D adjustment. The mirrors were mounted on adjustable height posts secured to the bench by clamping forks.

3.10.3 Illumination

Common illumination methods include mercury discharge lamps and lasers. Although a high intensity is required, it is the beam angle that is of more importance due to the high f/number of the system. A tungsten or halogen bulb may be very bright, but being fairly isotropic, the vast majority of the light is wasted. It was for this reason that LEDs were investigated. The power of these devices has been increasing over the

last few years, and some models feature very low beam angles. They also do not have the safety complications of lasers. Several models were tested. The preferred option was a 1 W green Prolight Power Star/O LED. The inner cone angle of this device was measured to be 6.4°. Green was chosen, as there was concern about light from the combustion interfering with the schlieren system. Since radiation from soot is mostly in the red region, green schlieren illumination would allow the use of a green bandpass filter after the bomb to filter out the light from combustion. However it was found after testing that this was not a problem, and the green filter was not subsequently required. Nonetheless, the green LED remained.

3.10.4 Mirrors

As the windows of the bomb are 40 mm in diameter, it is required that the spherical mirrors be larger, to catch any light refracted outside of the 40 mm beam. The f/number of these mirrors should be high to reduce the effect of astigmatism. Off-axis parabolic mirrors are made with a wedge shape so that they focus parallel light to a spot off their axis. This would be an ideal solution, however their complicated design makes them prohibitively expensive.

Spherical mirrors are available in many sizes and focal lengths. A high f/number implies a long focal length and small diameter, however the focal length is limited by the distance available on the bench. The mirrors chosen were by Techspec and had a focal length of 635 mm and a diameter of 63.5 mm, giving them an f/number of 10. They are polished to $\frac{\lambda}{8}$ and had an enhanced aluminium coating for better reflectivity in the visible range.

Unfortunately these mirrors were a non-standard diameter, and no kinematic mirror mounts were available. Hence mirror mounts were constructed which held the optics with nylon screws and fitted into a 2" commercial mirror mount (see Figure 3.21). These were made of aluminium alloy.

The folding mirrors are plain mirrors which reflect a narrow beam. This beam

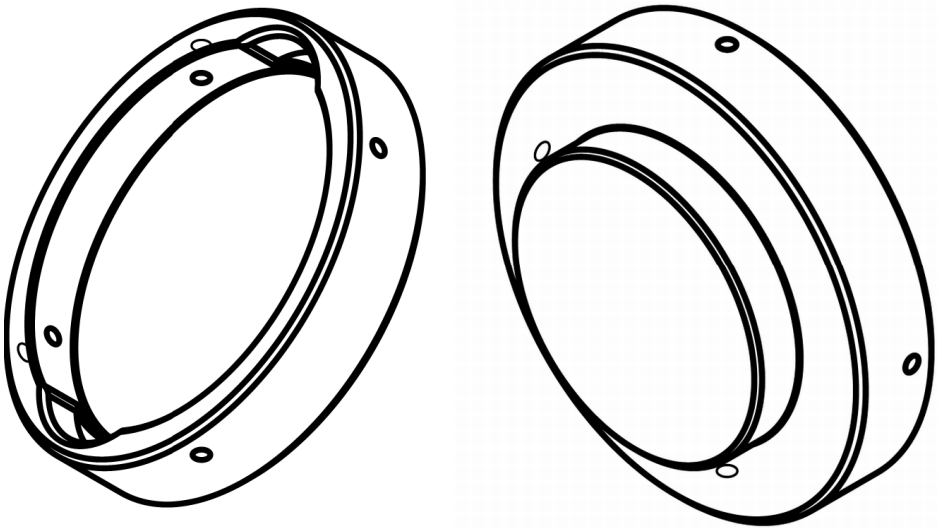

Figure 3.21: Isometric view of front and back of mirror mounts. Not to scale.

is focussed on one edge of the mirror so that it can be tucked in tightly against the bomb wall to reduce the Z angle as much as possible. Miniature angle mounts with a 22×22 mm $\frac{\lambda}{4}$ first surface mirror were chosen.

3.10.5 Lenses

The lenses are used to create point sources at the folding mirrors and pin-holes. Due to the high f/number of the system, these are very small. Unless the source is monochromatic, the lenses should be achromatic, else refraction in the lens will cause the focal length to be dependent on frequency. The lenses chosen were again by Techspec and had a diameter of 12.5 mm and a focal length of 75 mm. They had a VIS 0° anti-reflection coating. This cuts reflection down to less than 0.4% in the range 425–675 nm. These were held in 0.5" mounts.

The final lens in the system is the camera lens. A manual Nikon lens of focal length 135 mm, f/2.8 was used, along with a set of bellows to act as a long extension tube. This allowed focusing on the image. A custom mount was made for the bellows which allowed adjustment in two directions. A brass variable height support was screwed into the tripod mount of the camera to support its weight.

3.10.6 Knife Edge

Linear knife edges only allow detection of density gradients perpendicular to the edge. As the object of interest has spherical symmetry, it makes sense to use a circular pin-hole rather than a knife-edge. The effect of extending or retracting the knife-edge from the beam is replicated by using an iris so that the diameter of the hole can be adjusted. This allows for adjustment of sensitivity. A smaller hole will result in a higher sensitivity to density gradients. However, with too small a hole diffraction effects will cause the image to lose sharpness. The iris makes it easy to adjust this compromise depending on the initial pressure of the experiment, which affects the change in density across the flame front and the flame front thickness and hence alters the density gradient doubly.

3.10.7 Camera

Two Photron 1024 PCI cameras were available: one colour and one monochrome. Both have a maximum frame rate of 109,500 fps, and at their maximum resolution of 1024×1024 they can operate at up to 1,000 fps. The 1024 PCI is a PC based system, using a 10 bit CMOS sensor. The minimum shutter duration is 1.5 µs. It is triggered by TTL inputs and can output stills and video in a variety of formats.

It was decided that a frame rate of 1,000 fps did not give a sufficient number of frames with the flame front in view, especially for the faster burning mixtures. A reduced resolution of 512×512 pixels was chosen, as this allowed the frame rate to be increased to 3,000 fps. The camera's on-board memory allowed for over 13,000 frames to be stored—enough for more than 4 s of video. In practice, usually only a few tens of frames were required before the flame front left the field of view, and a few hundred before cellularity developed and the flame front reached the bomb wall.

The camera has many trigger modes, but for this case the simple START mode was sufficient. This starts recording on a rising edge fed into the external TTL input and records until the memory is full. In this way electronics could be built to ensure that the

images would be synchronised with the data acquisition and spark (see Section 3.6.3.2).

Images were saved as individual sequentially numbered 8 bit TIFF files. Hence each image had a size of 256 KB. Videos were saved in AVI format using the Indeo5 codec with video information added to the top of the image. The TIFF images were used for analysis and the videos allowed easy inspection.

3.10.8 Windows

The original windows were constructed of Spectrosil B fused silica. Their breaking pressure exceeded the rated pressure of the vessel. The schlieren beam was used to examine the existing stock of windows. Many were found to have chips or defects in the glass. It was decided to have a batch of new windows manufactured from Spectrosil 2000 by Newcastle Optical Engineering. The windows are 59.55 +0.02/-0.01 mm in diameter and 20.0 ± 0.1 mm thick. They have a 1.0×4.6 mm chamfer on each of the edges to aid fitting. Flatness across each of the faces was specified to $\frac{\lambda}{4}$. Parallelism was specified to be less than λ (approximated to be 550 nm i.e. the middle of the visible range) over the diameter of the window. The parallelism thus had to be better than:

$$\tan\psi = \frac{\lambda}{d} \tag{3.96}$$

$$= \frac{550 \times 10^{-9}}{59.6 \times 10^{-3}} \tag{3.97}$$

$$\psi = 5.29 \times 10^{-4\circ} \tag{3.98}$$

$$= 1.90" \tag{3.99}$$

Viton O-rings seal the windows. A ring of gasket material was placed under the windows. A second gasket ring and a ring of brass was placed between the windows and the end caps to prevent contact between metal and quartz.

Removal of the caps allows cleaning of the outside of the windows without disassembly of the bomb or oven, but cleaning of the inside of the window is impossible without removing the windows. Unfortunately, combustion deposits form quickly on

the inside of the windows. These have to be removed as much as possible by the image processing algorithm (see Section 4.2.1.1.1).

3.11 Conclusions

A spherical combustion vessel with oven was refurbished and augmented with new systems for fuel injection, ignition, data acquisition and high speed schlieren photography. A LabView program was written to aid accurate mixture preparation and record pressure data during combustion. Triggering electronics allow simultaneous triggering of the spark, schlieren photography and data acquisition. A variable dwell time ignition system was built to allow changes in ignition energy. Two options for fuel injection were analysed, and the syringe method was preferred due to its simplicity and better control. A schlieren system was constructed to allow visualisation of the flame.

Chapter 4

Data Analysis

4.1 *BVICS* Architecture

A number of programs have been written to analyse the burning velocity data. An overview of this process is shown in Figure 4.1. In order to streamline data processing, a graphical user interface (GUI) has been written to control all the programs from a single window and exchange data between them. The *BVICS* (Burning Velocity Integrated Calculation System) program allows the user to set options for the batch, run the multi-zone model, run *bvimage* and *burnvel* to get burning velocity data from schlieren image and pressure data respectively and then concatenate and save the data (see Figure 4.2). The *fitcorr* program can then be run to find correlation coefficients, which can be saved. The graph plotting tools described in Section 4.8 can be launched to plot graphs. There is a set of axes in the GUI used to display graphs generated by the various programs. The most important of these is the selection of burning velocity data as calculated from the pressure record (see Figure 4.15).

4.2 Image Processing

With rotating photographic drums or high speed ciné cameras, once the film had been developed, laborious manual procedures were required to derive radius-time data from

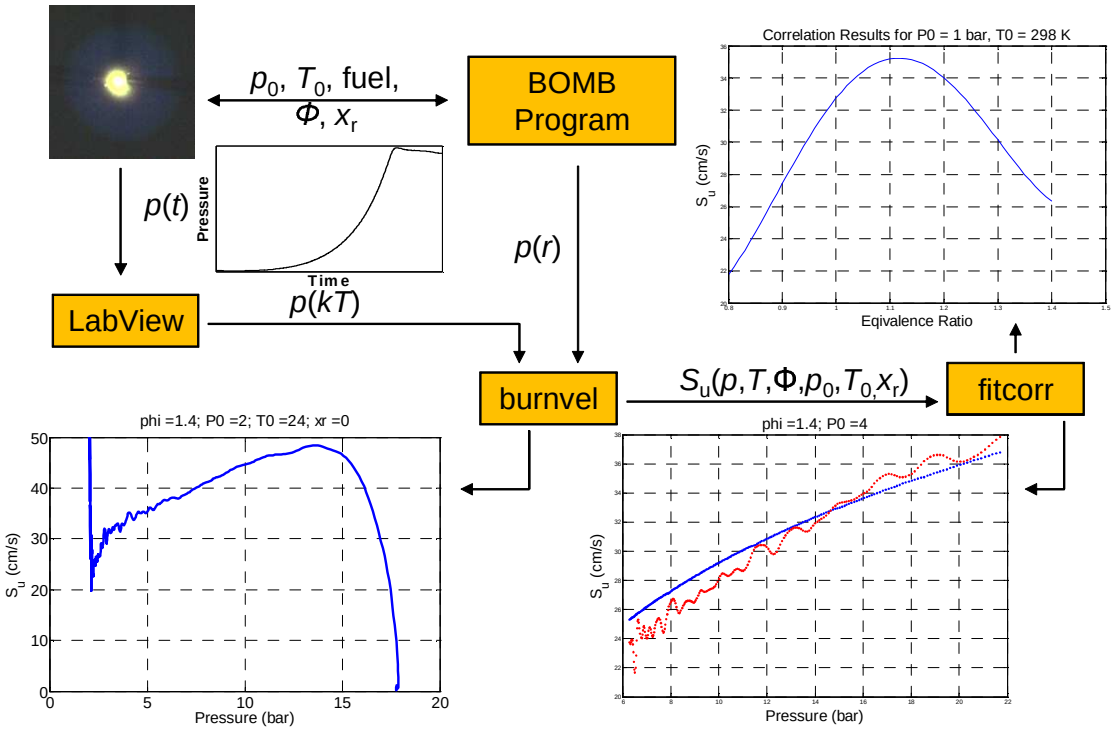

Figure 4.1: Overview of burning velocity calculations from the BOMB program and experiment.

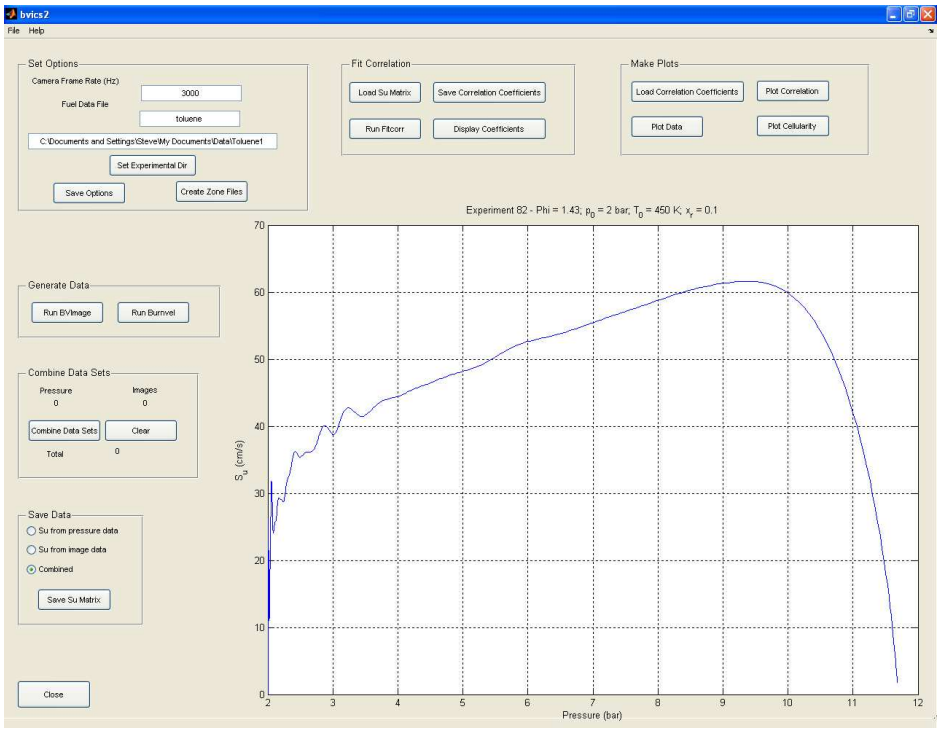

Figure 4.2: BVICS screenshot showing graph of burning velocity against pressure in the axes.

the images. With modern high speed digital cameras, the images are immediately available in a digital format which lends itself to computer-based processing to find the radius and other useful information. Once these processes are automated they can be left to run with no user interaction required, allowing for complicated algorithms that may take some time to execute.

4.2.1 Radius Calculation

It is known that in the absence of buoyancy, the schlieren image of the flame should consist of an approximate circle, nominally centred at the spark gap. The radius of this circle will increase until its edge is out of the circular field of view, defined by the windows in the bomb. Several methods were tested to build a MATLAB computer program capable of finding this radius reliably.

4.2.1.1 Thresholding Method

In the schlieren images the edge of the flame appears as a dark circle, the thickness of which varies depending on the temperature difference between the burned and unburned gases, the flame front thickness and the sensitivity of the schlieren system. If this circle can be recognised by the program, then its location and dimensions can be found. The challenge is to isolate it from other features in the photographs, particularly the electrodes and dirt that builds up on the optics, particularly the inside of the windows.

4.2.1.1.1 Background Removal A common method of removing unwanted artefacts which stay constant in every frame is to use background subtraction relative to a reference frame. This frame contains all the artefacts to be removed (such as the electrodes and dirt on the windows), but not the artefacts of interest (i.e. the flame). For the image sequences, the first frame was used, as this did not contain any image information. This has been shown to give good results, especially in removing the electrodes, as is shown in Figure 4.3.

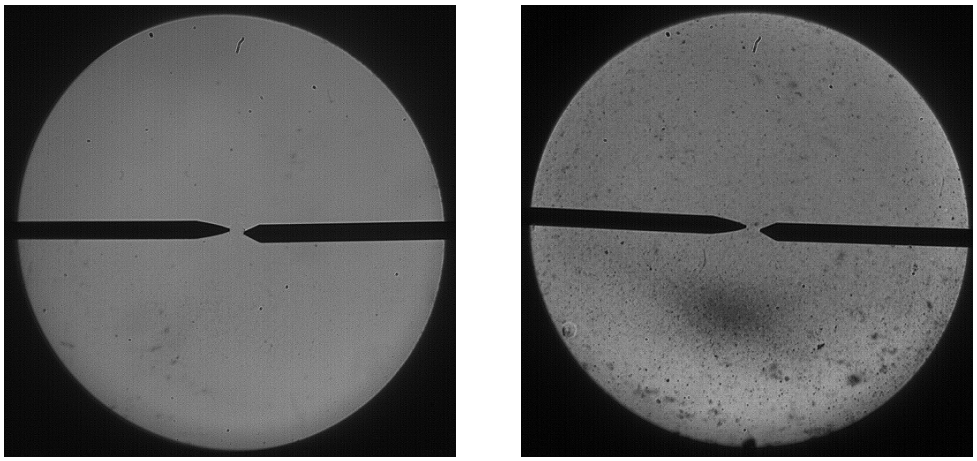

Background image

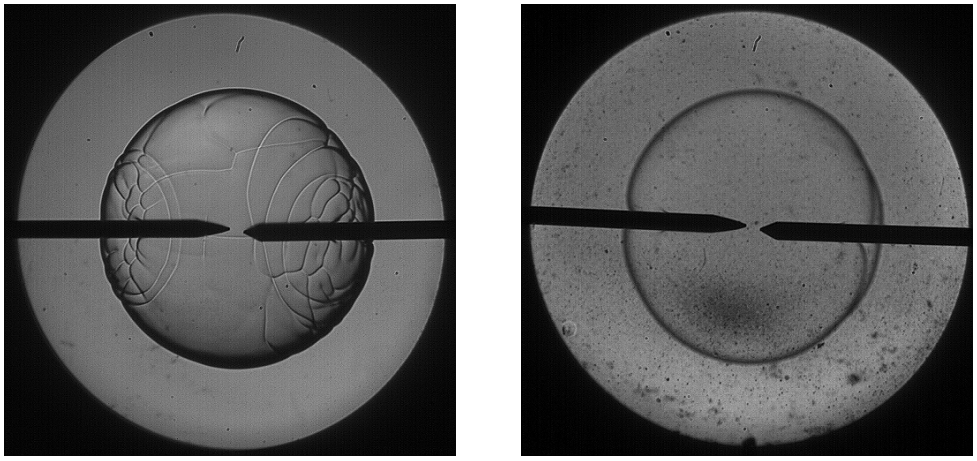

Sample image

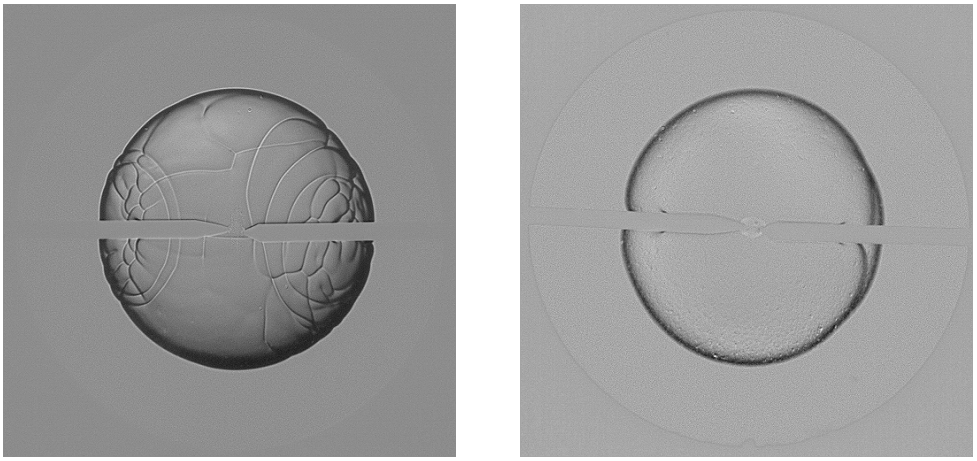

Subtracted image

Figure 4.3: Background for clean and dirty images, showing removal of dirt and electrodes. The flame on the left shows cracks on the surface.

4.2.1.1.2 Thresholding To decide what is flame front and what is not, the image is *thresholded*. In this process, a threshold level between zero and one is chosen and a Boolean matrix generated, where every pixel in the image with a magnitude greater than or equal to the threshold level is set to 1, and all below are set to 0. This is a very simple procedure to implement, but the difficulty comes in choosing a threshold level to differentiate between the artefacts of interest and everything else, without losing vital information. MATLAB includes a function *graythresh* which attempts to do this using the method of Otsu (1979). This chooses the threshold such that the intra-class variance of the black and white pixels is minimised. However, tests showed that a fixed threshold of 0.95 gave better results.

4.2.1.1.3 Erosion and Dilation In a binary image, a boundary point is defined as being a pixel that it located inside an object, but that has at least one neighbour outside the object (Castleman, 1996). Erosion is the process of eliminating all the boundary points of an object. Hence the object reduces in size by one pixel all around its perimeter (see Figure 4.4). Any part of the object that is fewer than three pixels wide will be cut off by the erosion operation. Similarly, any objects that are two or fewer pixels wide in any direction will be eliminated entirely. This is useful for smoothing the edges of objects and removing small artefacts.

Dilation incorporates all the pixels that touch an object into the object, hence making it bigger by one pixel all the way round. This has the effect of filling concave sections of the surface of the object, and connecting objects that are close together.

Opening is the process of erosion followed by dilation. This eliminates small and thin objects and smooths the edges of larger objects without changing their area.

Closing is the opposite: dilation followed by erosion. This fills small and thin holes and smooths boundaries of larger objects.

4.2.1.1.4 Edge Detection Edge detection attempts to find boundaries between regions of distinct grey level (Gonzalez and Woods, 1993). This is normally done by

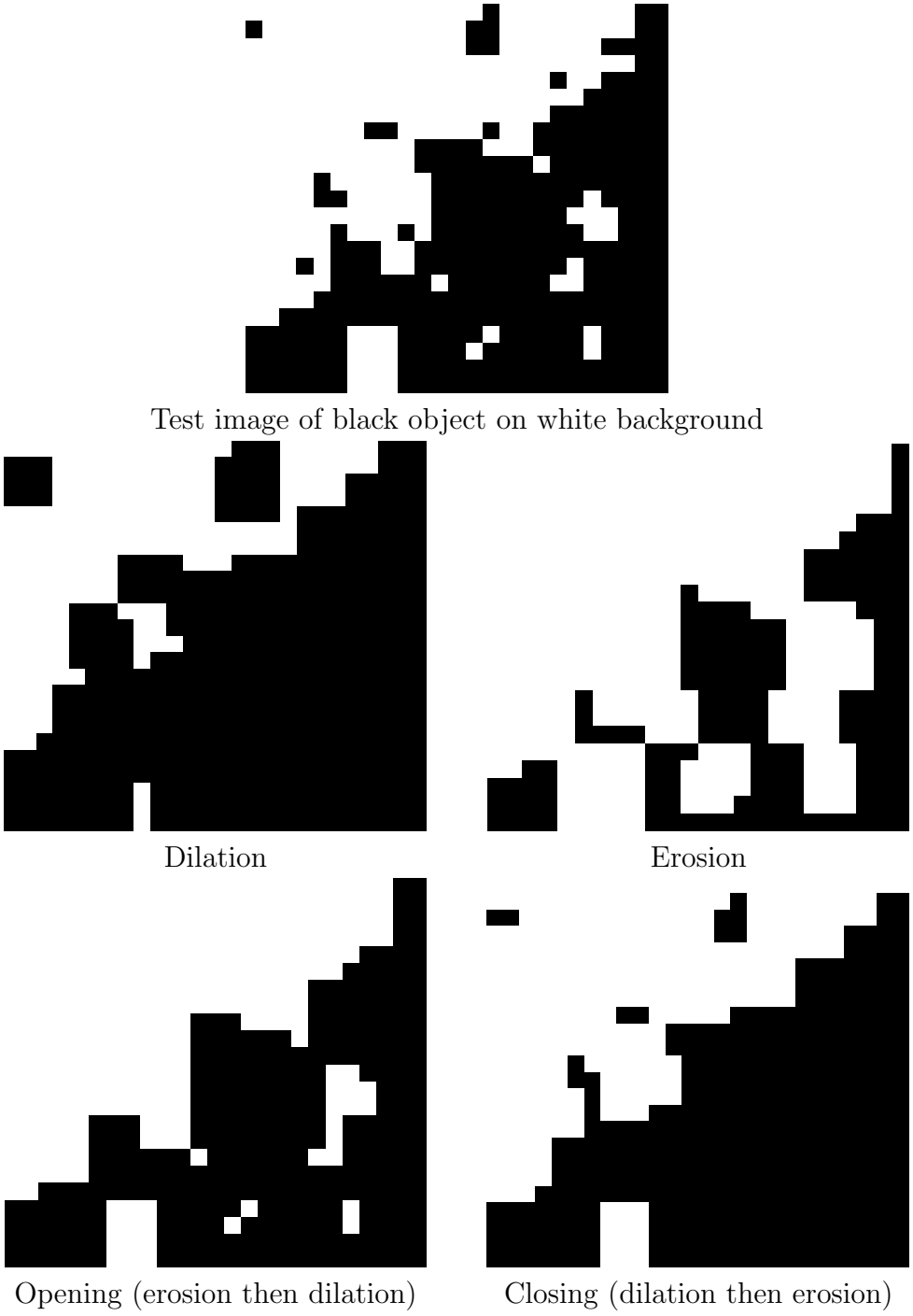

Figure 4.4: Erosion and dilation of a test image. Note that opening and closing do not affect the white rectangle at the bottom of the image, since it is bigger than 2×2 pixels.

employing a local derivative operator that examines gradients in a certain way. As an example, the gradient operator:

$$\nabla \boldsymbol{f} = \begin{bmatrix} G_x \\ G_y \end{bmatrix} = \begin{bmatrix} \frac{\partial f}{\partial x} \\ \frac{\partial f}{\partial y} \end{bmatrix} \tag{4.1}$$

can be discretised to operate over a neighbourhood surrounding the pixel of interest. These *kernels* are then convolved with the image to produce the gradient image. Sobel and Feldman (1968) proposed the following kernels:

$$G_x = \begin{bmatrix} 1 & 2 & 1 \\ 0 & 0 & 0 \\ -1 & -2 & -1 \end{bmatrix} * I; \quad G_y = \begin{bmatrix} 1 & 0 & -1 \\ 2 & 0 & -2 \\ 1 & 0 & -1 \end{bmatrix} * I \tag{4.2}$$

$$G = \sqrt{G_x^2 + G_y^2} \tag{4.3}$$

The MATLAB script *edge* allows use of the Sobel method, along with many others.

4.2.1.1.5 Masking The viewable area of the camera has to be a rectangle, and, to best fit the circular windows, is chosen to be a square. Hence there are areas in the corners of the image which are of no value. However, due to the bevel on the window caps, light from the combustion can still appear in these areas and lead to erroneous results in the image processing. Hence it is best to remove these areas by masking.

A mask is a matrix of binary elements designed to be the same size as the image matrix. When the two matrices are multiplied element-wise, a zero in the mask matrix will lead to an image pixel being made black, as a one will render it unchanged, since $0.x \equiv 0$ and $1.x \equiv x$.

In this case the mask needs to be a circle of ones (white) corresponding to the circular window area against a background of zeros (black). In early cases this was just made in Microsoft Paint by drawing a white circle of the correct size on a black background, saving it as a binary bitmap and then importing into MATLAB. However,

this requires the windows to be accurately aligned with the camera for all images. As it is prone to moving slightly over a period of days, a MATLAB script was written to dynamically generate a mask matrix, where the size and position of the circle could be entered as parameters. This program *mask* worked by looking at each pixel and calculating if the Euclidean distance between it and the intended centre was greater or less than the required radius of the circle.

4.2.1.1.6 Median Filtering There are many image filtering techniques available, from simple averaging filters, Butterworth types all the way to non-linear diffusion filters. All aim to smooth noise in the image without distortion, especially to edges. A filter was required to remove small inconsequential artefacts prior to thresholding. Median filters are very good at removing random noise without blurring edges (Gonzalez and Woods, 1993). A median filter belongs to the class of order-statistic filters, whose operation derives from statistical ordering rather than computations such as means (Castleman, 1996).

A median filter works by looking at each pixel and the area, or *neighbourhood* around it. The pixels in the neighbourhood are ranked in order of their value and the median value is assigned to the pixel of interest, which is normally at the centre of the neighbourhood. Any size of neighbourhood can be employed, and in some cases not all the pixels in the neighbourhood are used to calculate the median, but here the default size of 3×3 was used with all pixels utilised. The program used was the MATLAB script *medfilt2*.

4.2.1.1.7 Label Matrix Once an image has been thresholded, it will contain one or more islands of white (values that were above the threshold) on a black background. The MATLAB Image Processing Toolbox contains the script *bwlabel* which identifies these islands and assigns them a number. Properties of each island can then determined using *regionprops*. These include the area of the island and the co-ordinates of its bounding box—a rectangular box aligned with the axes which encloses the island so

that the island touches it on all four sides.

It is hoped that one of these objects will be the ring relating to the flame front. However sometimes it is split into two by the gap in the image caused by the electrodes. The largest object will be the masked off area outside the windows. This is simple to eliminate as its bounding box will always in the top left hand corner of the image. Very small artefacts with an area of less than twenty pixels were also eliminated. The remaining islands represent the flame. A box is created which encloses all of these islands. The height of this box was found by inspection to be the best match to the radius of the circle.

4.2.1.2 Intensity Minima Method

As the flame front appears as a dark ring on a lighter background, if one were to take a vertical slice through the image in line with the spark gap, the grey level along that line should decrease at the two points corresponding to the flame front. Detecting the location of these minima would allow calculation of the diameter. This was tested but found not to work reliably.

4.2.1.3 Hough Transform Method

The Hough Transform (Hough, 1962) is a method of discovering shapes from edges (Low, 1991). If the user seeks a particular shape and has done some edge detection on their image, then they will have many points describing the edge of that shape. However, detecting shapes from a cloud of points (some of which may be random noise) is very difficult. The Hough Transform aims to convert this global detection problem in image space into a local peak detection problem in a parameter space relevant to the shape to be found. This is a far easier problem (Illingworth and Kittler, 1988).

Imagine the simple problem of fitting a straight line to the four points shown in Figure 4.5. It is clear that the line should pass through the left hand three points, while the right hand point should be ignored as noise. However, to solve this problem in image space requires a line to be plotted between every pair of points and then to

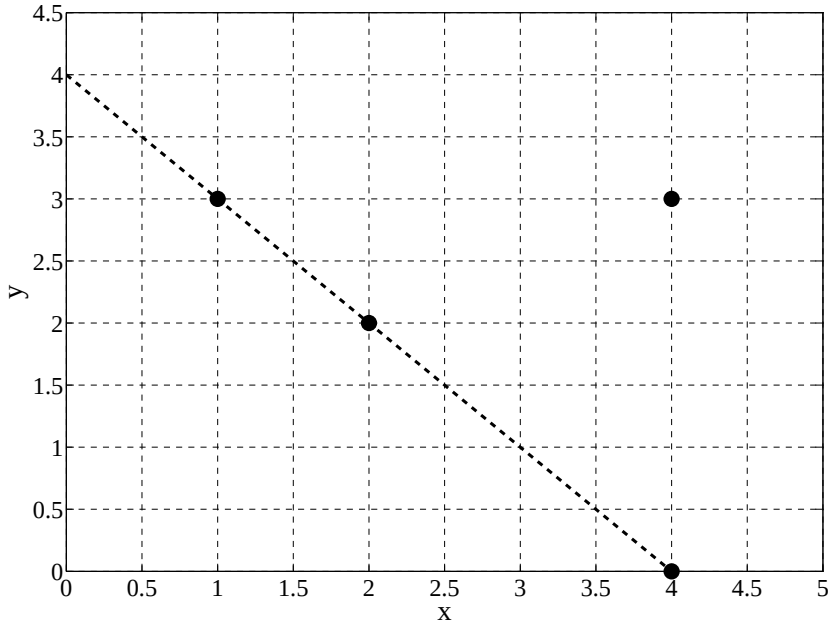

Figure 4.5: A simple shape detection problem

see if that line intersects any other points. This is computationally intensive.

Alternatively, one could rearrange the equation for the shape of interest:

$$y = mx + c \tag{4.4}$$

to make the equation of a second line, where the gradient and y-intercept of the new line are the known co-ordinates of the points x and y:

$$c = (-x)\, m + y \tag{4.5}$$

So for the point at $(1, 3)$ this would become:

$$c = (-1)\, m + 3 \tag{4.6}$$

This line can now be plotted, not in the x-y space of the original problem, but in the parameter space m-c. This can be repeated for the other three points to form Figure 4.6. It is clear that the three lines corresponding to the three non-noise points cross at $(-1, 4)$. Hence the original line that is being searched for must have the

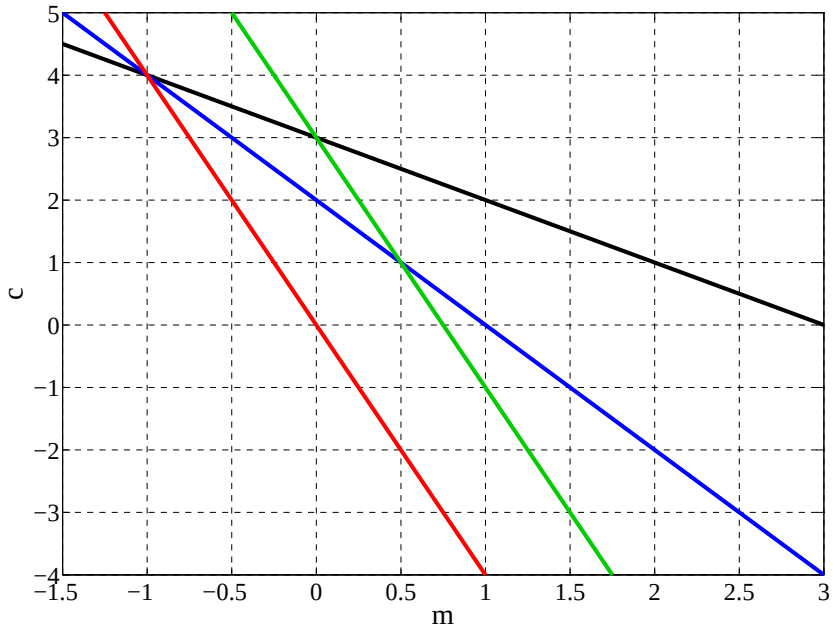

Figure 4.6: The m-c parameter space

equation $y = -m + 4$. Looking back at Figure 4.5 it is clear that this is so.

The usual way to find where the lines cross (technically where the most lines cross, since the green line corresponding to the noise point also crosses the blue and black lines) is to set up an accumulator space. This would consist of a matrix initially full of zeros. Each line is then 'plotted' onto the space by incrementing all the elements of the matrix which lie under the line. This is achieved using the algorithm of Bresenham (1965). This is repeated for all lines so that the intersection of two lines will lead to values of 2 in the matrix. To find the intersection which involves the largest number of lines then involves finding the location in the matrix of the largest element, which is straightforward.

However, the Bresenham algorithm only draws thin lines, meaning that elements only have to be connected by corners, not by edges. This means that, as is shown in Figure 4.7a, two lines can cross without overlapping and causing a peak in the matrix values. This is overcome by modifying the algorithm to draw thick lines, (see Figure 4.7b) so that the lines will definitely overlap and generate the required peak.

Having thicker lines incremented in the accumulator space also allows some margin for error with the exact alignment of the points, bringing resistance to noise on real

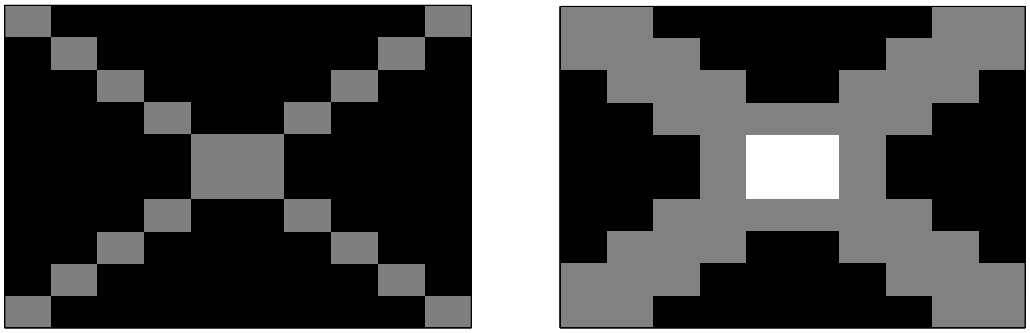

(a) (b)

Figure 4.7: Result in accumulator space when (a) thin and (b) thick lines cross.

data points.

A similar procedure can be extended to the two variable problem of a circle of known radius:

$$r^2 = (x-a)^2 + (y-b)^2 \tag{4.7}$$

$$= (-a+x)^2 + (-b+y)^2 \tag{4.8}$$

Here, for each data point a circle of radius r is plotted, centred at (x, y). The peak in the a-b accumulator space will indicate the centre of the original circle.

As a test of this, twenty random points were plotted on the circumference of a circle of radius 100, centred at $(180, 350)$. A further one hundred random noise points were added (see Figure 4.8).

The Hough Transform was then run on this example. The result was a peak at $(180, 350)$, correctly giving the location of the original circle despite there being five times as many noise points as data points. This would not be possible with other approaches such as least squares fitting. A problem with the accumulator space is that it is possible for circles to overlap the edge of the space, as is seen in Figure 4.9. This causes MATLAB to try and increment an element of the matrix which does not exist. The two solutions are to pad the matrix with r elements all around, or to check that an element is valid before attempting to increment it. Despite the extra computation required by the latter, it becomes the preferable option when one moves

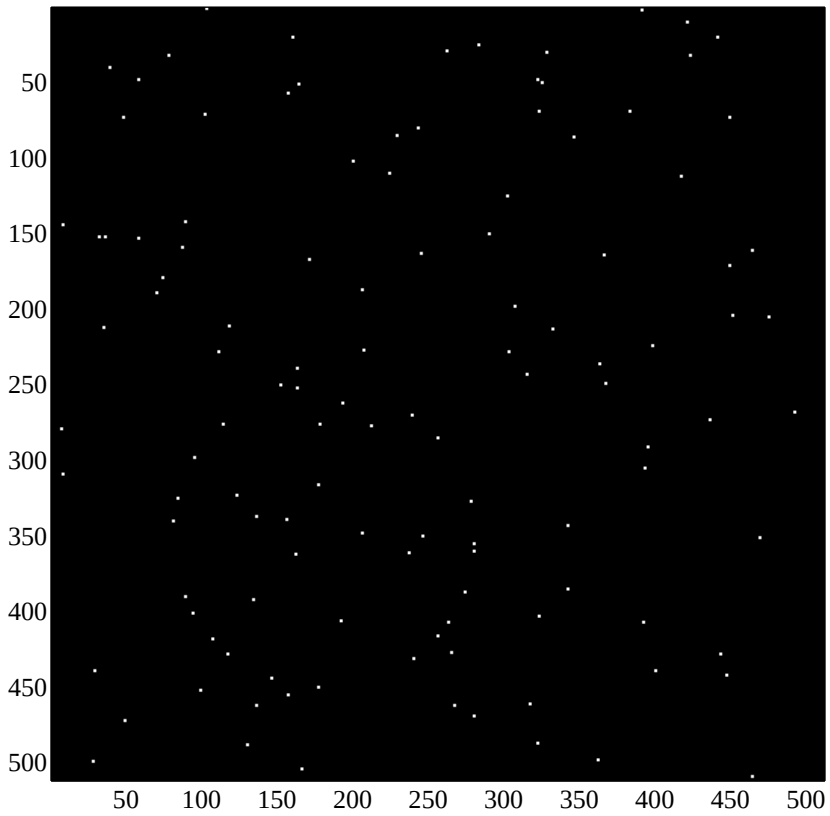

Figure 4.8: Edge of circle with many random noise points. Note that points have been made larger in diagram to aid clarity.

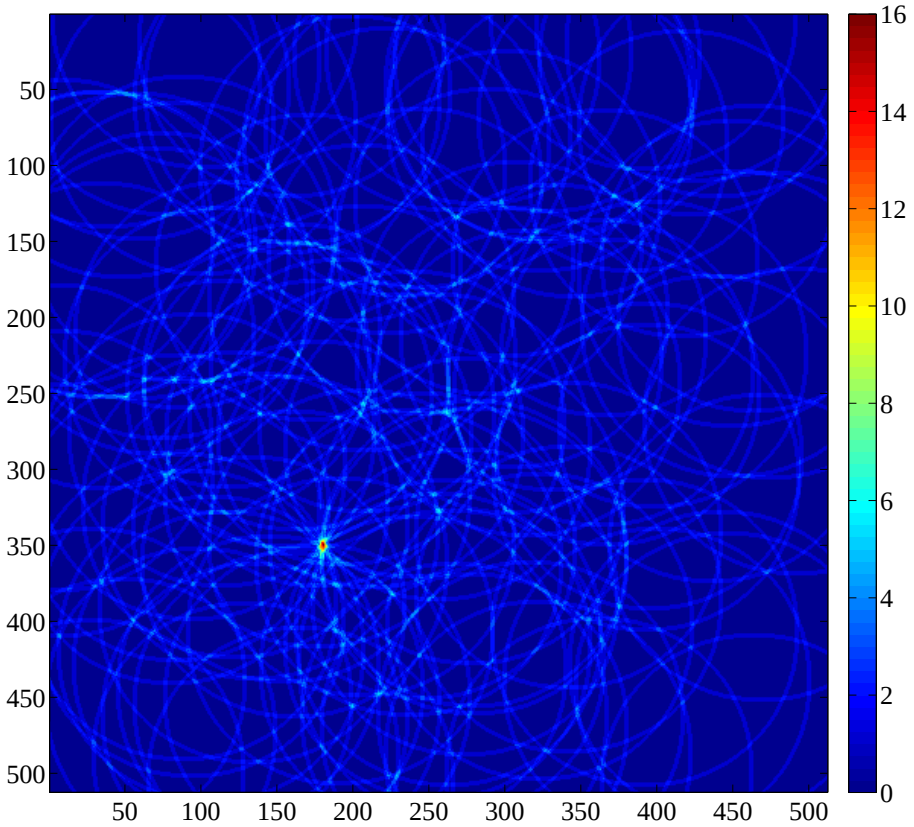

Figure 4.9: *a*-*b* accumulator space showing peak at $(180, 350)$

to very large, multi-dimensional parameter spaces where the extra padding required massively increases the memory needed to store all the elements in the space.

For the problem of the flame front, the radius is not known, and will be changing. Hence each point will become a right-angled cone in (a, b, r) space, corresponding to a circle of unknown radius. The most populated intersection of these cones will be the point in (a, b, r) space corresponding to the co-ordinates of the centre of the flame front circle and its radius. Although the radius is of primary importance, checking the location of the centre may be useful in detecting buoyancy.

Cones were simply constructed by stacking Bresenham-type circles. As the cones are right-angled, the radius of the circle will be equal to the distance from the tip along the cone-axis. This worked very well, but for a real image which may have many thousands of points, plotting all these 3D cones on top of each other became very time consuming. Hence ways were investigated to speed up the process.

Firstly, one can reduce the number of points. The edge detection algorithm will yield points around the edge of the flame front, but it will also give many points corresponding to artefacts both inside and outside the flame which are not of interest. These can be avoided by masking (see Section 4.2.1.1.5) both outside the circle and inside. These masks can be actively generated with prior knowledge of the approximate expected radius of the flame so that they cover as much of the uninteresting space as possible.

Secondly, one can cut down the size of the parameter space. It is clear that in a 512×512 image, the flame is unlikely to the be centred anywhere near the corners. Similarly, the radius is unlikely to be less than it was in the previous frame. Hence the size of the parameter space can be reduced, while still ensuring that the peak will occur within the bounds of that space.

Once the parameter space is quite small compared to the image, it may be that some of the cones to be plotted will not intersect it at all. As they are right-angled cones, this is easy to predict, and means that time is not spent testing every element in the cone to see whether it lies within the bounds of the parameter space when none

of them do.

4.2.1.4 Cross-Correlation Method

As we have knowledge of the shape to be detected and its approximate position and size, we could generate an artificial circle of the expected size and position and see how well it compares to the real image. This comparison would be done by cross-correlating the two images to form a difference image. A cost function could then be devised to describe the magnitude of the difference, and minimisation code used to adjust the size and position of the artificial circle to match the real one. Once a suitable match was achieved, the dimensions would then be known.

A simple demonstration was made with a white circle on a black background. A second white circle was placed repeatedly at random positions until there was some overlap between the two. The minimisation code then started, attempting to adjust the position and size of the second circle to maximise the overlap between the two. Although this worked quite well, it was considered that extending the method to noisy dark rings would be too difficult.

4.2.1.5 Fast Fourier Transforms

Normally, a Fourier analysis would be performed on some data varying as a function of time, yielding a frequency spectrum. However, it is equally possible to analyse data which varies as a function of position. In this case the result is a spectrum of wavenumber, the spatial analogue of frequency.

A monochrome image matrix is simply a grey level varying as a function of two spatial dimensions. Hence patterns may be detectable using Fourier Transforms. The dark ring of the flame front against a light background can be inverted to give two peaks when a slice is taken across the image in any direction. Hence there is some basic periodicity, based around the centre.

Sample images were made to inspect their FFTs, but no useful data could be gleaned from them. The problem is that the FFT assumes the function is continuous.

It does this by tiling the image so that the pattern continues to infinity. Hence there are two characteristic wavenumbers — the space between the peaks in the image, and the space to the first peak in the next image.

A possible solution to this problem is to use a windowing function, but it was again decided that this method was too complicated and fundamentally not suited to the problem due to the very low number of repetitions of the pattern in the image.

4.2.1.6 Final Algorithm

Although a reasonable Hough Transform algorithm was developed, it was very slow and struggled at small radii when the flame was not particularly circular.

The first algorithm used on a large scale was written by the author. It used thresholding and bounding boxes to find the radius, and utilised the following steps:

1. Background division
2. Median filtering
3. Masking
4. Rotating by 45° so that the difficult area where the electrodes intersect the flame were not at the 90° and 270° positions where they were more likely to affect the size of the bounding box
5. Threshold using fixed level of 0.95
6. Create label matrix
7. Get region properties
8. Exclude area outside windows
9. Exclude very small regions
10. Fit bounding box to remaining regions
11. Find height of bounding box

This algorithm was then modified to the final version by Taylor (2008). Taylor's algorithm used the steps (see Figure 4.10):

1. Median filtering
2. Background subtraction
3. Threshold
4. Remove small regions
5. Morphological closing operation with disk of diameter equal to that of the electrodes. The circular shape of the flame is convex while the gaps caused by the spark plug elements are concave, so this has the effect of filling in the gaps caused by the electrodes.
6. Find area and assume circular shape to find equivalent radius

The region that was detected as flame was not always circular, particularly when the flame was very small or the density difference caused only a small change to intensity. Also, the assumption that the flame was spherical was not always valid. To prevent the function returning radii calculated when this was the case, a measure of circularity is calculated. The measure is:

$$P_{\text{calculated}} = 2\pi R_{\text{calculated}} \tag{4.9}$$

$$\text{circularity} = \frac{P_{\text{actual}}}{P_{\text{calculated}}} \tag{4.10}$$

This measure equals one for a perfect circle and increases for any other shape. By only returning radii when this measurement was sufficiently close to one the output of the function was made far more robust.

As the flame front always moves out from a central origin, regions of detected flame can be retained for use in future frames. This allows a more noise resistant set of thresholds to be used in detecting the flame front, making it more likely that a full circle will be detected and increasing the reliability of the output.

The background can move slightly during the experiment. Although the movement is only by a few pixels, this creates long, thin regions on the edges of the electrodes and window which are dark after the background subtraction. As the flame front is a thin dark ring it is very hard to differentiate between this and the erroneous areas caused by the background movement. To prevent these regions from surviving the background subtraction, once the flame has been detected in a frame, the background is updated everywhere that does not contain flame. This reduces the effect of background movement and results in a more robust function that can operate on more video sequences.

4.2.2 Cellularity Detection

As is explained in Section 2.8.6, the onset of cellularity means that calculating burning velocities using the pressure record is no longer possible. Without optical access, the onset of cellularity has to be guessed by examining the plot of burning velocity against pressure for a sudden jump in burning velocity. It is important to have a reliable method of automatic, objective cellularity detection to ensure that data compromised by cellularity is not used. Taylor (2008) was able to incorporate such an algorithm into his radius detection code.

Cellularity appears as the flame front rapidly segments (see Figure 4.11). This can be detected by using an edge detector (see Section 4.2.1.1.4) on the region known to be within the flame front. The rapid segmentation caused by cellularity results in a rapid and prolonged increase in the number of edges that can be detected. The MATLAB edge detection function requires a threshold to decide how strong an edge should be before it is returned as a genuine edge. The *edge* function can set a threshold level automatically, but it must be fixed to produce a reliable account of how the number of edges is changing between frames. Otherwise a different threshold may be chosen for each frame, which would be inconsistent. Calculation of a suitable threshold level was achieved by first performing an edge detection on each frame and selecting the largest

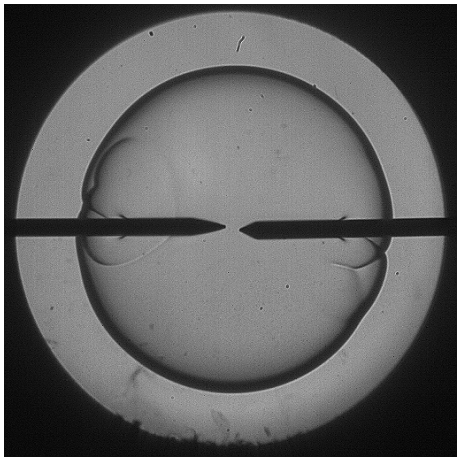

1. Original image

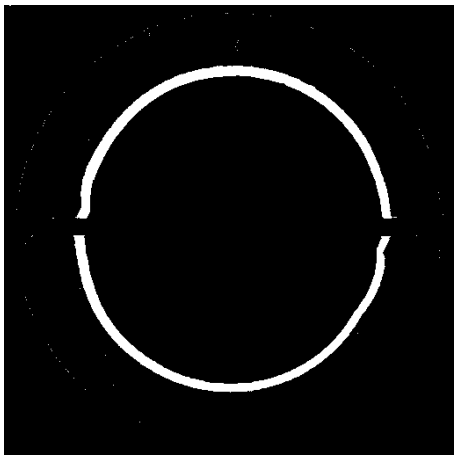

4. Threshold

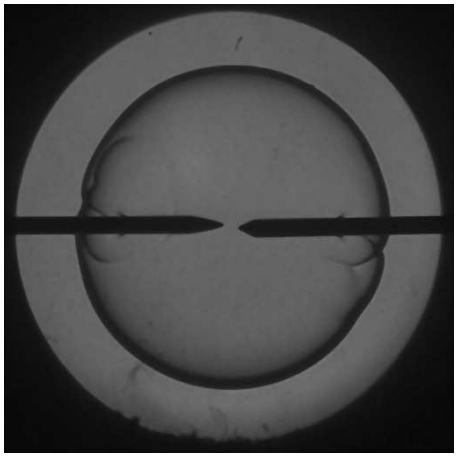

2. Median filter

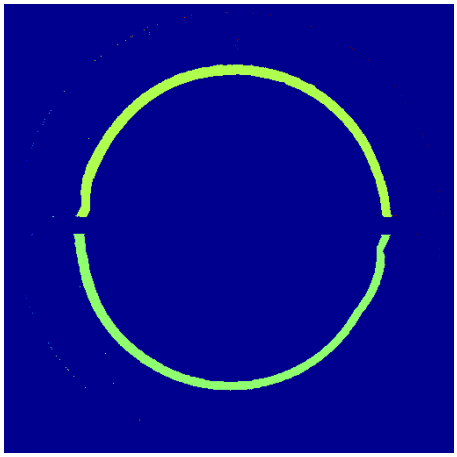

5. Label matrix

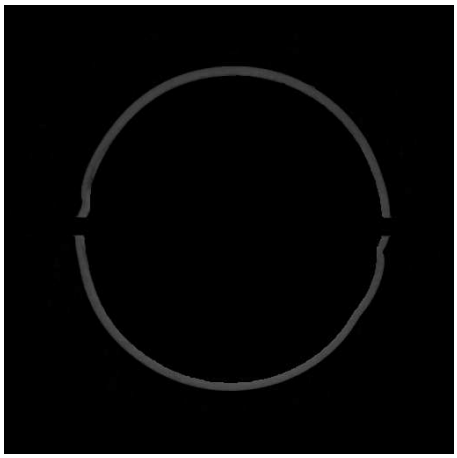

3. Background subtraction

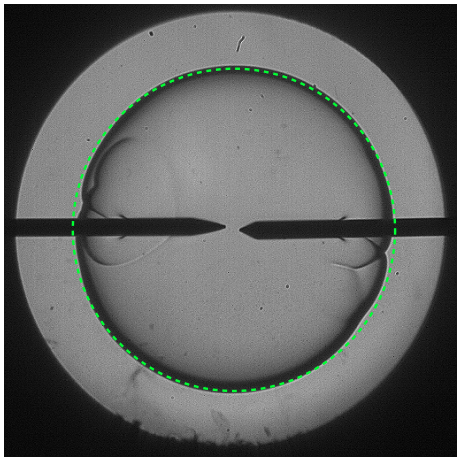

6. Original image with calculated radius overlay

Figure 4.10: Image processing steps.

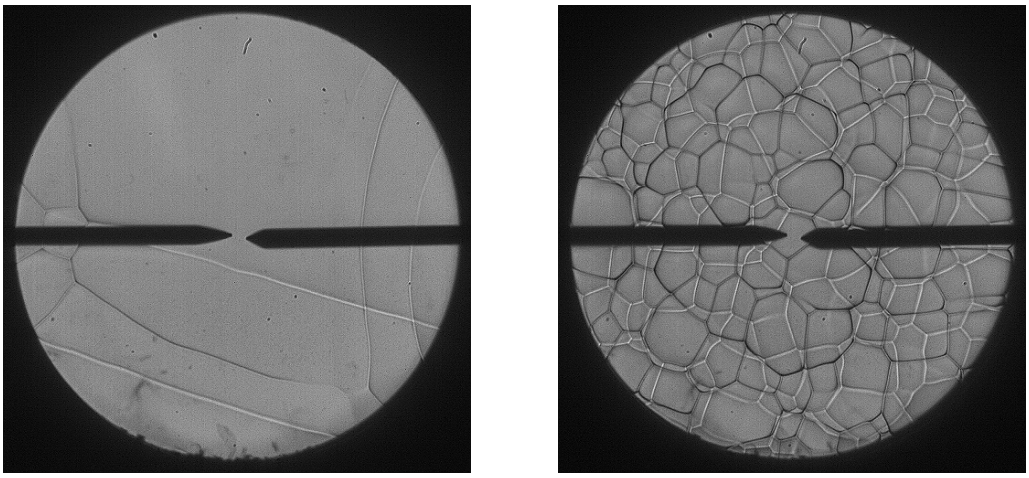

(a) Cracked (b) Cellular

Figure 4.11: A (a) cracked flame expanding to become (b) fully cellular.

automatic threshold that *edge* chooses. Edge detection was then performed on each frame in the sequence using this fixed threshold and the number of edges detected is recorded. Once all of the frames have been processed, the series of numbers of edges is smoothed with a moving average filter and the result differentiated. Large, wide peaks are then detected and flagged as cellularity events. The frame number of the first of these events is taken to indicate the onset of cellularity.

The frame number is converted to a time from ignition. From the pressure record, the pressure at this time can be found, and from the BOMB program the radius can be found, as well the burning velocity, flame speed, stretch rate and unburned gas temperature. These parameters are stored for each experiment in the series.

Both this code and the radius detection code described in Section 4.2.1.6 are incorporated into the function *refreshbg*.

4.3 The BOMB Program

The *BOMB* program is based on the *ISIS* program for calculating the NO_x levels emitted from a spark ignition engine. This was written by the Oxford Engines Group in FORTRAN 77 (Raine et al., 1995), based on the routines of Ferguson (1986). This is a multi-zone numerical model as described in Section 2.4.1.6.3. Given the fuel under

test, the equivalence ratio, residuals fraction, initial pressure and initial temperature, it solves the composition for the equilibrium of ten major combustion products for each zone.

The BOMB program solves the conservation equations for energy and mass in a constant volume chamber. It assumes negligible flame front thickness and has the option of a multi-zone model. In practice the flame front and the preheat zone (a thermal boundary layer) will be separating the burned and unburned gases.

The program outputs are in the format of text files. For each experiment (i.e. each combination of initial conditions), two text files are generated - a *data* file and a *zone* file. Together they provide the following information:

1. Combustion
   (a) Mass fraction burned
   (b) Flame radius
   (c) Pressure
   (d) Composition of the burned gas in terms of CO_2, H_2O, N_2, O_2, CO, H_2, H, O, OH and NO_x
2. State of the unburned gas
   (a) Temperature
   (b) Specific volume
   (c) Ratio of specific heats γ
3. State of each zone
   (a) Radius of the boundaries r_b
   (b) Temperature
   (c) Specific volume of the gas

4.3.1 BOMB Options

The *BOMB* program can be run from an MS-DOS prompt. However, this requires typed data entry to multiple prompts, which takes a long time. Hence a batch file was used to run the program with an input file, which contains the input data as it would be entered by the operator. This allows values to easily be changed using a text editor, and the input file can be saved for later use.

Many of the options relate to the original ISIS program and hence are obsolete. This does not however mean they can necessarily be ignored, but they do not need to be changed. The important options are explained below.

4.3.1.1 Fuel Ideal Gas Properties

Specific heats, enthalpies and entropies are calculated for a given temperature by reference to known polynomials, with coefficients given for the fuel under test. The structure of these polynomials follows that used by Ferguson (1986):

$$\frac{c_\mathrm{p}}{R} = a_0 + b_0 T + c_0 T^2 \tag{4.11}$$

$$\frac{h}{RT} = a_0 + \frac{b_0}{2} T + \frac{c_0}{3} T^2 + \frac{d_0}{T} \tag{4.12}$$

$$\frac{s^0}{R} = a_0 \ln T + b_0 T + \frac{c_0}{2} T^2 + e_0 \tag{4.13}$$

Ferguson (1986) provides coefficients for some fuels, including methane, methanol and benzene. Unfortunately, data were not available for the other fuels of interest in this format. Instead, a third order polynomial for specific heat capacity with respect to temperature from Reid et al. (1987) was plotted and a quadratic fitted to it to generate a_0, b_0 and c_0. As the cubic term was generally very small, this reduction in order introduced very little error. The d_0 and e_0 enthalpy and entropy terms were calculated using these coefficients together with the enthalpy of formation, Gibbs energy of formation and absolute entropy from Daubert and Danner (1997).

Also required are the higher and lower gravimetric calorific values, which can be

calculated from the enthalpy of formation of the fuel and those of CO_2 and H_2O which were found from Atkins (1994).

A MATLAB program was written to calculate all the required data. These data are written to a plain text fuel data file, which is read by the BOMB program. The fuel file also contains a second law term, which is the difference in the Gibbs energies of the products and reactants. This is not required for the BOMB program but is present due to its requirement for the original ISIS program.

4.3.1.2 Number of Zones

A discussion of the number of zones is presented in Section 2.4.1.6.3. Ten zones and two hundred steps were used throughout this study.

4.3.1.3 Burn Rate Type

Considering its parentage as an engine combustion simulation, the BOMB program has the option of six different burn rates. These would have originally been mass fraction burned as a function of crank angle. This option decides the formation of the zones. A linear burn rate leads to zones formed on the basis of equal mass. The change in mass fraction burned between the beginning and end of combustion in each zone is the same. The second option is a cubic burn rate, which leads to zones with equal radius. Hence later zones will contain more mass. The equal mass option was used. This made interpolation in the zone file easier (see Section 4.6.1).

4.3.1.4 Initial Conditions

The equivalence ratio, molar residual fraction, initial temperature and initial pressure all have to be set. These are expressed as a start value, end value and step size, so that multiple conditions can be evaluated. These lead to multiple sequentially numbered text files being generated. As an example, if the equivalence ratio input were set to be 0.8 1.2 0.1 then equivalence ratios of 0.8, 0.9, 1.0, 1.1 and 1.2 would be simulated.

4.3.2 Visualising Output

A program was written to visualise the BOMB program output. This can show the radii and temperature of the zones. For the same experiment (methane, $T_0 = 298$ K, $p_0 = 1$ bar, $\phi = 1$, $x_r = 0$), the BOMB program was run with five zones and fifty zones. These files were used to generate Figure 4.12. The left hand column shows five zones burning, with the flame front in red. This shows how the radii of the zones increase as they are compressed outwards by the inner zones burning. This happens until they themselves are burned, at which point their radii decrease again as they are compressed inwards. The right hand column shows fifty zones burning to show the temperatures of the zones. This further demonstrates the recompression in the burned gas, with the peak temperature in the centre (i.e. zone 1).

4.4 Experimental Summary Spreadsheet

The experimental summary spreadsheet is an Excel spreadsheet which is read by several MATLAB programs to give them information about the experiments in a batch. The file contains the following columns:

1. Experiment number
2. Equivalence ratio
3. Initial temperature (K)
4. Initial pressure (bar)
5. Residuals mole fraction
6. A Boolean describing whether the pressure data should be included in the analysis
7. A Boolean describing whether schlieren images should be used in the analysis
8. The window diameter in pixels

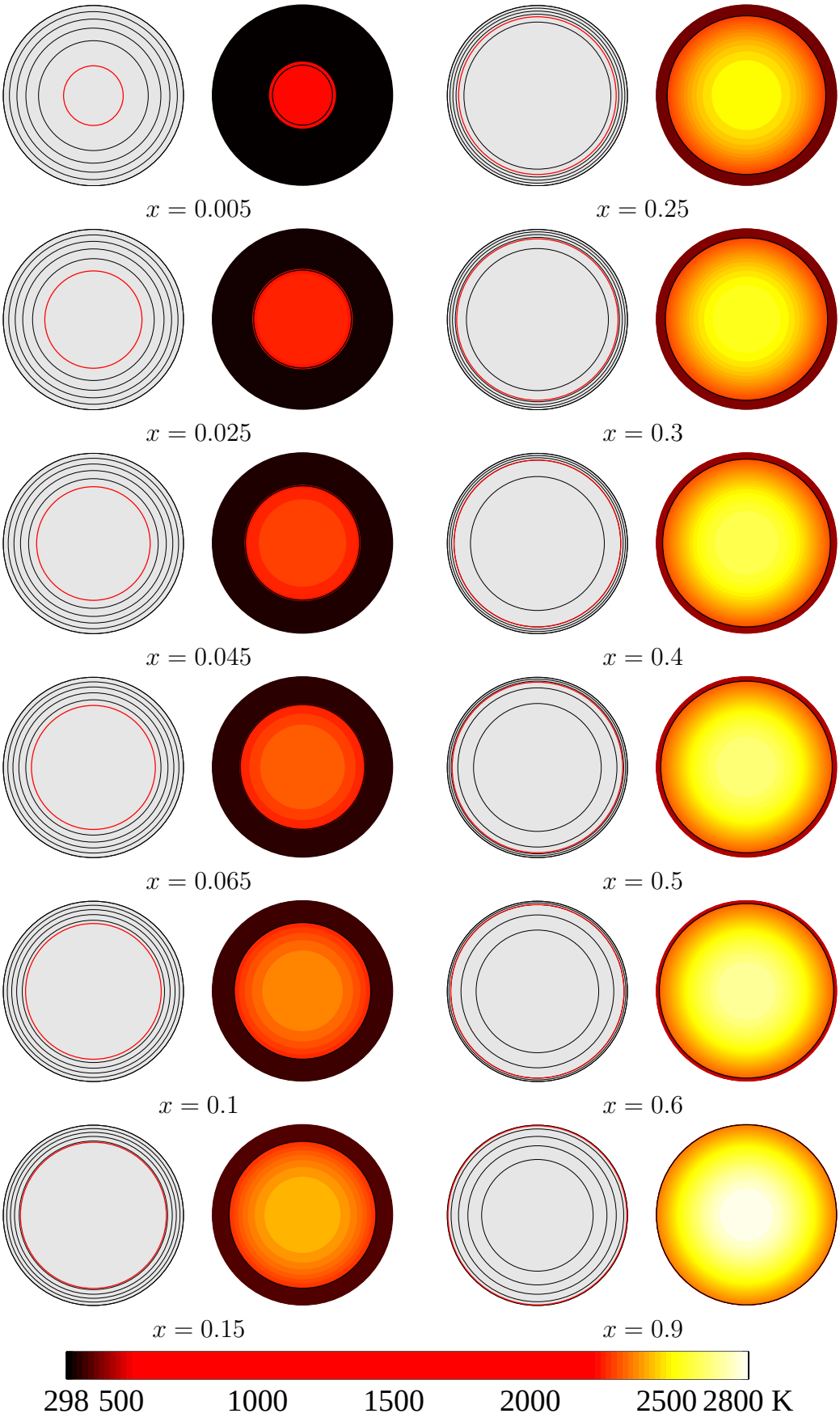

Figure 4.12: BOMB program radius and temperature outputs.

4.5 *BVImage* Program

The *bvimage* program has been written in MATLAB. It takes the zone file output from the BOMB program and the TIFF images from the experiment and uses these to calculate burning velocity against time and detect any cellularity.

The sub-program *refreshbg* described in Section 4.2.1.6 analyses each experiment in turn, returning the radius of the flame, the velocity and the time at which any cellularity occurs.

For each frame the radius was used to find values of unburned gas specific volume, pressure, unburned gas temperature and the mass fraction burned from the zone files by interpolation. The burning velocity was calculated from the flame speed from refreshbg multiplied by the ratio of the unburned and burned specific volumes:

$$S_{\mathrm{u}} = \frac{\mathrm{d}r_{\mathrm{b}}}{\mathrm{d}t}\frac{v_{\mathrm{u}}}{v_{\mathrm{b}}} \tag{4.14}$$

where the burned gas specific volume was found from the first time step available in the zone file:

$$V_0 = \frac{4\pi}{3}\left(R^3 - r_0^3\right) \tag{4.15}$$

$$m_{\mathrm{t}} = \frac{V_0}{v_{\mathrm{u}0}} \tag{4.16}$$

$$m_{\mathrm{b}} = x m_{\mathrm{t}} \tag{4.17}$$

$$v_{\mathrm{b}} = \frac{4\pi}{3}\frac{r_{\mathrm{b}}^3}{m_{\mathrm{b}}} \tag{4.18}$$

The stretch rate is found by:

$$\alpha = \frac{2}{r_{\mathrm{b}}}\frac{\mathrm{d}r_{\mathrm{b}}}{\mathrm{d}t} \tag{4.19}$$

This process was repeated for each experiment in the batch and all the data was concatenated in a large S_{u} matrix containing:

1. burning velocity

2. flame speed
3. equivalence ratio
4. pressure
5. temperature
6. initial pressure
7. initial temperature
8. residuals molar fraction
9. stretch rate
10. flame radius
11. time
12. experiment number

The conditions at the onset of any cellularity were also saved for each experiment.

4.5.1 Stretch Extrapolation

Due to the small flame radius and high flame speed, the burning velocity results from the schlieren images will be highly stretched, which will affect the burning velocity. It would be advantageous to be able to extrapolate to zero stretch to find the unstretched burning velocity. This is possible, because the mass fraction burned is low enough that pressure and temperature will not have increased significantly. However, as is discussed in Section 2.7.5, extrapolation can be highly error-prone unless there is a clear trend and data down to a sufficiently low stretch rate.

Figure 4.13 shows a plot of stretched burning velocity against stretch rate for iso-octane with $\phi = 1.1$, $T_0 = 380$ K, $p_0 = 4$ bar and $x_r = 0$. Stretch rate data extends down to approximately 240 s^{-1}. Several different extrapolation schemes were tested,

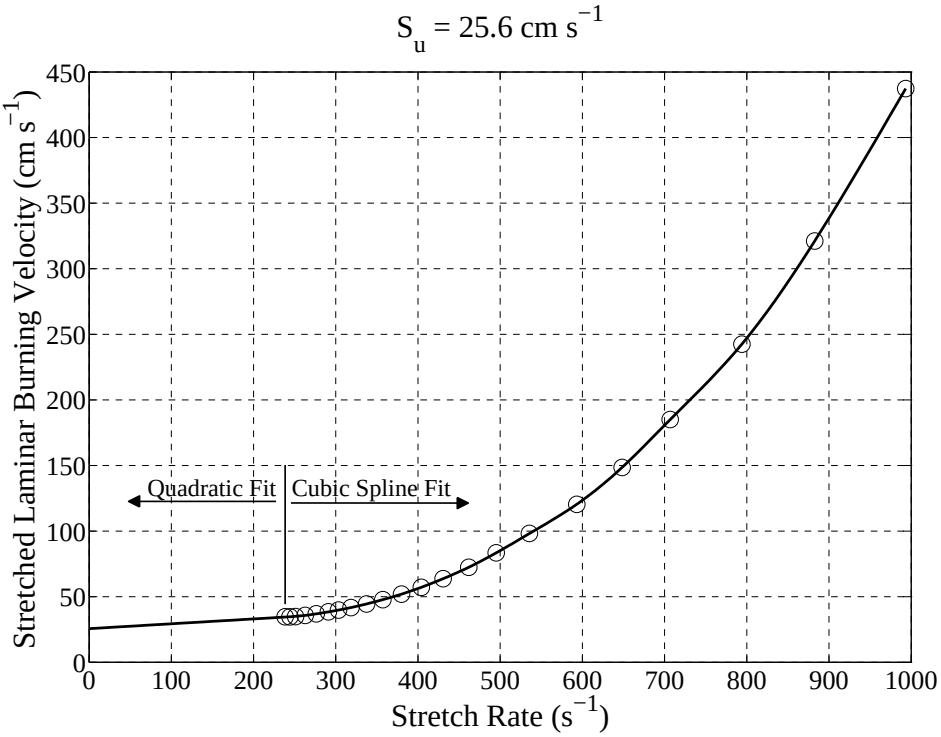

Figure 4.13: Spline extrapolation of schlieren stretch data to find unstretched burning velocity.

and Figure 4.13 shows a cubic spline fitted to the data. A second spline was then created which agrees with the first in the range where there is data, but takes the form of a quadratic outside the range, while meeting smoothness conditions at the join.

Although this seems to give a reasonable result for this one case, trying this method with other experiments led to poor results. The extrapolation was very sensitive to the last few data points available (i.e. those with the smallest stretch rate), and also the number of data points at high stretch rate which were included in the fit. Furthermore, it was found for many experiments that the lowest stretch rate data point had a slightly higher burning velocity than the point before it, possibly due to the partial overlap of the flame front and the edge of the window in the schlieren image. This data point had to be ignored, or else it would cause an extrapolation up to a very high value of unstretched burning velocity.

The poor accuracy in this extrapolation meant that it was not used further. Although the windows in the bomb are a useful asset, particularly for detecting cellularity, they really need to have a larger diameter to give low stretch rate burning velocity data

which could be extrapolated to the stretch-free condition more easily.

4.6 *Burnvel* Program

The *burnvel* program has been written in MATLAB. It takes the zone file output from the BOMB program and the experimental pressure data from LabView (see Section 3.8.2) and uses these to calculate burning velocity.

It reads the experimental summary spreadsheet to find the conditions for each experiment. It then passes the file paths of the appropriate experimental data file and zone file to a sub-program, *bvcalc*, which does the calculations.

4.6.1 *Bvcalc*

The program *bvcalc* reads in the zone file and the experimental data file. Pressure data after the peak pressure is discarded. As the bomb pressure is measured using a piezo-electric pressure sensor, the experimental pressure will always be the pressure above the initial pressure. Hence, to get the absolute pressure the initial pressure must be added to the recorded pressures. However, the experimental pressure record does not normally start at zero, due to small offsets in the charge amplifier and the calibration curve of the pressure transducer. Neither can the first data point be taken as a datum, since this is often greater that the subsequent data. This 'pressure dip' is thought to be caused by HT noise from the spark. This was confirmed by running the data acquisition but without the spark (see Figure 4.14). Consequently, the datum pressure is taken as a mean of the pressure measurements taken between 3 and 4 ms. After that time there will be a small pressure rise due to combustion.

4.6.1.1 Filtering

The experimental pressure data is then passed through a low-pass filter. This helps to reduce noise which is amplified by the subsequent differentiation. This is done using a fourth order Butterworth filter with a normalised cut-off frequency of 0.1. The

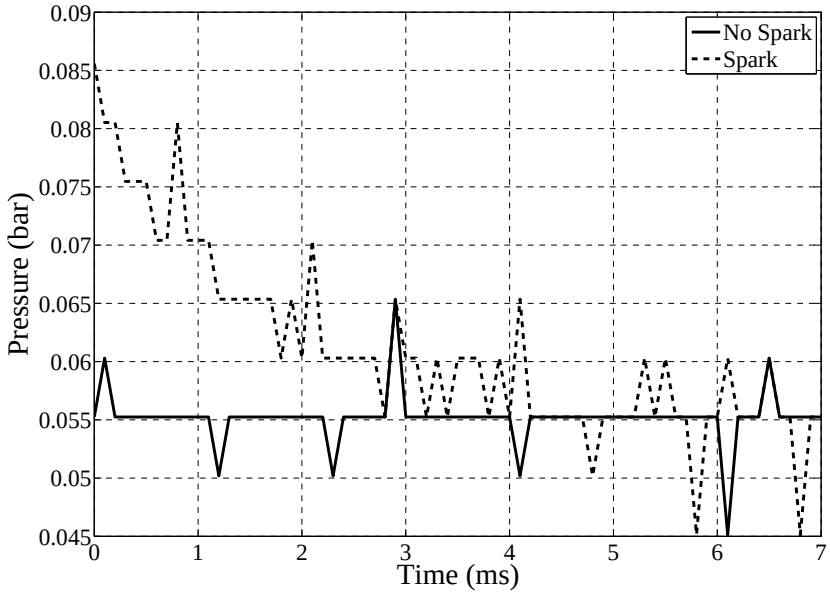

Figure 4.14: Comparison of pressure traces in atmospheric air with and without spark, showing 'pressure dip' effect due to HT noise.

normalized cut-off frequency is a number between 0 and 1, where 1 corresponds to the Nyquist frequency. Plots were produced with typical experimental data in order to determine suitable filter parameters.

The program then matches up the experimental pressures with those in the zone file, where pressure and other parameters are tabulated against mass fraction burned. This was used to interpolate a value of the mass fraction burned, flame radius and gamma (ratio of specific heats) of the unburned gas for each experimental pressure data point.

The program calculates the burning velocity for each data point using Equation (2.36):

$$S_{\mathrm{u}} = \frac{\mathrm{d}r_{\mathrm{i}}}{\mathrm{d}t}\left(\frac{r_{\mathrm{i}}}{r_{\mathrm{b}}}\right)^{2}\left(\frac{p_{\mathrm{i}}}{p}\right)^{\frac{1}{\gamma_{\mathrm{u}}}}$$

The radius of a mass fraction before any combustion r_{i} can be found (see Figure 2.6) by relating the initial volume of a given mass fraction x with the total volume of the

vessel:

$$x = \frac{\frac{4}{3}\pi r_{\mathrm{i}}^3}{\frac{4}{3}\pi R^3} \tag{4.20}$$

$$= \frac{r_{\mathrm{i}}^3}{R^3} \tag{4.21}$$

$$r_{\mathrm{i}} = \sqrt[3]{x \cdot R^3} \tag{4.22}$$

The flame radius r_{b} is found from the zone file as described above. The r_{i} data is also filtered prior to differentiation to reduce numerical noise. In this case a normalised frequency of 0.07 is used. The differentiation was done using the MATLAB function *gradient*. The burning velocity can then be calculated, remembering that p_{i} is the initial pressure and p is the experimental pressure.

The stretch rate is also calculated using Equation (2.123):

$$\alpha = \frac{2}{r_{\mathrm{b}}} S_{\mathrm{f}}$$

For each experimental file, a graph of burning velocity against pressure is plotted (see Figure 4.15). On top of this may be plotted a red vertical line indicating the estimated onset of cellularity, if it was detected by the *bvimage* program. This pressure is found by comparing the time at which cellularity first occurred with the experimental pressure trace. The accompanying radius is calculated from the zone file.

The user then needs to select the range of data to be included in the correlation fitting. This is done by clicking on the figure on the screen at the start and end points of the region of interest, so as to eliminate the noisy data at low pressures and data affected by cellularity and heat transfer to the bomb at high pressures. Clearly selecting data after the indicated onset of cellularity is not recommended. The data from the window of interest is then sent back to the parent program *burnvel*. This process is repeated for each experiment in the batch and all the data is concatenated in a large S_{u} matrix containing the same data as is output from the *bvimage* program

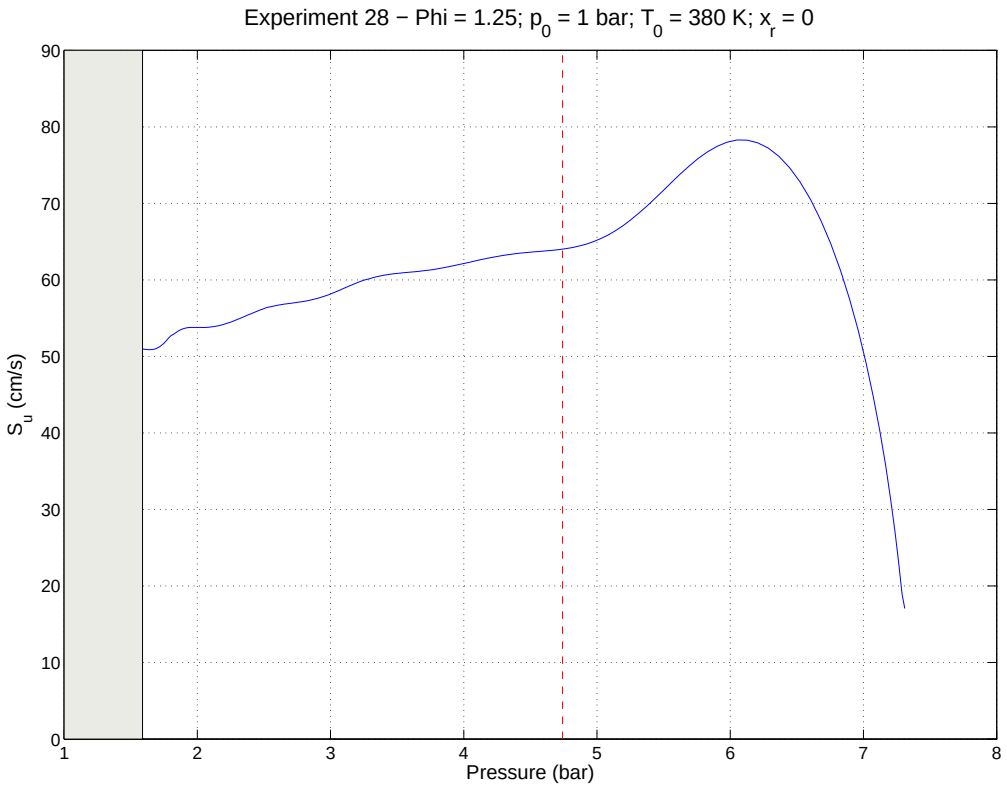

Figure 4.15: Example of a graph of burning velocity. The lower limit has already been chosen by the user, hence the area to the left of the limit is greyed. The red dashed line shows the onset of cellularity calculated from image analysis. It can be seen that this occurs shortly before a rise in burning velocity due to the increased surface area.

(see Section 4.5).

A batch may contain several hundred experiments due to the large number of combinations of the variables, as well as repeats. This can add up to tens of thousands of data points.

4.7 *Fitcorr* Program

4.7.1 Current Correlation

As mentioned in Section 2.6, many different correlations have been fitted to burning velocity data. Clarke (1994) extended the correlation of Metghalchi and Keck (1982) to:

$$S_{\mathrm{u}} = \left[S_{\mathrm{u},0} + S_{\mathrm{u},1}\left(\phi - 1\right) + S_{\mathrm{u},2}\left(\phi - 1\right)^2 + S_{\mathrm{u},3}\left(\phi - 1\right)^3 + S_{\mathrm{u},4}\left(\phi - 1\right)^4\right] \times T^{\eta} p^{\beta} \tag{4.23}$$

where:

$$T = \frac{T_{\mathrm{u}}}{298} \tag{4.24}$$

$$p = \frac{p_{\mathrm{u}}}{1.0} \tag{4.25}$$

$$\eta = \eta_0 + \left(\phi - 1\right)\eta_1 \tag{4.26}$$

$$\beta = \beta_0 + \left(\phi - 1\right)\beta_1 \tag{4.27}$$

Given the increase in computational power now available and further insight into burning velocity behaviour, the decision had to be made whether to keep this correlation or to make improvements.

4.7.2 Choice of Correlation Form

4.7.2.1 Burning Velocity Modelling

Modelling of the burning velocity of methane was carried out by Crina Heghes using the MIXFLA package (Warnatz, 1978a,b,c). This program calculates the speed and structure of stationary premixed one dimensional laminar flat flames. The conservation equations for the total mass, the species masses and the enthalpy are solved. It was written in FORTRAN 77.

A new C_4 mechanism by Heghes (2006) was used, which uses rate parameters as recommended by the CODATA project (Baulch et al., 2005). This mechanism consists of 412 elementary reactions and 61 species. The approximate temperature range is 900–2500 K. It can predict the burning velocities of H_2, CO, CH_4, C_2H_6, C_3H_8, n$-C_4H_{10}$ and i$-C_4H_{10}$.

Two methane data sets were available. The first was stoichiometric data with pressures from 1 to 50 bar and temperatures from 298 to 800 K. The second was data at a fixed temperature of 298 K with pressures from 0.5 to 50 bar and equivalence ratios from 0.8 to 1.4. No residuals were modelled. There were 92 data points in total. Some of this data has previously been published by Heghes et al. (2005), where it was shown to compare well with the experimental data of Vagelopoulos and Egolfopoulos (1998) and Rozenchan et al. (2002). This data was used to validate the form of the correlation used to fit the experimental burning velocity data. It was then compared to the methane experimental results (see Section 6.3).

The modelling data allowed analysis of the form of the correlation. Previously, the only way to do this was to run different forms of the correlation for a set of experimental data and see which fitted the data with the smallest residuals. The modelling data could be treated as perfect data, allowing examination of parameters one at a time. However, where there are only a few data points, one must be careful to fit the trend, not just the data points. This is especially true for the equivalence ratio term where the correlation has a high order.

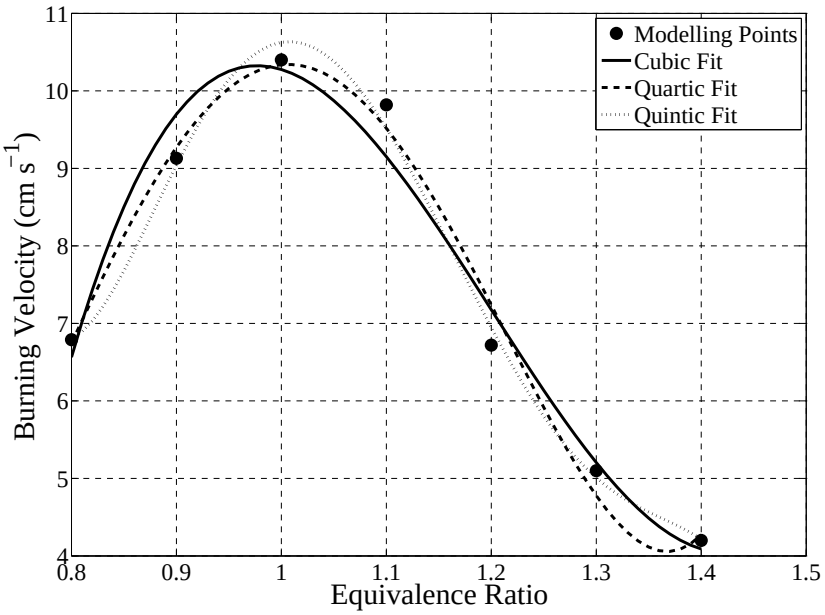

Figure 4.16: Methane modelling data at 10 bar and 298 K fitted by three different orders of polynomial, using a least squares algorithm.

4.7.2.2 Equivalence Ratio

The modelling data was used to examine the quartic expression which describes the effect of equivalence ratio. For the data with a fixed temperature of 298 K, burning velocity was plotted against equivalence ratio for different pressures (see Figure 4.16 for an example at 10 bar). The data points for each pressure were fitted well by the quartic. Reduction to a cubic equation did not work well, particularly at lean conditions. At low pressures, additional points of inflection were evident at high and low equivalence ratios, giving 'tails' to the curve. These were captured by the fourth order term. Addition of a fifth term gave little benefit.

The three functions (cubic, quartic and quintic) were tested with the minimisation code (see Section 4.7.3), using four different data sets. The first was the fixed temperature (298 K) half of the modelling data. The second was the whole modelling data set. This should be very similar to the first, since the second half is all stoichiometric data, which will not be affected by the number of $(\phi - 1)$ terms. Lastly, the methane and iso-octane experimental data sets were used. In each case, the mean absolute error for each point between the data points and the value of the correlation at the same

Table 4.1: Comparison of mean error (cm s^{-1}) between modelling/experimental data and the correlation fit to the data for different orders of equivalence ratio function.

Data Set	Cubic	Quartic	Quintic
Modelling fixed temp	1.4259	1.3984	1.3996
Modelling all	2.0882	2.0924	2.0850
Experimental methane	1.3337	1.3514	1.3411
Experimental iso-octane	2.1334	2.1167	2.1167

conditions was measured. It should be noted that this is not the same criterion as used for the experimental data correlation (see Equation 4.38), but it is more intuitive to see the effect on the error, since the lack of logarithms will give units of cm s^{-1}.

The results are given in Table 4.1. They show that for the experimental methane data, the cubic equation actually fitted better than a quartic or quintic. This is probably because having fewer free variables allowed the minimisation code to get closer to a solution within the bounds of the defined termination parameters. However, it does make clear that there is little fourth order behaviour. Analysis of the modelling results should be treated with caution due to the small number of data points being used, but similarly to the experimental data they show very little difference between the different functions. It was decided to keep the quartic function, but with the view that it could be reduced to a cubic if necessary to reduce the number of coefficients.

4.7.2.3 Temperature and Pressure

For stoichiometric data, the nine term correlation collapses to:

$$S_{\mathrm{u}} = S_{\mathrm{u},0} T^{\eta_0} p^{\beta_0} \tag{4.28}$$

Taking logarithms of both sides allows evaluation of η_0:

$$\log S_{\mathrm{u}} = \log \left(S_{\mathrm{u},0} p^{\beta_0} \right) + \eta_0 \log T \tag{4.29}$$

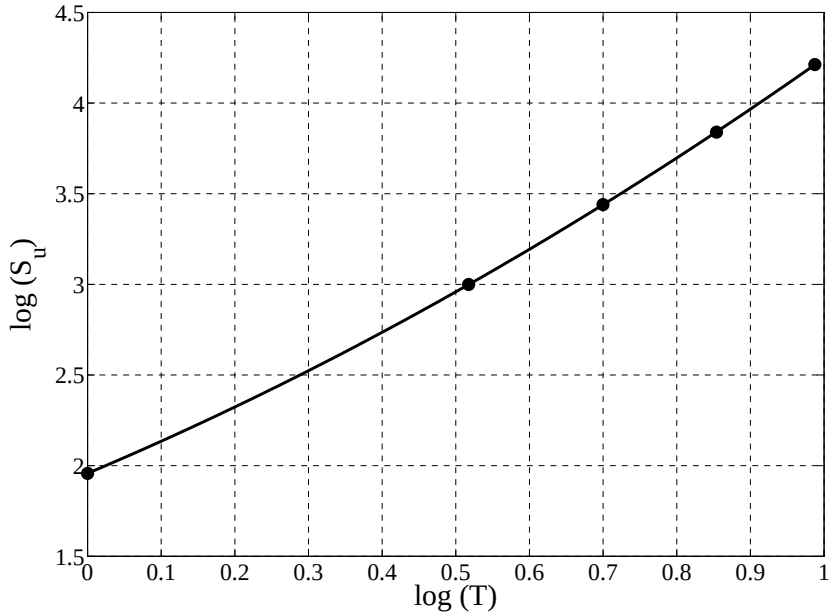

Figure 4.17: Log plot of burning velocity against temperature for stoichiometric modelling data at 20 bar and 298 K, with parabolic least-squares fit.

Taking the stoichiometric modelling data at 20 bar, a plot of $\log S_{\mathrm{u}}$ against $\log T$ produces a slight curve, which can be fitted by a parabola (see Figure 4.17). The first differential of this quadratic with respect to $\log T$ will provide the gradient of the curve, which is equal to η_0. As the second order term of the quadratic is non-zero, η_0 is clearly not a constant with respect to $\log T$. Hence it appears that the temperature exponent changes linearly with temperature. Thus it was decided to try replacing the constant η_0 with a linear function in temperature $\eta_{0\mathrm{a}} + \eta_{0\mathrm{b}} T$.

A similar argument can be applied to pressure and β_0. Again it was found that a quadratic fitted the graphs of $\log S_{\mathrm{u}}$ against $\log p$ very well. Thus β_0 was also replaced by a linear function of pressure.

Analysis of the β_1 term is greatly complicated by the re-introduction of variable equivalence ratio. This makes a similar analysis using logarithms impossible as too many variables are changing. It was decided not to pursue this, especially as adding even more terms would contribute to an increasing number of free variables in the correlation, increasing the computational complexity. Analysis of the η_1 term was impossible, as there was no modelling data available where both the temperature and

Table 4.2: Comparison of mean error (cm s^{-1}) between modelling/experimental data and the correlation fit to the data for different exponents of temperature and pressure.

Data Set	Expanded η	Expanded β	Both	Neither
Modelling fixed temp	-	1.5332	1.5332	1.3974
Modelling all	1.6608	2.1367	1.6324	2.0923
Experimental methane	1.3517	1.3532	1.3516	1.3530
Experimental iso-octane	2.0519	2.1112	2.0483	2.1172

equivalence ratio changed. Hence the updated versions of η and β to be tested were:

$$\eta = \eta_{0a} + \eta_{0b} T + (\phi - 1)\,\eta_1 \tag{4.30}$$

$$\beta = \beta_{0a} + \beta_{0b} p + (\phi - 1)\,\beta_1 \tag{4.31}$$

The same four data sets from Section 4.7.2.2 were tested. Table 4.2 shows that the extra terms improved the experimental data only very slightly. This reflects the fact that the parabola in Figure 4.17 is very shallow, so not far off being a straight line. Hence it was decided to use the original η and β terms, especially as extra terms will need to be added for residuals.

4.7.2.4 Residuals

Clarke (1994) found that the reduction in burning velocity due to residuals varied with equivalence ratio as well as residual molar fraction and hence he expanded the term used by Metghalchi and Keck (1982), since they only tested stoichiometric conditions. He analysed three additional terms to account for the residuals fraction. Of these, the following was considered most suitable:

$$S_u = S_{u,x_r=0}\left(1 - \mu_1 x_r^{\left(\mu_2 + (\phi-1)\mu_3\right)}\right) \tag{4.32}$$

4.7.2.5 Stretch Rate

As explained in Section 2.7.5, for burning velocity data found from analysis of schlieren images of the pre-pressure period flame, a plot of burning velocity against stretch rate

can be made and the burning velocity extrapolated back to the zero stretch condition in order to find a stretch-free burning velocity. This is possible because in the pre-pressure period temperature and pressure do not increase significantly. However, for the burning velocity data from the pressure record, this is certainly not true: pressure and temperature certainly increase. Hence a simple extrapolation cannot be made.

Some authors have commented that for a pressure increase to occur (such that the pressure record can be used), then the flame has to be large enough that the stretch rate will have decreased to a level such that it can be neglected (see, for example, Rahim et al. (2002), who found that for methane-air and methane-argon-oxygen flames, $L_b \approx 10^{-14}$ cm s^{-1} and so stretch rate had almost no effect). This approach was also adopted by Farrell et al. (2004). However, many other authors think that stretch rate is very important, and is the main reason for the large discrepancies between data in the literature (see, for example, Bradley et al., 1996).

For the pressure record data, two methods of correcting for the effects of stretch were investigated.

4.7.2.5.1 Extrapolation of Normalised Data As stated above, simple extrapolation cannot be carried out for pressure record data, since pressure and temperature will both be increasing. However, if the data were normalised for the effects of temperature and pressure, then virtual pre-pressure data could be generated. This could then be extrapolated.

The stoichiometric version of the correlation without residuals has the form:

$$S_u = S_{u,0} T^{\eta_0} p^{\beta_0}$$

If a fitting is done with this equation to determine values of η_0 and β_0, then the data can be normalised back to 1 bar, 298 K:

$$S_{u,0} = \frac{S_u}{T^{\eta_0} p^{\beta_0}} \tag{4.33}$$

The $S_{u,0}$ data can then be plotted against stretch rate and extrapolated back to zero stretch.

Alternatively, a stretch term can be added to the simplified correlation, so that the burning velocity data is also normalised for the effects of stretch. Following the concept of linear stretch extrapolation, this would be:

$$S_u = S_{u,0} T^{\eta_0} p^{\beta_0} (1 - L\alpha) \tag{4.34}$$

$$S_{u,0} = \frac{S_u}{T^{\eta_0} p^{\beta_0} (1 - L\alpha)} \tag{4.35}$$

where L is the Markstein length. If this data is now plotted against stretch rate (see Figure 4.18), a horizontal line should fit it, since neither temperature, pressure nor stretch rate is changing, so the burning velocity remains constant. This has the advantage that no extrapolation is required—only the y co-ordinate of the horizontal line. Therefore the two linear fit lines should have the same y-intercept. Unfortunately this does not quite occur (see Figure 4.18). In fact the difference is approximately 2 cm s^{-1}. However, the best fit line to the stretch-corrected data is very close to horizontal.

The main problem with this method is that it only works for a particular equivalence ratio. It could be repeated for different equivalence ratios, but this would lead to a piece-wise regression analysis. With the current form of the correlation it is not possible to normalise for many different equivalence ratios.

4.7.2.5.2 Stretch Term in the Correlation An alternative method to incorporate the effect of stretch would be to include a stretch term in the main correlation which would work for all data. This has the advantage that no extrapolation is required, eliminating the problems of deciding between a linear and non-linear scheme as well as choosing a data range to extrapolate from. No normalisation is required since the correlation already includes terms to take account of changing pressure and temperature. However, adding more terms has the problem of complicating the correlation,

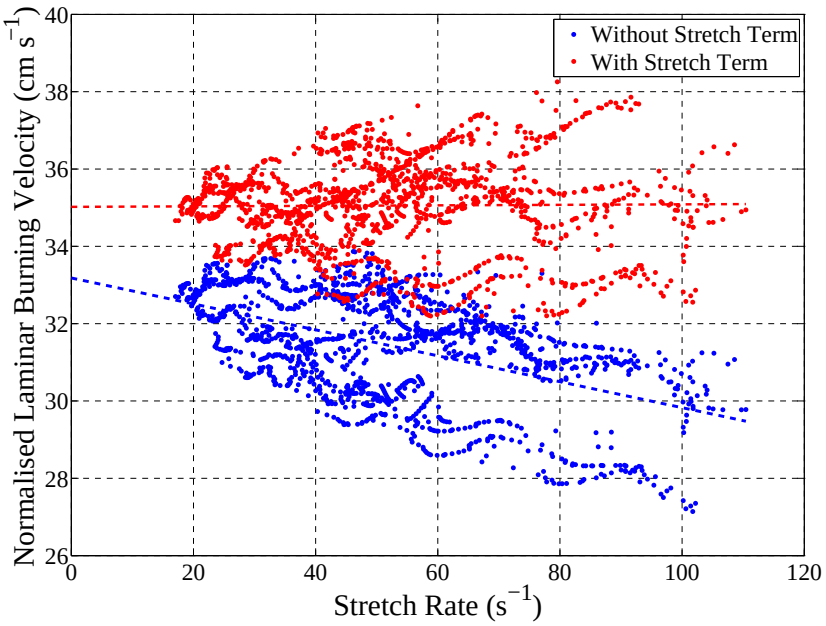

Figure 4.18: Data from twelve stoichiometric iso-octane experiments, normalised to 1 bar, 298 K. The red data has also been normalised by a linear stretch term. Linear fits are made through each of the data sets.

Table 4.3: Comparison of mean error (cm s^{-1}) between experimental iso-octane data and the correlation fit to the data with and without a linear stretch function.

Data Set	Normal	With Stretch Term	L (cm)
Experimental iso-octane stoichiometric	2.1391	1.5951	0.0017
Experimental iso-octane all	2.1172	2.1066	0.00033

which already contains a large number of free variables.

The stretch term added could be the same as that used in Section 4.7.2.5.1, namely a linear Markstein length. This would then extend the full correlation to thirteen coefficients:

$$S_{\mathrm{u}} = \left[S_{\mathrm{u},0} + S_{\mathrm{u},1}(\phi-1) + S_{\mathrm{u},2}(\phi-1)^2 + S_{\mathrm{u},3}(\phi-1)^3 + S_{\mathrm{u},4}(\phi-1)^4\right] \times T^{(\eta_0+(\phi-1)\eta_1)} p^{(\beta_0+(\phi-1)\beta_1)} \left(1-\mu_1 x_{\mathrm{r}}^{(\mu_2+(\phi-1)\mu_3)}\right)(1-L\alpha) \quad (4.36)$$

The methane modelling data was for a flat flame, so was stretch free. Hence it could not be used for analysing the impact of adding a stretch term. Experimental iso-octane data was used instead. The whole data set was tested, as well as just the stoichiometric data.

Table 4.3 shows that for the stoichiometric iso-octane data, there was a significant reduction in the mean error by adding the stretch term. However, the reduction for the whole data set was small. This result leads to the main problem with this method: a linear stretch term assumes that the Markstein length is constant, when in reality it will certainly be a function of equivalence ratio and pressure, and possibly also temperature (see Section 2.7.6). The dependence on equivalence ratio in particular is a problem, as rich and lean mixtures will tend to show opposite trends. This would explain why the resultant Markstein lengths are so small. The fitting picks a central value of a spread of data. This clearly does not apply to the stoichiometric data, although there may still be effects of temperature and pressure.

It was decided not to employ a universal stretch term in the correlation, but that a stoichiometric normalisation extrapolation as in Figure 4.18 could yield useful information about the difference in stretch behaviour between fuels.

4.7.2.6 Final Correlation

The final correlation that has been used in the current work, creating a twelve term expression for burning velocity, is:

$$S_{\mathrm{u}} = \left[S_{\mathrm{u},0} + S_{\mathrm{u},1}\left(\phi-1\right) + S_{\mathrm{u},2}\left(\phi-1\right)^2 + S_{\mathrm{u},3}\left(\phi-1\right)^3 + S_{\mathrm{u},4}\left(\phi-1\right)^4\right] \times T^{\left(\eta_0+(\phi-1)\eta_1\right)} p^{\left(\beta_0+(\phi-1)\beta_1\right)} \left(1-\mu_1 x_{\mathrm{r}}^{\left(\mu_2+(\phi-1)\mu_3\right)}\right) \tag{4.37}$$

For stoichiometric mixtures with no residuals, this collapses to Equation (4.28):

$$S_{\mathrm{u}} = S_{\mathrm{u},0} T^{\eta_0} p^{\beta_0}$$

4.7.3 Minimisation Method

For each batch, the program *fitcorr* aims to fit the twelve terms to the large data matrix generated by the *burnvel* program. These coefficients can then be used to plot graphs for conditions of interest. This method has the advantages that the condition

of interest does not necessarily need to be one that was actually tested (as long as it is within the range of conditions tested) and also these graphs can be plotted using just the twelve coefficients, so the large data matrix is no longer required.

To do this, an objective function *S_u_error* was created which calculates the sum of the squares of the differences between the natural logarithms of the burning velocity calculated for each experiment and that given by the correlation, given values of the coefficients:

$$f = \sum \left(\log S_{\mathrm{u,corr}} - \log S_{\mathrm{u,exp}} \right)^2 \tag{4.38}$$

The logarithm terms are included to make the equation closer to being linear, and so that the square of the percentage errors are minimised.

The MATLAB function *fminunc* was then used to perform an unconstrained non-linear minimisation on this problem, given initial values for the constants listed. Hence it seeks to minimise the error i.e. fit the correlation to the experimental data. It produces updated values for the constants as its output.

Fitting a four dimensional surface to a data set is computationally difficult, as the complexity approximately increases exponentially with the number of free variables. To aid the speed of convergence, the minimisation is performed in four stages, with the coefficients produced by each being used as the initial values for the next stage. The four stages are:

1. Only the stoichiometric data with no residuals is used, as this means that $\phi - 1 = 0$, hence the twelve term problem is reduced to the three term problem of Equation (4.28). The initial values of the coefficients are set to values found from previous runs, as most fuels will show behaviour of the same order.

2. One in every ten data points from the data set of experiments without residuals is used and then the nine coefficient minimisation is performed using the three variables from (1) and the other coefficients are set to values found from previous runs.

3. The nine coefficient minimisation is performed on the full data set of experiments without residuals, using the initial conditions from (2).

4. Any experiments with residuals are used to find the remaining three coefficients: μ_1, μ_2 and μ_3.

To further help convergence, for each function to be minimised, the gradient vector and Hessian matrix of the objective function are provided. The gradient vector is a vector of partial differentials. This tells the minimisation code the gradient $\mathbf{g}$ of the surface in each dimension at the point of interest, helping it to work out which direction it should move in order to make its next guess. The Hessian $\mathbf{H}$ is the matrix of second partial differentials. So for a simple function of three variables:

$$f = f(x, y, z) \tag{4.39}$$

$$\mathbf{g} = \begin{bmatrix} \frac{\partial f}{\partial x} \\ \frac{\partial f}{\partial y} \\ \frac{\partial f}{\partial z} \end{bmatrix} \tag{4.40}$$

$$\mathbf{H} = \begin{bmatrix} \frac{\partial^2 f}{\partial x^2} & \frac{\partial^2 f}{\partial x \partial y} & \frac{\partial^2 f}{\partial x \partial z} \\ \frac{\partial^2 f}{\partial z \partial x} & \frac{\partial^2 f}{\partial y^2} & \frac{\partial^2 f}{\partial y \partial z} \\ \frac{\partial^2 f}{\partial z \partial x} & \frac{\partial^2 f}{\partial z \partial y} & \frac{\partial^2 f}{\partial z^2} \end{bmatrix} \tag{4.41}$$

Clearly, to find the Hessian of an expression as complex as Equation (4.37) would require a large amount of tedious differentiation. This was simplified by using the Symbolic Math toolbox in MATLAB, which allows the user to generate a symbolic equation. The *jacobian* function finds the gradient vector, and the Jacobian of that is the Hessian matrix. The result can be simplified to reduce the length of the expressions.

Once the twelve coefficients have been found, fitcorr shows the user a plot of burning velocity against pressure for each experiment (see Figure 4.19). This contains the experimental data as well as the burning velocity calculated from the correlation for the same conditions (i.e. same pressure, temperature, equivalence ratio and residual frac-

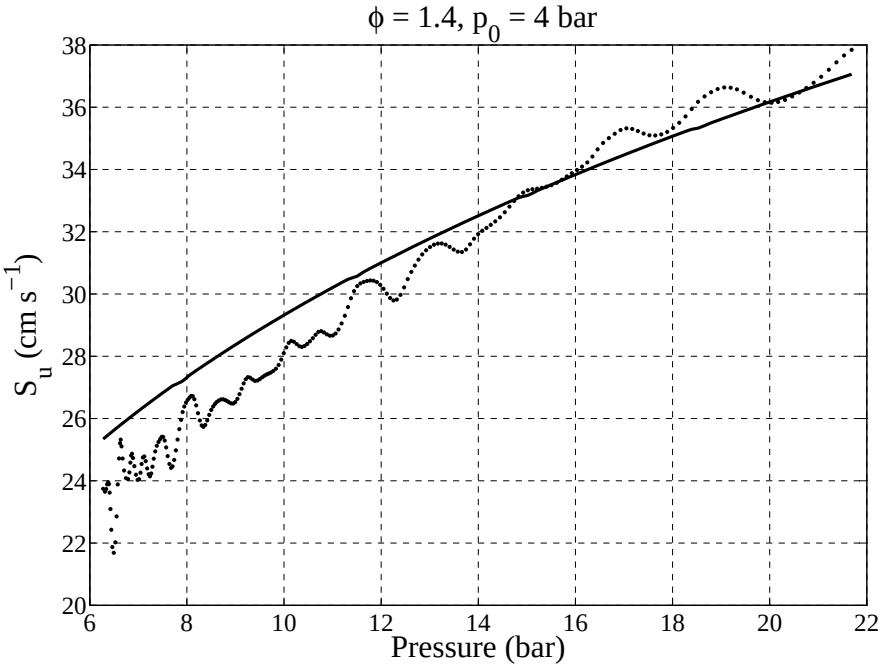

Figure 4.19: Burning velocity for a single experiment shown as points with the correlation from many experiments for the same conditions shown as a line. An important point is that the line is not fitting the experimental data from just this experiment, but from every experiment in the batch.

tion). This clearly shows the user how well the correlation has fitted the experimental data.

4.8 Data Plotting

4.8.1 Onset of Cellularity

If *bvimage* has already been run for the current batch, then the time of onset of any cellularity will be known. If *burnvel* has subsequently been run, then the other conditions relating to that time will also be known. All can be plotted by the program *plot_cell* against one or two variables from initial pressure, initial temperature, equivalence ratio and residuals mole fraction. Fixed values of up to three of the same variables can be chosen. For an example see Figure 4.20.

For plots of two variables, there is a choice of multiple 2D lines, 3D points or a 3D surface. Titles, axes labels and legends are generated automatically. For multiple

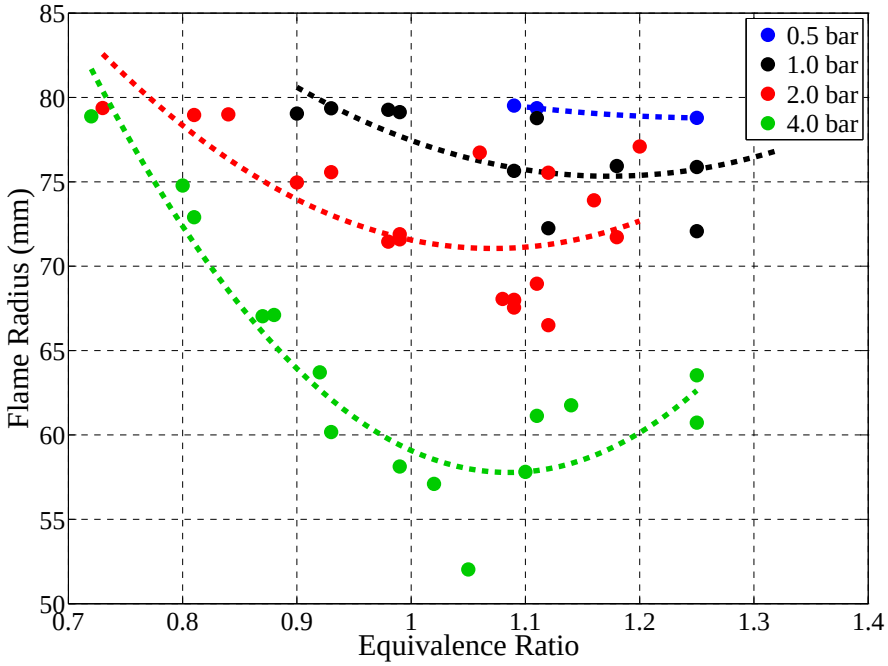

Figure 4.20: Example plot showing flame radius at onset of cellularity against equivalence ratio for different initial pressures, a fixed initial temperature and no residuals, with parabolic least squares fit to help show trends.

2D lines there is the option of fitting a parabola to the data to help show trends. This system allows for a very quick investigation of how the initial conditions affect cellularity.

4.8.2 Burning Velocity Data

The program *plot_data* plots burning velocity data points determined from either pressure data or schlieren images. 2D or 3D plots can be generated from the following variables:

1. Burning velocity
2. Stretch Rate
3. Temperature
4. Pressure
5. Flame Radius

6. Time
7. Equivalence ratio
8. Initial temperature
9. Initial pressure
10. Residual mole fraction

Data can be filtered by the four initial conditions. The number of data points included is displayed.

4.8.3 Burning Velocity Correlation

Once the fitcorr program has been run on a data set, coefficients for the correlation can be used to plot the correlation over any range of up to two initial conditions. There is a the choice of a single 2D line, multiple 2D lines or a 3D surface (see Figure 4.21). For the variables that are not being plotted, fixed values can be entered. For multiple 2D lines, a step size is required to determine the change in the plotting variable between lines, as well as start and end values. This tool is very useful to see trends in burning velocity with smooth curves due to the use of the correlation, however users should be careful that the conditions plotted are ones for which there is data, otherwise the results will be an extrapolation, which can lead to errors.

4.9 Conclusions

Image processing code was developed in MATLAB to produce radius data and cellularity detection data from the schlieren images. However, this could not reliably be used to find burning velocities, as the small windows meant that the data had stretch rates large enough to prevent robust extrapolation to zero stretch. Further MATLAB code was written to calculate burning velocities, using the experimental pressure traces in conjunction with the output of an existing multi-zone numerical combustion model.

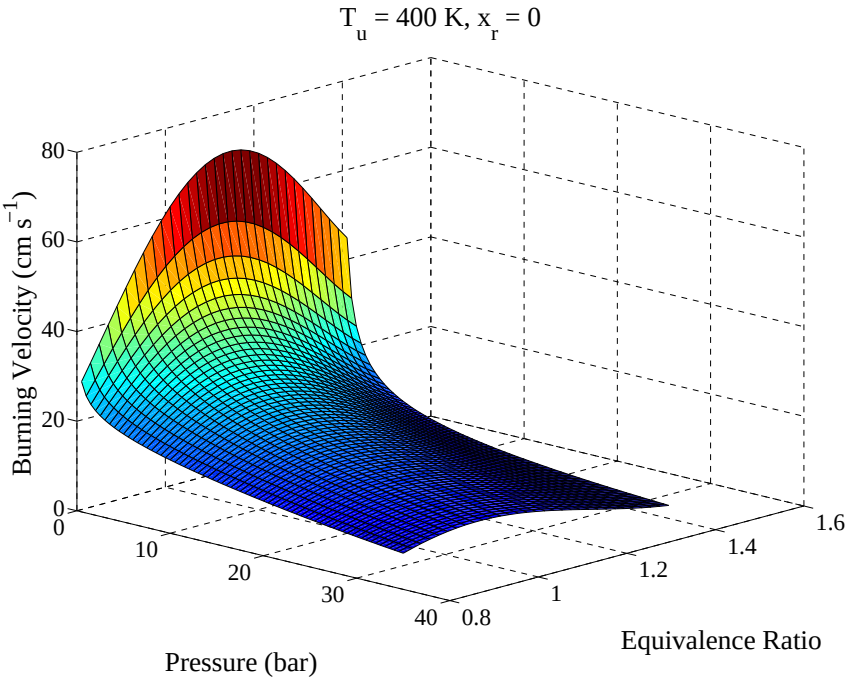

Figure 4.21: Example surface plotted from the correlation.

A twelve term correlation in terms of pressure, temperature, equivalence ratio and residual mole fraction was validated by reference to methane modelling data and experimental data for methane and iso-octane. It was shown how this correlation could be used to normalise stoichiometric, non-residuals, pressure-derived data back to standard conditions, so that pressure and temperature were constant. This would then allow extrapolation to zero stretch.

An integrated graphical user interface was constructed to allow running of the BOMB program, calculating burning velocities from both schlieren and pressure data, fitting to find coefficients for the correlation, and plotting of all the available data.

Chapter 5

Data Validation

5.1 Mixture Preparation

5.1.1 Mixing Loop

The fact that the mixing loop was open for only part of the filling process meant that it had a richer equivalence ratio than the rest of the bomb, as it was closed when the second tranche of air was added. A spreadsheet was set up to see how this would affect the equivalence ratio of successive experiments, using the volumes calculated in Section 3.3.5. It was assumed that the whole apparatus started off containing only air and that all the experiments had the same target equivalence ratio and mixture pressure, hence the same partial pressure of fuel to be added.

Figure 5.1a shows that the equivalence ratio starts off lean, as the mixing loop initially contains air, but the LabView program assumes that there is mixture left over from the previous experiment. The logarithm of the error between the intended equivalence ratio and that which will occur is seen to fall approximately linearly (see Figure 5.1b).

To avoid the potential 2% error that could result from the first experiment, where there was no knowledge of the composition of the mixing loop each set of experiments was preceeded by a dummy experiment. For experiments where there were no residuals

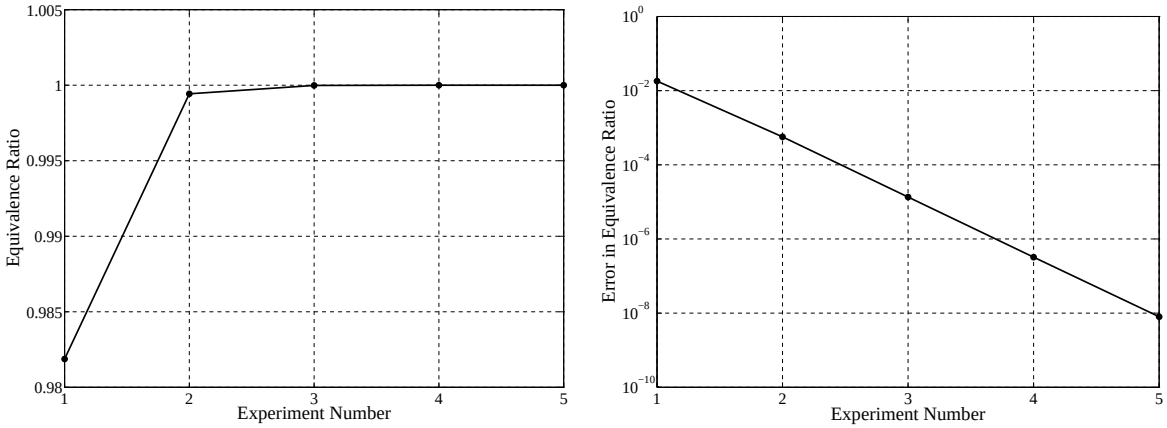

(a) Equivalence ratio (b) Error in equivalence ratio (log scale)

Figure 5.1: The (a) equivalence ratio and (b) error in subsequent experiments due to the mixing loop.

used, a dummy experiment was deemed unnecessary if the equivalence ratio had only being changed by 0.1. Dummy experiments were generally found to be leaner by a λ value of around 0.02.

5.1.2 Equivalence Ratio Problems

It was found that with liquid fuels, experiments at the same conditions had good repeatability (see Section 5.6), but the equivalence ratios of the products, as measured by the lambda sensor, did not always match what was anticipated. The mixtures were generally richer than required. The equivalence ratio seemed to change with initial temperature and injection pressure. Furthermore, the effects were different for different fuels. The focus of the investigation into these problems was the syringe injection method. Many tests were performed to try and characterise the error.

5.1.2.1 Injection Pressure

The fuel has to be injected around atmospheric pressure so that the low pressure pump can operate. The pressure normally used was 0.8 barA. Using a pressure slightly below atmospheric pressure meant that if there was a leak, air would leak in rather than fuel/air mixture leaking out. This analysis agrees with Figure 5.2, which shows that

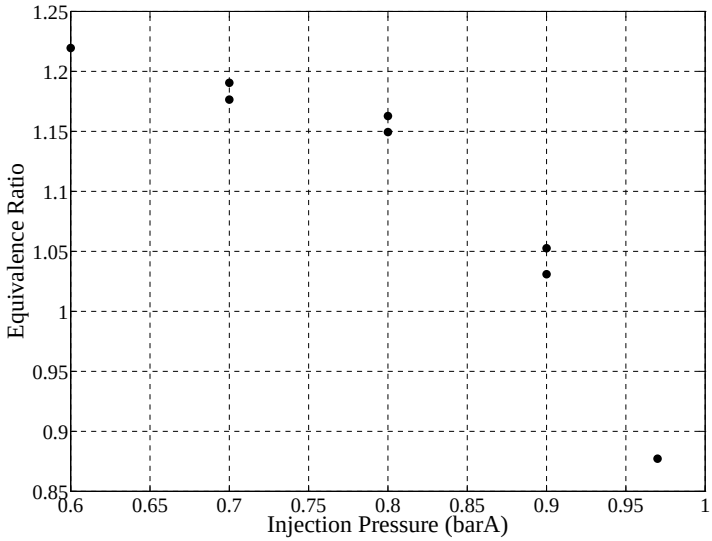

Figure 5.2: Measured equivalence ratio for a nominally stoichiometric experiment with different injection pressures (iso-octane, $T_0 = 380$ K, $p_0 = 2$ bar).

high injection pressures led to weak mixtures, even though all the pressures tested were below atmospheric.

5.1.2.2 Weighing The Syringe

Tests were conducted using toluene with different nominal equivalence ratios, weighing the syringe before and after injection to compare the lambda measurements of the combustion products with the mass of fuel injected. The injection pressure was kept constant at 0.8 barA. The volume of fuel was kept the same, and the equivalence ratio varied by varying the number of moles of air subsequently added. This ensured that the injection conditions remained the same throughout. An equivalence ratio was also calculated from the mass of fuel injected.

Figure 5.3 shows that rich experiments were richer than the intended equivalence ratio. This is also where the largest errors were seen. There was no clear trend for lean experiments. The mass of fuel injected varied between 313.6 and 325.7 mg. There was no clear relationship between this and nominal equivalence ratio.

Better agreement is seen when the equivalence ratio measured by the lambda sensor is replaced by that calculated from the mass of fuel injected (see Figure 5.4). This shows that for constant injection conditions, the injection process is consistent. The

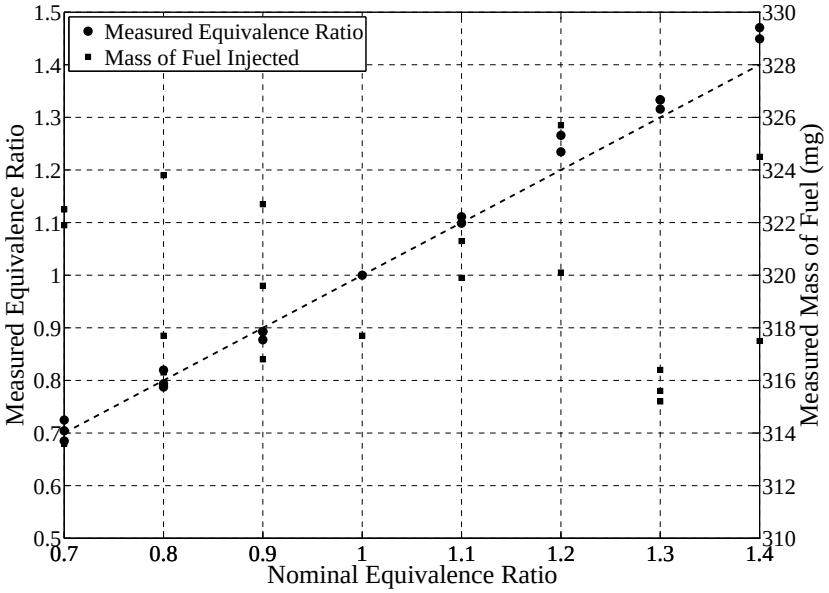

Figure 5.3: Nominal equivalence ratio against measured equivalence ratio from lambda sensor and mass of fuel injected.

problems are that it varies with the temperature, volume of fuel injected and the injection pressure. The differences are more pronounced for more volatile fuels e.g. iso-octane and ethanol.

5.1.2.3 Syringe Volume

In addition to the problems noted above, it was found that the volume of the syringe used made a difference to the mass of fuel injected. Injecting 500 µl of fuel from a 500 µl syringe gave an 8% increase in mass injected over that measured when a 1000 µl syringe was used to inject 500 µl, from a mean of three injections for each. This led to an average difference in lambda of 0.10 between the two syringes. When the same injections were done outside of the bomb, very similar mass changes were measured.

Both syringes were placed as if to inject fuel into the hot bomb for five minutes with no injection and the change in mass was measured. The change in mass was far greater for the 500 µl syringe, both when the pump was on and when it was off. The 500 µl syringe also led to faster fuel evaporation from a pre-heated needle. A reduction in the injection duration from 5 minutes to 1 minute had no effect.

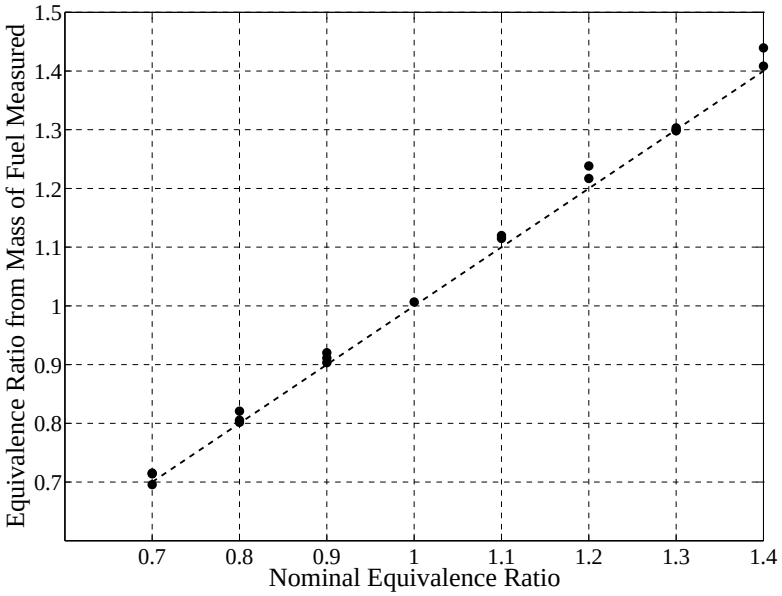

Figure 5.4: Nominal equivalence ratio against that calculated from the mass of fuel injected.

5.1.2.4 Conclusions

It was decided that the problems were due to heat from the oven conducting along the stainless steel needle and evaporating fuel in the needle. This led to a greater mass of fuel being introduced into the mixing loop than the change in syringe volume would indicate, because there was vapour in the needle. Although the needle used for the two different sizes of syringes was the same, it was thought that the smaller 500 µl syringe would be affected more, hence it produced a richer mixture than the larger syringe.

A copper heat-sink and electric fan blowing over it were tested to try and keep the syringe-end of the needle at a constant temperature. This was found to reverse the difference between the two needles i.e. the 1000 µl syringe now gave the richer mixture. Hence this was not used.

It was decided to only use the 1000 µl syringe for all experiments, as the gain in consistency would outweigh the slight decrease in accuracy for fuel volumes less than 500 µl. This still left the problem of the rich mixtures. It was decided that although a nominal equivalence ratio would still be used as a target, the lambda sensor would be used to measure the equivalence ratio of each experiment and this would be taken as the actual equivalence ratio for the results. For the 1 and 0.5 barA initial pressure

experiments, the lambda sensor could not be used as there was no pressure difference to cause a flow past the sensor. However, since these experiments use the same mixture pressure (and hence the same fuel volume) as their equivalent experiment at 2 barA, the value measured for this experiment was copied to the other two.

5.2 BOMB Program

5.2.1 Lewis and von Elbe Method

Lewis and von Elbe (1961) proposed a simple linear model for mass fraction burned (see Section 2.4.1.6.1), in which it is assumed to be equal to fractional pressure increase. Although this is less accurate than the multi-zone numerical model used by the BOMB program, it can used as a useful check. It does, however, require an end pressure and a value of gamma (ratio of specific heats) to be specified.

An experiment from the iso-octane data set was used to compare the two methods. This had an initial temperature of 450 K, initial pressure of 1 bar, an equivalence ratio of one and no residuals. The end pressure was set to the last pressure output by the BOMB program (i.e. the pressure when the mass fraction burned is equal to one). This was 6.53 bar. The gamma was set to an approximate mean value of those output by the BOMB program ($\gamma = 1.31$). The burned gas radius is calculated by Equation (2.74) and the initial shell radius by Equation (4.22).

The mass fraction burned and stretched burning velocity are plotted against pressure in Figure 5.5. As expected, the mass fraction burned given by the multi-zone numerical model varies from the linear Lewis and von Elbe analytical model in the middle section. Note that the mass fraction burned never reaches one, because the experimentally measured pressure will never reach the modelled end pressure due to conduction to the walls of the bomb in the latter stages of combustion. Other than the very early stages, the calculated burning velocities are remarkably similar. This shows that the burnvel program, the BOMB program and the thermodynamic data inputs

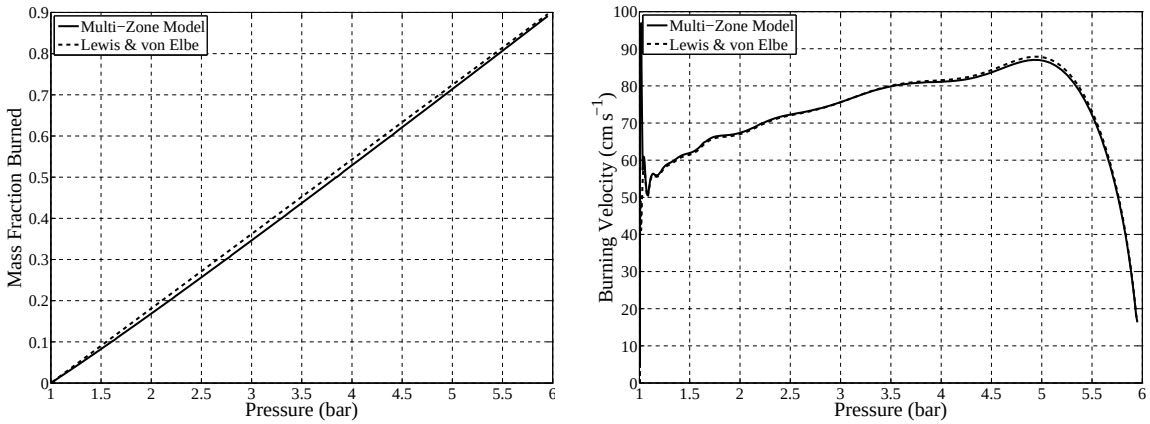

(a) Mass Fraction Burned

(b) Stretched Burning Velocity

Figure 5.5: The (a) mass fraction burned and (b) burning velocity calculated using both the BOMB program and the linear model of Lewis and von Elbe (1961) for an iso-octane experiment ($T_0 = 450$ K, $p_0 = 1$ bar, $\phi = 1$, $x_\mathrm{r} = 0$).

are working correctly.

5.2.2 Comparison with Other Models

Combustion of stoichiometric methane burning in air, at an initial temperature of 298 K and an initial pressure of 1 bar, is used as a standard case in the literature for examining the output of various computer models of combustion.

The BOMB program was run under these conditions with 1, 2, 10, 20 and 100 zones. For each of these, the first and last zones were compared with the equilibrium solvers *STANJAN* (Reynolds, 1986) and *Gaseq* (Morley, 2005).

Gaseq has the methane-air system built-in. It calculates the mole fraction of ten product species (N_2, H_2O, CO_2, CO, O_2, OH, H, O, H_2 and NO).

5.2.2.1 Single Zone

The BOMB program can also be run with a single zone. It then becomes a simple equilibrium program, allowing direct comparison to STANJAN and Gaseq. The results show excellent agreement (see Table 5.1).

Table 5.1: Comparison of end temperatures and pressures for single zone combustion of stoichiometric methane in air at $T_0 = 298$ K and $p_0 = 1$ bar.

Model	p_e (bar)	T_e (K)
BOMB single zone	8.799	2587
STANJAN	8.808	2587
Gaseq	8.805	2587

Table 5.2: Comparison of temperatures of first and last burning zones for different numbers of zones and different equilibrium solvers, for stoichiometric methane in air at 298 K, 1 bar. Temperature subscripts refer to the points shown in Figure 2.8. Note $\Delta T = T_3 - T_5$.

Model	Zones	T_2 (K)	T_3 (K)	T_4 (K)	T_5 (K)	ΔT (K)	p_{end} (bar)
STANJAN	-	2225	2934	537	2399	535	-
Gaseq	-	2225	2934	537	2398	536	-
BOMB	2	2223	2694	537	2463	231	8.777
	10	2223	2850	534	2406	444	8.753
	20	2223	2880	532	2399	481	8.745
	100	2223	2889	522	2389	500	8.700
Luijten and de Goey (2007)	20	2159	3086	532	2232	854	-

5.2.2.2 Multiple Zones

As is explained in Section 2.4.1.6.3, the burning of the first zone in a multi-zone combustion model is equivalent to burning at constant pressure and enthalpy followed by isentropic compression (see route $1 \rightarrow 2 \rightarrow 3$ in Figure 2.8). The last zone is compressed isentropically from the initial conditions to the end pressure and then burns at constant pressure and enthalpy (route $1 \rightarrow 4 \rightarrow 5$). These two separate routes can be explored by the equilibrium solvers, although they require an end pressure to be set. This was set to be 8.753 bar, corresponding to that returned by the BOMB program using ten zones.

The BOMB program was also compared against the analytical twenty zone model of Luijten and de Goey (2007), which is described in Section 2.4.1.6.4. Henceforth, this model shall be referred to as the Eindhoven model.

This model has been validated against their own two zone numerical model, but the BOMB program's multi-zone model has been validated against STANJAN and Gaseq.

As is shown in Table 5.2, this comparison showed good agreement for the temperatures at every stage when run with 100 zones. In this case the BOMB program showed a burned gas temperature difference of 500 K, as STANJAN gave 534 K when used in conjunction with the end pressure given by the BOMB program. By comparison, the temperature difference in the graph published by Luijten and de Goey (2007) is approximately 810 K.

The reason for the large disagreement between the Oxford and Eindhoven models with respect to the burned gas temperature difference is due to four main reasons. The first is that, as already stated, the Eindhoven model uses constant gas properties, meaning that the value of gamma used in the isentropic compression of zone one is overestimated. Figure 5.6 shows that for the twentieth zone, there is good agreement along the line of isentropic compression, because the temperature is less than 550 K and hence the change in heat capacity is small. However, the major disagreement comes with the isentropic compression of the first zone after burning, when the temperatures are much higher, and hence the values of gamma will be different between the two models.

The other reasons for the discrepancy are, briefly, that the Eindhoven model completely ignores the dissociation of the burned gas (this will tend to change the specific heat capacity even more, leading to further error), complete combustion is assumed, and the end pressure must still be deduced. These problems are described in full in Section 2.4.1.6.4.

5.3 Burnvel Program

5.3.1 Artificial Pressure Trace

A program was written which, for a specified constant arbitrary burning velocity, worked backwards to create an artificial pressure trace, which could then be fed into the burning velocity programs as if it were experimental data, to provide some checks

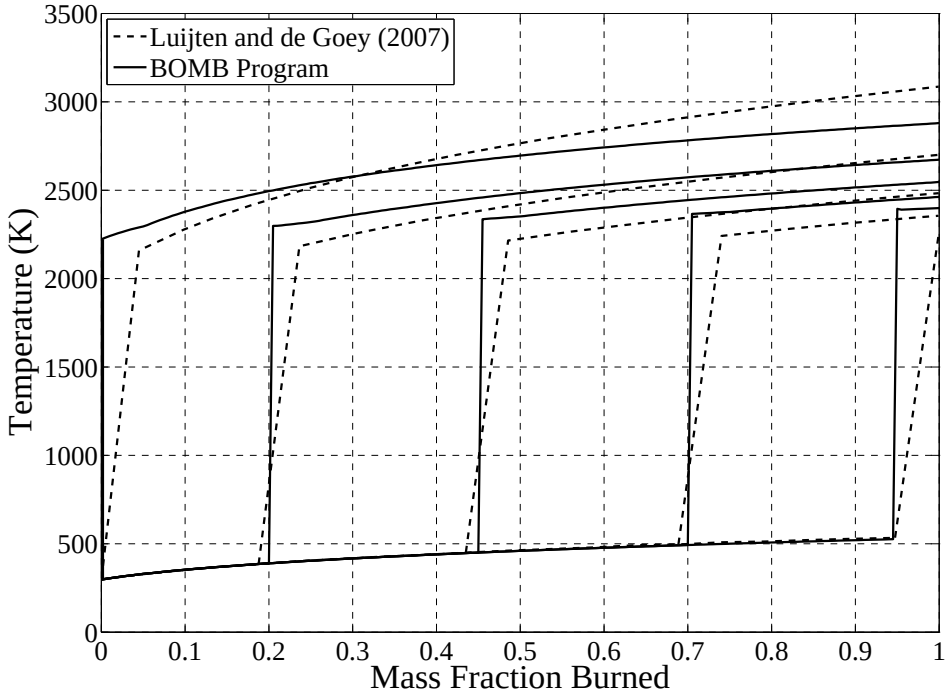

Figure 5.6: Zones 1, 5, 10, 15 and 20 of the BOMB program run with twenty zones and the same zones for the twenty zone analytical model of Luijten and de Goey (2007).

on the code. The constant originally entered should then be given as the output.

A BOMB program zone file was used to generate an approximate mean gamma ($\gamma = 1.36$), end pressure and the initial density. The latter is used to calculate the total mass:

$$m_{\mathrm{t}} = \frac{4}{3}\pi R^3 \rho_0 \tag{5.1}$$

A small initial radius is set. The initial mass of burned gas is then calculated by:

$$m_{\mathrm{b}}^0 = m_{\mathrm{t}} \left(\frac{r_{\mathrm{b}}}{R}\right)^3 \tag{5.2}$$

This program then used an incremental model of the advancing flame front in a loop,

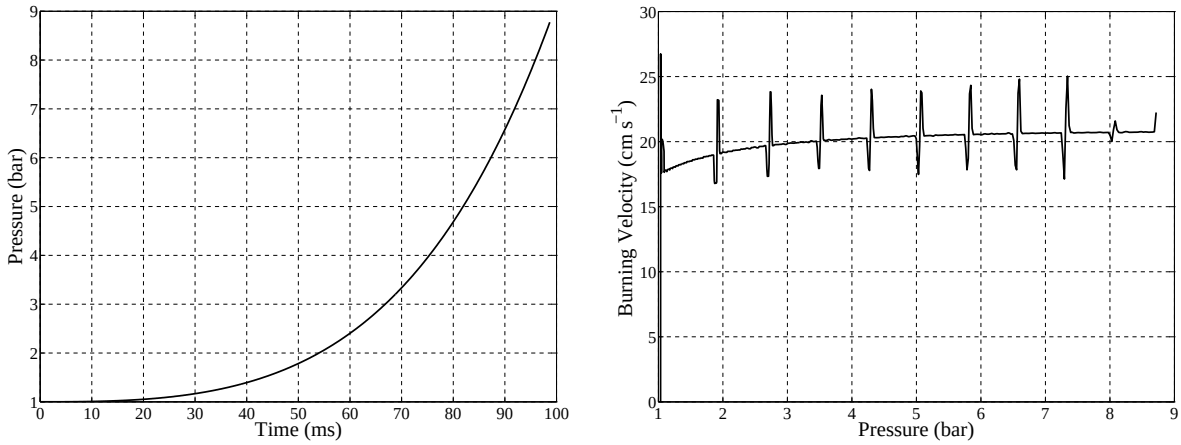

Figure 5.7: (a) Artificial pressure trace constructed using an incremental analytical flame model for constant burning velocity of 20 cm s^{-1} and (b) burning velocity calculated from this pressure trace.

using the linear analytical mass fraction burned model of Lewis and von Elbe (1961):

$$m_{\mathrm{b}_{i+1}} = m_{\mathrm{b}_i} + 4\pi r_{\mathrm{b}_i}^2 \rho_{\mathrm{u}_i} S_{\mathrm{u}}\,\mathrm{d}t \tag{5.3}$$

$$x_i = \frac{m_{\mathrm{b}_{i+1}}}{m_{\mathrm{t}}} \tag{5.4}$$

$$p_i = x_i\,(p_{\mathrm{e}} - p_0) + p_0 \tag{5.5}$$

$$\rho_{\mathrm{u}_{i+1}} = \rho_0 \left(\frac{p_i}{p_0}\right)^{\frac{1}{\gamma}} \tag{5.6}$$

$$r_{\mathrm{b}_{i+1}} = \left[R^3 - \frac{m_{\mathrm{t}}\,(1 - x_i)}{\frac{4}{3}\pi\rho_{\mathrm{u}_{i+1}}}\right]^{\frac{1}{3}} \tag{5.7}$$

This algorithm was used to generate a pressure trace for a constant burning velocity of 20 cm s^{-1} (see Figure 5.7a).

The zone file used to find the initial and end conditions was for stoichiometric methane with an initial pressure of 1 bar, initial pressure of 298 K and no residuals. The pressure trace was then fed into the burnvel program as if it were experimental data. The burning velocity output of the burnvel program is shown in Figure 5.7b. The spikes are caused by the transition between the zones. These are normally filtered (see Section 4.6.1.1). As expected, the burning velocity is not constant at 20 cm s^{-1}, because of the approximations in the linear relation of Lewis and von Elbe (1961).

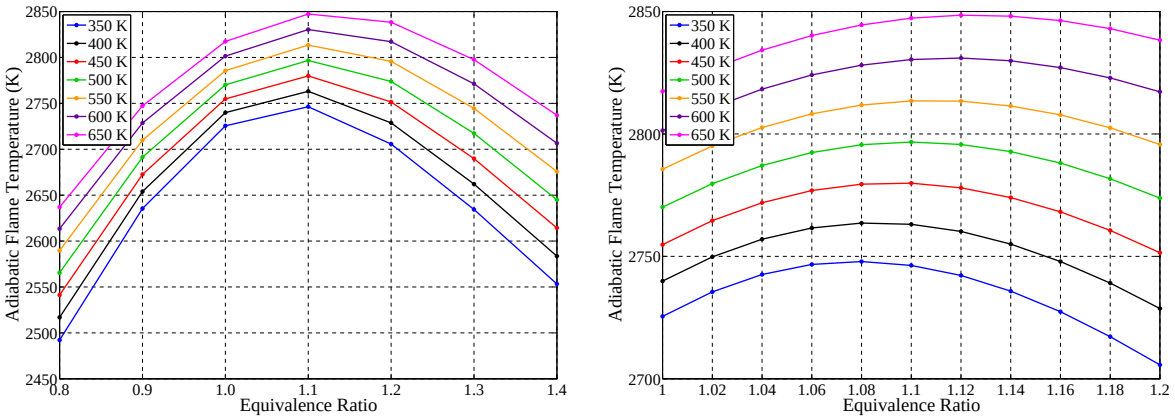

(a) Full Range (b) Peak

Figure 5.8: Adiabatic flame temperatures of iso-octane at $p_0 = 5$ bar for varying equivalence ratio and unburned temperature, showing the equivalence ratio at peak burning velocity increasing with temperature due to dissociation.

5.4 Adiabatic Flame Temperature

Since the burning velocity is dominated by temperature effects (including the temperature effects caused by varying equivalence ratios), an idea of the trends in burning velocity with equivalence ratios at different temperatures and pressure can be obtained from plotting adiabatic flame temperatures for the fuel of interest. Adiabatic flame temperatures for iso-octane/air were calculated using the equilibrium solver Gaseq (Morley, 2005).

Figure 5.8 shows adiabatic flame temperatures at an initial pressure of 5 bar. Figure 5.8b gives a more detailed view of the burning velocity maxima shown in Figure 5.8a. As temperature increases, adiabatic flame temperature increases and the peak burning velocity occurs at a higher equivalence ratio, due to increased dissociation.

Figure 5.9 shows adiabatic flame temperatures at an initial temperature of 500 K. It should be noted that the trend of increasing adiabatic flame temperature with increasing pressure is opposite to that for burning velocities. However, the important trend is that the equivalence ratio at which peak burning velocity occurs decreases (i.e. gets closer to stoichiometric) as pressure increases. This is because the higher pressure

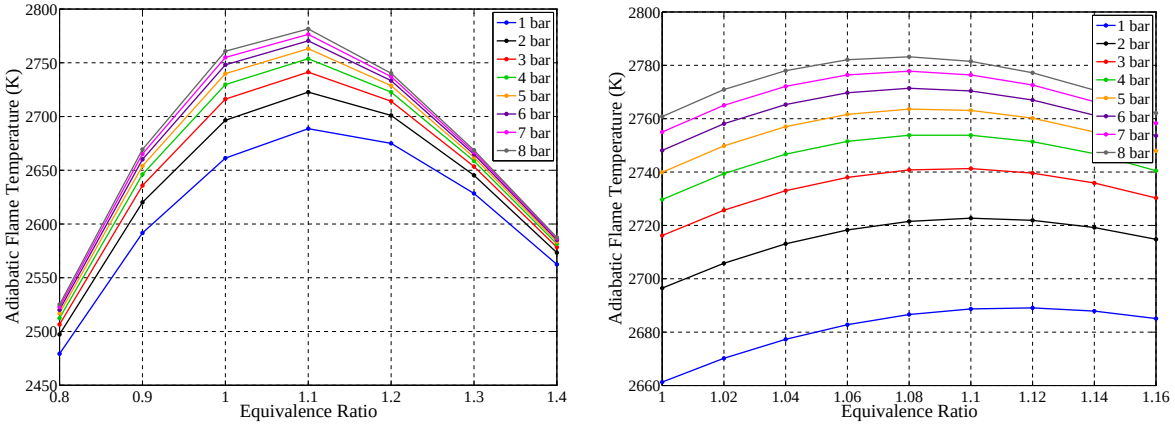

(a) Full Range (b) Peak

Figure 5.9: Adiabatic flame temperatures of iso-octane at $T_0 = 400$ K for varying equivalence ratio and unburned pressure, showing the equivalence ratio at peak burning velocity getting closer to stoichiometric for increasing pressure.

reduces dissociation.

5.5 Correlation Fitting

5.5.1 Avoiding Cellularity

The fitcorr program relies on the user to choose the data from each experiment, which is concatenated with all the other experiments into the data set, and then has the correlation fitted to it. Experience is necessary to spot the increase in burning velocity associated with the onset of cellularity. The cellularity detection algorithm helps a lot, especially for rich, high pressure experiments, where cellularity can occur very early on, well within the noisy early-burn period. This makes it very hard to spot otherwise.

To see the effect of including cellular data, burnvel was run twice with the n-butane experimental data. On one pass, the user was very selective, and used the equivalence ratio and pressure for each experiment to determine likely cellular data. On the second pass, only very clear cellular data was excluded. The correlation was fitted to both data sets and then plotted at typical conditions for the set.

As is shown in Figure 5.10, the choice of data made a large difference to the burning velocity correlation. This difference is greater in the rich data and at higher pressures

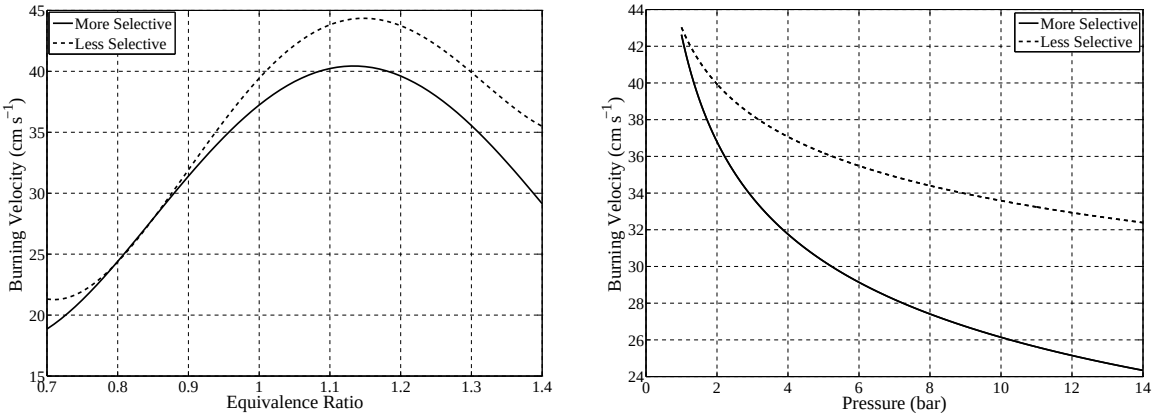

(a) Equivalence Ratio (b) Pressure

Figure 5.10: Burning velocity correlation evaluated at (a) $T_\mathrm{u} = 400$ K, $p_\mathrm{u} = 6$ bar (b) $T_\mathrm{u} = 400$ K, $\phi = 1.4$ for fits to a selective and less selective n-butane data set.

— the conditions where the flame would be expected to be cellular. Correspondingly, pressure and equivalence ratio had a large effect on the difference between the two sets. Temperature had a relatively small effect. The increased surface area of the cellular flame means that it will have a higher burning velocity than the smooth flame.

5.5.2 Biased Data

Pressure data affected by cellularity is not included in the data matrix which the correlation is fitted to. Rich experiments at higher initial pressures tend to be affected more by cellularity. Hence in the data matrix there are far fewer data points at high equivalence ratios and pressures compared to low ones. The correlation is fitted by minimising a function of the difference between the correlation and each data point (see Equation 4.38). All points are weighted equally. Hence the correlation can become biased towards lower equivalence ratios and pressures, sacrificing a good fit at conditions where data is sparse in order to give a slightly better fit where there are lots of points. An example of this will be seen later in Figure 5.13a. The following sections reflect investigation of this phenomenon.

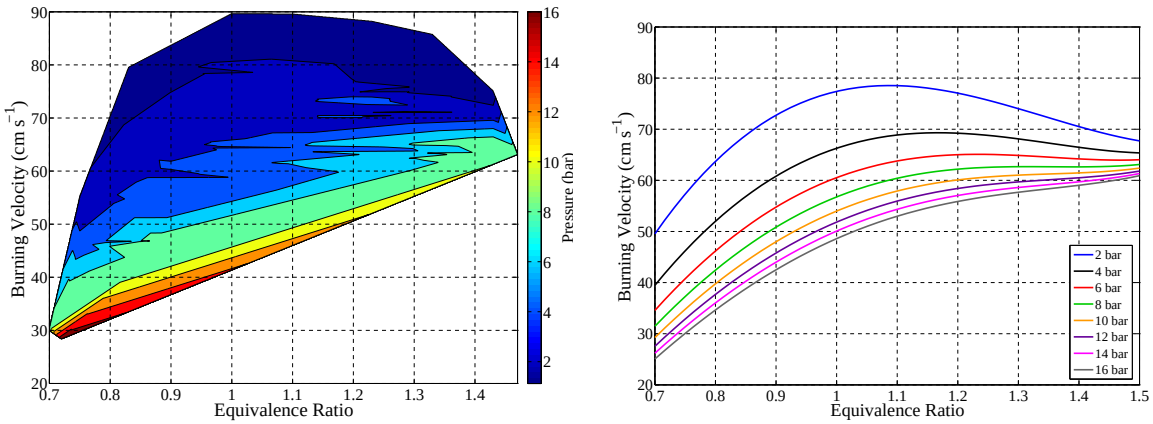

(a) Data (b) Correlation

Figure 5.11: Comparison of (a) a contour plot of iso-octane burning velocity data close to 550 K and (b) the correlation plotted at the same conditions.

5.5.3 Correlation Compared with Raw Data

Figure 5.11 shows a comparison between a contour plot of iso-octane data around a fixed temperature (550±1 K) and a plot of the correlation at the same conditions. The contour plot shows that there is no high pressure (hence low burning velocity) data for rich equivalence ratios. This could explain the shape of the correlation, with burning velocities that are too high on the rich side. The correlation is merely following the data available. Having data which filled the 'hole' would pull down the values on the rich side to form a curve peaking at $\phi \approx 1.1$.

5.5.4 Data Splitting

If a data set is split into rich and lean data, the correlation can be fitted to each set separately and plotted over the full range of equivalence ratios (see Figure 5.12). This gives a good indication of how each half wants the correlation to look like in its own half, and what its extrapolated other half will look like as a result.

The lean correlation fits the lean half well, and peaks at approximately the correct equivalence ratio, but clearly decreases too rapidly on the rich side, going negative. The rich half does not seem to fit either half well. It peaks at too high an equivalence ratio and shows very little gradient with respect to equivalence ratio.

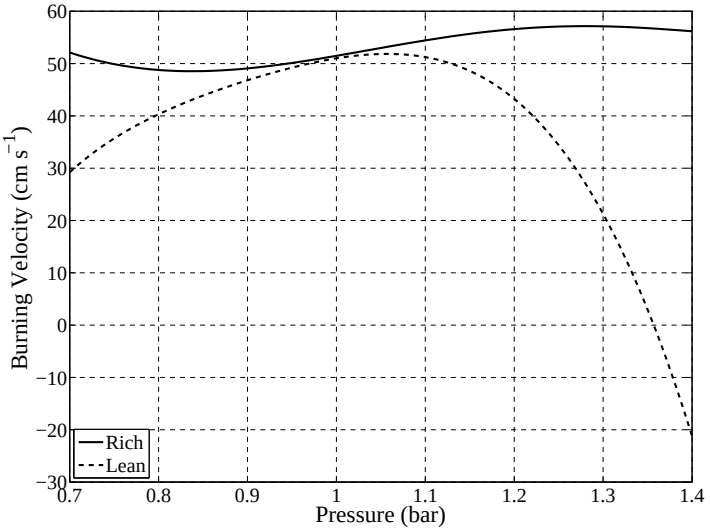

Figure 5.12: Correlations fitted to the rich and lean halves of the iso-octane data set at $T_\mathrm{u} = 500$ K, $p_\mathrm{u} = 5$ bar and $x_\mathrm{r} = 0$.

This analysis shows how radically different the behaviour of rich and lean mixtures are.

5.5.5 Piece-wise Regression

An alternative method of minimisation is to segment the data by equivalence ratio (e.g. $\phi = 0.7$–0.8, 0.8–0.9 etc.), then treat each segment as if it were a single equivalence ratio (unfortunately this will not be the exact case due to some scatter in the equivalence ratio). Then the stoichiometric correlation was fitted to each segment individually to get values of $S_{\mathrm{u},0}$, η and β. Once this was done for each segment, suitable functions can be fitted to the concatenated values of the three variables. In line with the form of the general correlation, a quartic can be fitted to the values of $S_{\mathrm{u},0}$ to give an expression for equivalence ratio. Linear functions can be fitted to η and β to give η_0, η_1, β_0 and β_1. These can then be used to construct the full correlation.

The segmented correlation was compared with the normal correlation (see Figure 5.13). Although the segmented correlation shows more change in gradient, burning velocity starts to increase at high equivalence ratios. Also, the peak burning velocity seems to increase with pressure, which is the opposite of the correct trend (see Section 5.4).

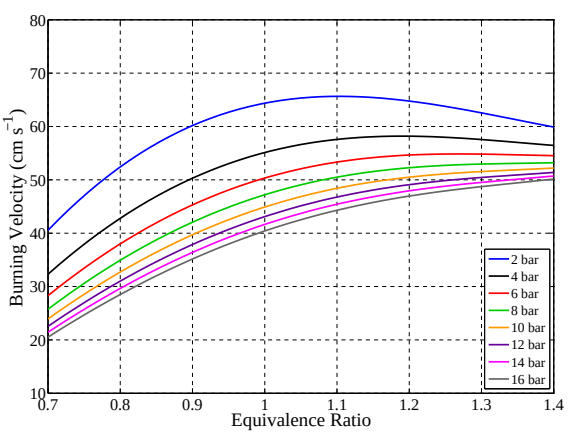

(a) Normal Correlation

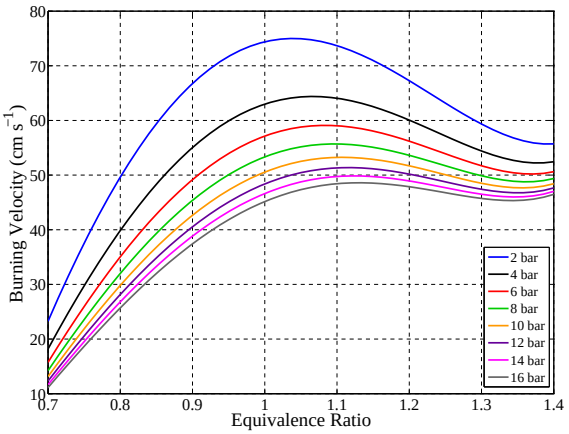

(b) Segmented Correlation

Figure 5.13: Comparison of (a) normal correlation for iso-octane at $T_{\mathrm{u}} = 500$ K, $x_{\mathrm{r}} = 0$ and (b) a segmented correlation at the same conditions.

5.5.6 Gaussian Processes

As mentioned in Section 5.5.2, the problem with the correlation fitting is that all points are equally weighted, so the correlation is liable to be skewed. This fitting is an instance of a prediction problem. Given the experimental observations of burning velocity (which will contain a certain level of associated noise) at various pressures, temperatures etc., one wishes to be able to predict the burning velocity at any arbitrary conditions. One method is to apply a Gaussian process (GP) to this regression problem.

Gaussian processes (Rasmussen and Williams, 2006) are a powerful way to perform regression. They fit a multivariate Gaussian probability distribution to any set of output variables, allowing for analytic inference. As a principled Bayesian technique, GPs supply a full posterior distribution for the output variables, giving both mean estimates and an indication of their uncertainty.

MATLAB code to implement a Gaussian process was obtained from the Oxford Pattern Analysis & Machine Learning Research Group. Unfortunately, the GP was a memory-intensive algorithm, and so the burning velocity data sets had to be reduced to fewer than 450 data points. A crude downsample can be implemented by taking 1 in every n data points. A more rigorous method was to use an algorithm that chose points for deletion so that the final data set would not contain any points closer than a

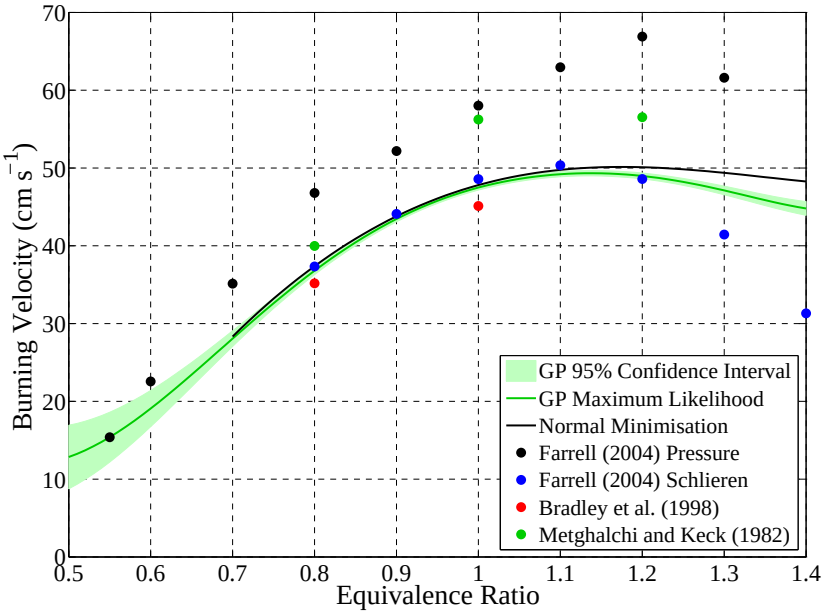

Figure 5.14: Comparison of Gaussian process maximum likelihood function, normal minimisation and literature data for iso-octane at $T_u = 450$ K, $p_u = 3$ atm, $x_r = 0$.

set Euclidean distance in the parameter space (p_u,T_u,ϕ). However, this algorithm also required more memory than was available, so a pre-filter of a 1 in 3 crude downsample was required first to reduce the data set to a manageable size.

This algorithm was tested with the iso-octane data set and predictions for different equivalence ratios were obtained at $T_u = 450$ K, $p_u = 304$ kPa to compare with literature data and the current correlation fitting method (see Figure 5.14). The data set used was a crude downsample using 1 in 50 data points. This figure shows that the GP agrees very well with the correlation for $\phi < 1.05$. It is notable that the 95% confidence interval is very narrow, indicating a good GP fit. At rich equivalence ratios, the GP is lower than the normal minimisation, as would be expected, given the problems listed above which the GP should be immune to. However, it is also clear that the values for the GP are still higher than would be expected at rich conditions (compared with the schlieren results of Farrell et al. (2004), for example). The slightly wider confidence interval in this region reflects the lack of data. This is likely to be more pronounced at higher pressures. The confidence interval is very wide for $\phi < 0.7$ as would be expected as there is no data in this region.

It seemed that the GP was an improvement on the normal minimisation, although

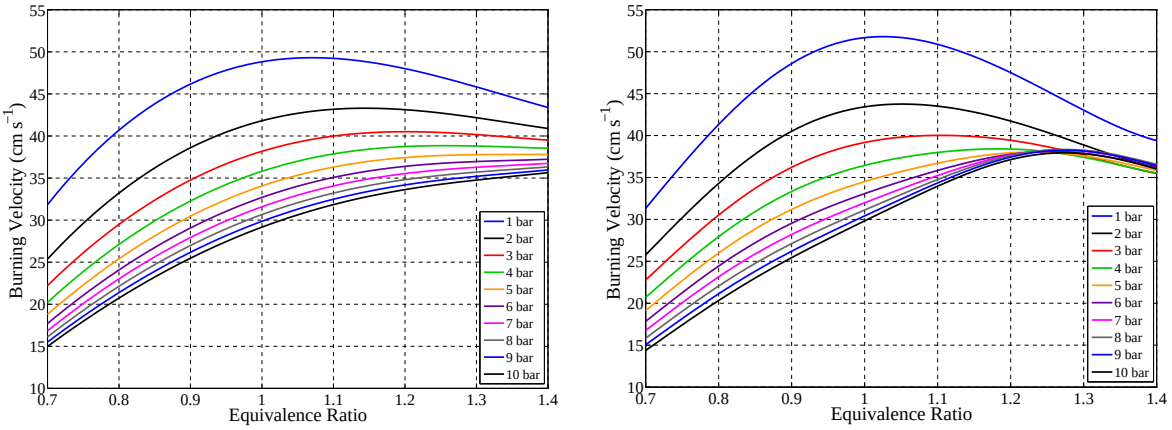

(a) Correlation

(b) Gaussian Process

Figure 5.15: Burning velocity of iso-octane at $T_u = 400$ K, $x_r = 0$ derived from (a) the correlation and (b) predictions of a Gaussian Process.

it can only output predictions at specified points rather than outputting coefficients for a general correlation, and it is an intensive process. Nonetheless, it was tested over a broader range of conditions to compare with the correlation (see Figure 5.15). There are major problems with the GP in this case. The trend in equivalence ratio for peak burning velocity is incorrect, as higher pressures should have a peak closer to stoichiometric, due to reduced dissociation. More worrying is that some of the lines cross, which is not possible, since at all conditions higher pressures should lead to slower burning velocities. Other curves plotted showed poor trends, and for this reason this approach was not pursued.

5.5.7 Smart Downsample

The problem with the existing data set was that the points were not evenly spaced, meaning that a fit would be biased towards the areas with more points. It was thought that this distribution problem could be solved by using the smart downsampling code from Section 5.5.6. This aims to create a data set which does not contain any points closer than a set Euclidean distance in the parameter space. This would have the effect of deleting points in the lean, low pressure area, while leaving most of those in the rich, high pressure area. This should lead to a more balanced set, allowing fitting of the

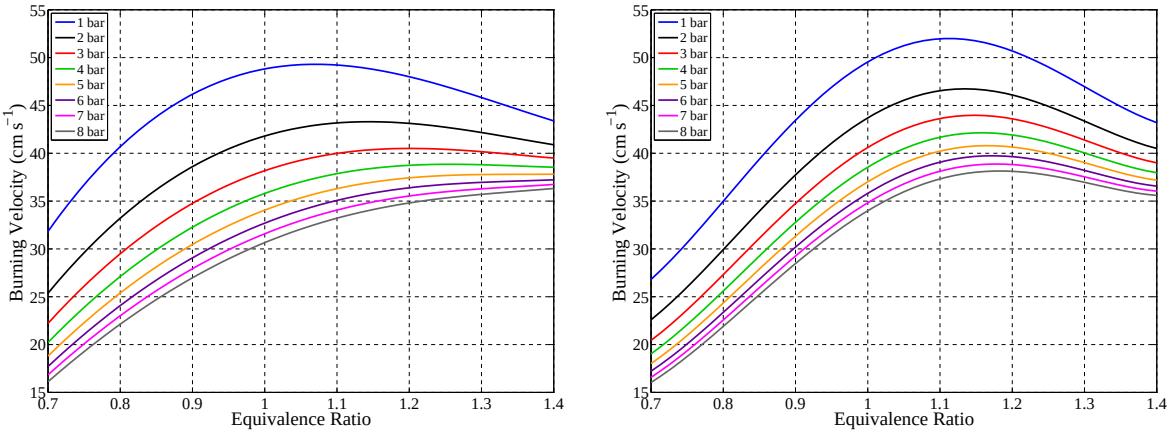

(a) Full Data Set

(b) Downsampled Data Set

Figure 5.16: Burning velocity of iso-octane at $T_u = 400$ K, $x_r = 0$ derived from (a) the correlation fitted to the entire iso-octane data set and (b) fitted to a downsampled set.

correlation without bias.

Different Euclidean distances were tested with the iso-octane data set. The optimum was found to be 0.4, with the three variables normalised by their respective ranges. As in Section 5.5.6, a 1 in 3 crude prefilter was required to reduce the data set of 21,720 points (no residuals were included) down to 7240. A Euclidean distance of 0.4 led the smart downsample algorithm to reduce this to only 11 points. Figure 5.16 shows that the downsampling led to higher values of burning velocity around stoichiometric, and clear turning points in the range $1.1 < \phi < 1.2$. However, the trend in the equivalence ratio for peak burning velocity is incorrect, as the peak should move closer to stoichiometric as pressure increases. Also, the result is highly sensitive to the Euclidean distance chosen.

5.5.8 Limited Datasets

Another method of reducing the data set was to remove points above a certain pressure or equivalence ratio before fitting. This would delete any remaining points in the data set that may be affected by cellularity. These should be very few, due to careful selection with the aid of the cellularity detection algorithm. It would also balance the set to avoid bias. The major downside of this would be a reduced range of validity for

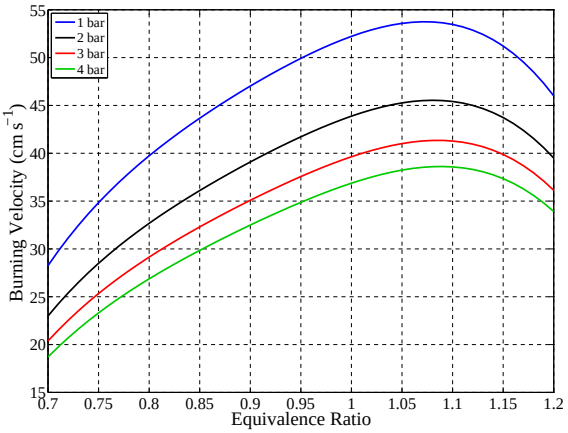

(a) $\phi \leq 1$

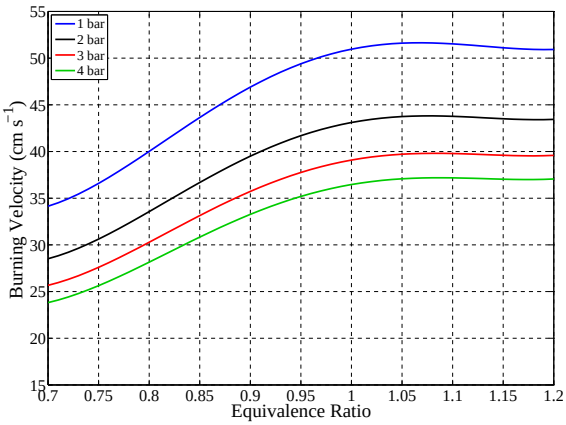

(b) $\phi < 1.2$ and $p_u < 4$ bar

Figure 5.17: Burning velocity of iso-octane at $T_u = 400$ K, $x_r = 0$ derived from partial data sets.

the correlation, limiting its usefulness. However, most of the interest for automotive purposes is around stoichiometric, so it may be worth sacrificing rich data to guarantee accurate values in this range.

Figure 5.17 shows the correlation fitted to two different partial iso-octane data sets. In Figure 5.17a, a peak in burning velocity is seen at $\phi \approx 1.07$ even though there is no data present in the set richer than stoichiometric, so this is an extrapolation. In contrast, in Figure 5.17b the peak are not well defined, even though there is data at these equivalence ratios in this set.

A hybrid method is to limit by the product of equivalence ratio squared and pressure, as this forms a suitable curve on a plot of pressure against equivalence ratio. It deletes most of the rich, high pressure data, while maintaining a more balanced data set than those shown in Figure 5.17. Figure 5.18 shows a data set where data above the line $p_u \times \phi^2 = 3$ was removed. This led to a smooth series of burning velocity curves, with peaks in the range $1.05 < \phi < 1.11$.

5.5.9 Conclusions

It is clear that the correlation plotted as it is gives poor results. Various methods of eliminating the problems in the data set and fitting process have been tested. It

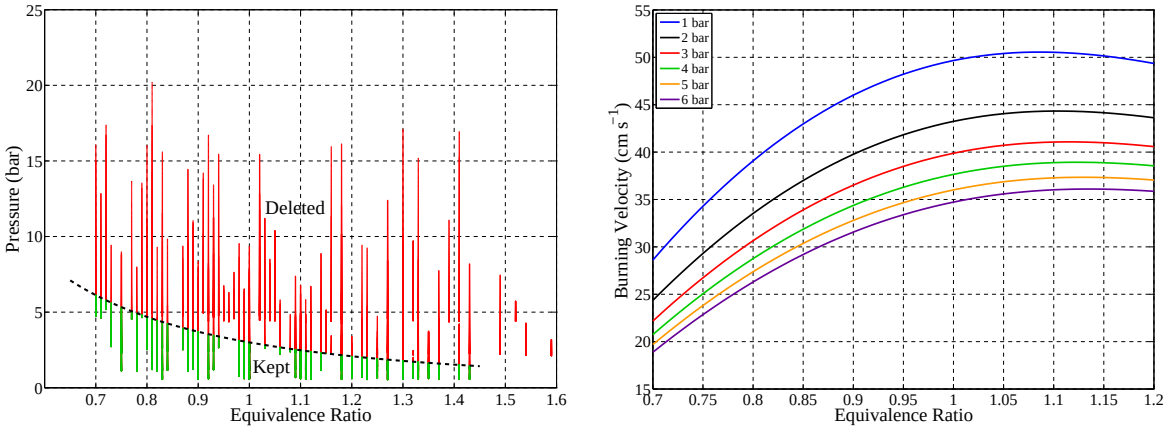

Figure 5.18: Iso-octane (a) data set limited by $p_u \times \phi^2 < 3$ and (b) the resultant burning velocities at $T_u = 400$ K, $x_r = 0$.

was decided to use limited data sets using the criterion $p_u \times \phi^2 < k$, where k is some constant. It may be possible to use the same k for all fuels, but it may also have to be adjusted to find suitable results. The same process was applied to residuals data, since the fitting for residuals relies on having non-residuals data at the same conditions in order to ascertain how much the residuals level has reduced the burning velocity.

With sparse data the correlation equation 'struggles', and which data is selected has a significant effect on the outcome.

5.6 Experimental Consistency

After a suitable dummy experiment, ten consecutive tests were carried out with a fixed stoichiometry iso-octane/air mixture at an initial temperature of 400 K and an initial pressure of 4 bar. Nine of these experiments gave a reading on the lambda sensor of 1.08, and one gave 1.07. The burning velocity for each was calculated from both pressure and schlieren data.

Figure 5.19 shows ten similar pressure traces leading to similar burning velocities. The schlieren results of Figure 5.20 show one experiment slightly apart from the others, but otherwise the results are very close together.

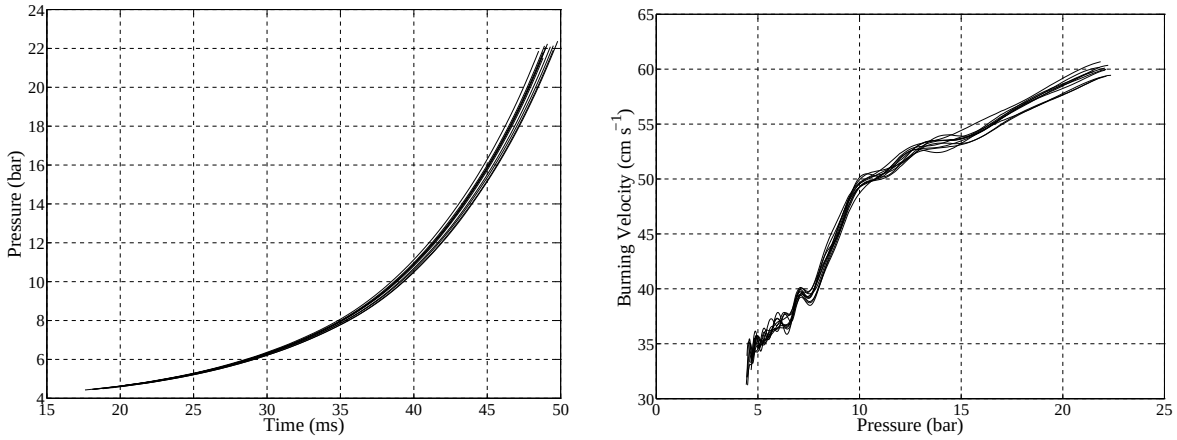

(a) Pressure (b) Stretched Burning Velocity

Figure 5.19: (a) Pressure traces and (b) calculated burning velocities for ten consecutive experiments with iso-octane ($T_0 = 400$ K, $p_0 = 4$ bar, $x_\mathrm{r} = 0$).

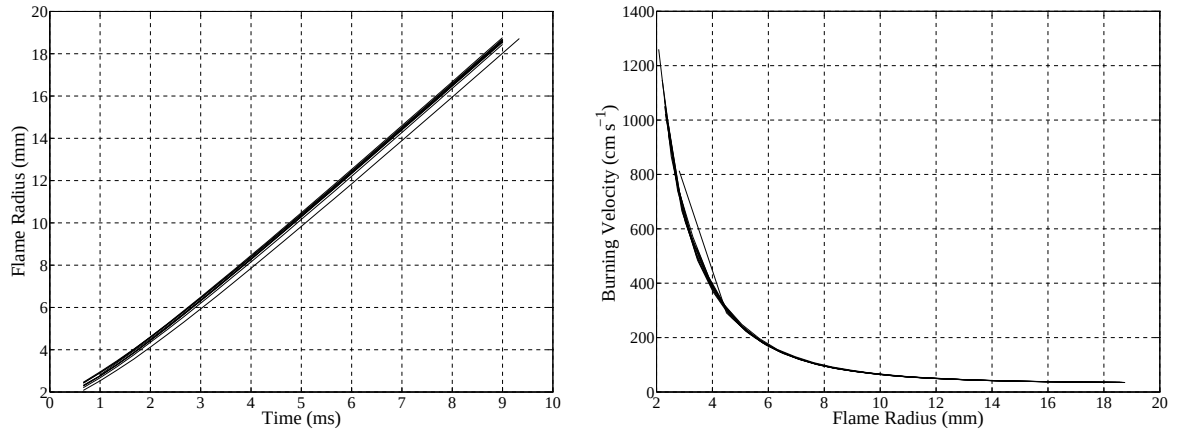

(a) Radius (b) Stretched Burning Velocity

Figure 5.20: Measured schlieren (a) radii and (b) calculated burning velocities for ten consecutive experiments with iso-octane ($T_0 = 400$ K, $p_0 = 4$ bar, $x_\mathrm{r} = 0$).

5.7 Experimental Error

Because the current method relies on fitting a correlation to a large number of experiments, any non-systematic errors in initial temperature, initial pressure, equivalence ratio or residual mole fraction should be largely eliminated, improving the signal-to-noise ratio. An error in equivalence ratio would be a function of the incremental errors in pressure and temperature measurements at the various stages in the filling and mixing process, and the oxygen content of the air. However, the lack of control over equivalence ratio due to the syringe problems (see Section 5.1.2) meant that these became irrelevant, and errors in the lambda sensor were the sole factor.

5.8 Sensitivity Analysis

5.8.1 Experimental Pressure

Although the initial conditions of each experiment are important, the only two variables measured during the combustion are pressure and time. As the timing accuracy of the DAQ system is very high, error in the pressure transducer and charge amplifier will be far more significant.

A pressure trace for a typical experiment (stoichiometric iso-octane, $T_0 = 380$ K, $p_0 = 2$ bar, $x_r = 0$) was modified so that the pressure readings were artificially increased by 1% of the full span (20 bar), giving a zero error of 0.2 bar. A second copy was multiplied by 1.01 to give a span error of 1%. These modified pressure traces and the original were processed in the normal way to give graphs of burning velocity against pressure and then compared.

Figure 5.21a shows that the zero error had no effect on the burning velocity. This is due to the pressure datum being set from the early pressure data (see Section 4.6.1) that negates the effect of the pressure shift. Figure 5.21b shows that the effect of a 1% span error is small (less than 0.4%), and furthermore the error changes sign as the experiment progresses, so the mean difference is likely to be small.

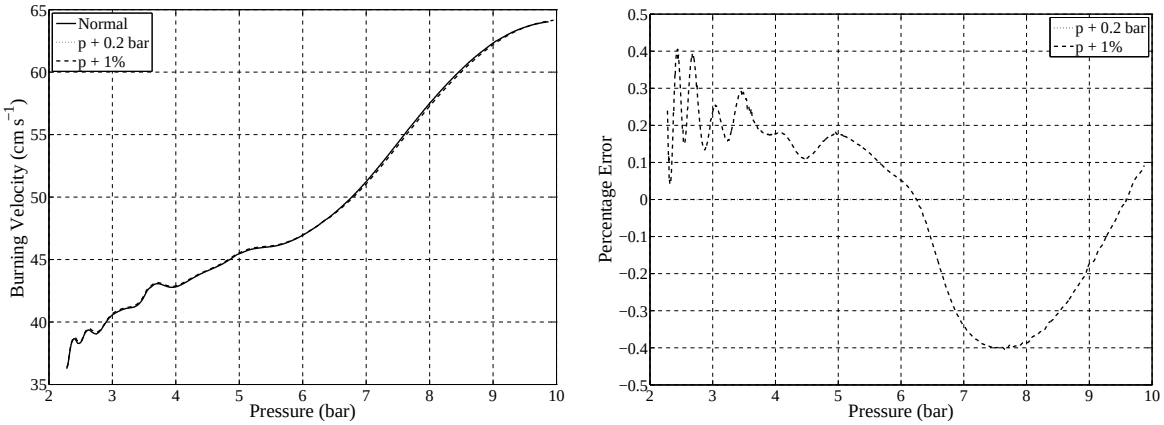

(a) (b)

Figure 5.21: Effect of experimental pressure zero and span error on burning velocity.

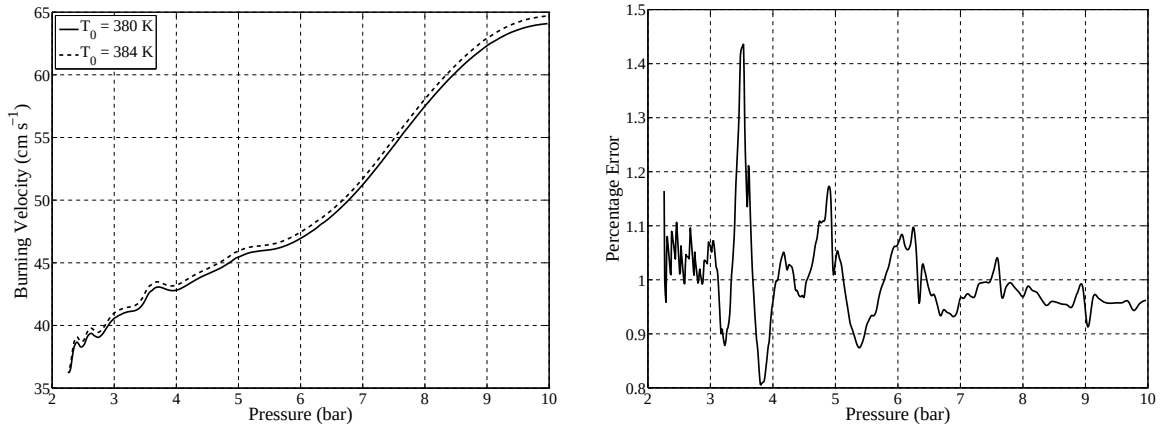

Figure 5.22: Effect of initial temperature error on calculations of burning velocity.

5.8.2 Initial Temperature

An error in initial temperature will bring about an error in burning velocities, since higher temperatures lead to higher burning velocities, but also an error in the calculation of the burning velocity, since the zone files are generated for an exact initial temperature.

This second error can be quantified by generating a second zone file with a different initial temperature (380 K + 1% $\approx$ 384 K). The same experimental pressure file can be processed using the two zone files and the resultant burning velocities compared.

Figure 5.22 shows that there is a maximum burning velocity difference of ≈ 0.7 cm s^{-1} between the two temperatures, which is approximately 1%.

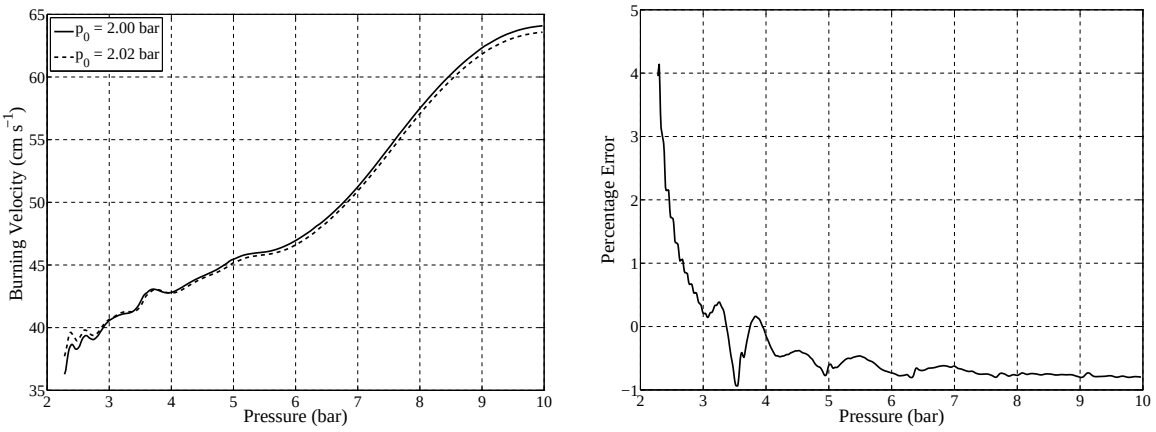

Figure 5.23: Effect of initial pressure error on calculations of burning velocity.

5.8.3 Initial Pressure

A similar exercise can be undertaken for initial pressure. The initial pressure was increased to 2.02 bar. Note that this is not the same as the *experimental* pressure in Section 5.8.1. After the noisy early burn period (which would not normally be used), the percentage error decreases to be less than 1% (see Figure 5.23). The error is negative because an increase in pressure leads to a decrease in burning velocity.

5.8.4 Equivalence Ratio

For equivalence ratio, the value was increased from 1.00 to 1.01. The result was a small error in burning velocity, but surprisingly the error was negative (see Figure 5.24). This was unexpected, as an increase in equivalence ratio would lead to an increase in burning velocity, since the equivalence ratio is less than that required for peak burning velocity, which is usually in the region 1.05–1.15. For an equivalence ratio away from stoichiometric, a larger error would be expected.

5.8.5 Residual Fraction

For residual mole fraction, the BOMB program has a resolution of only 2 dp, hence the smallest difference possibly was 0.01. Hence experiments with $x_\mathrm{r} = 0.20$ and $x_\mathrm{r} = 0.21$ were compared, giving an error of 5%. All the other conditions were the same as the

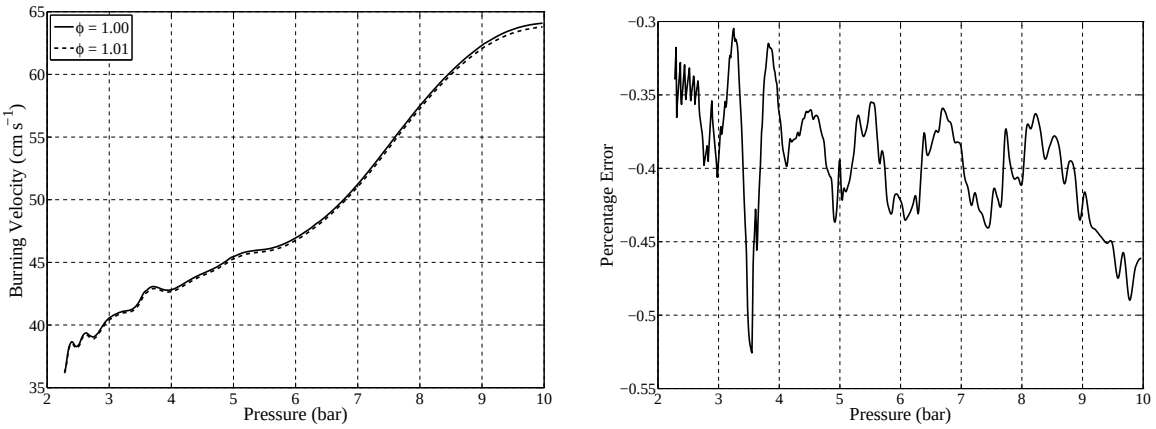

Figure 5.24: Effect of equivalence ratio error on calculations of burning velocity.

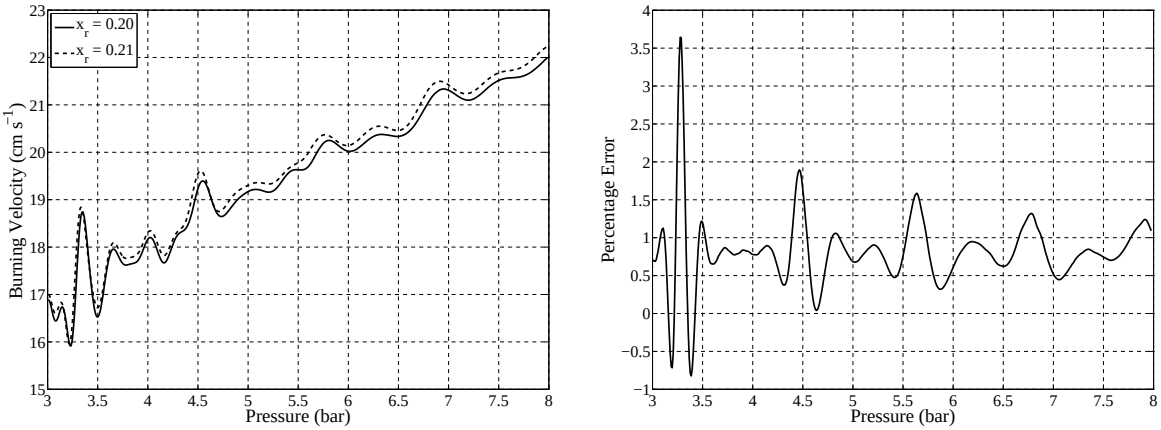

Figure 5.25: Effect of residuals mole fraction 5% error on calculations of burning velocity.

previous sections. This 5% error led to an error in burning velocity of less than 5% (see Figure 5.25).

5.9 Conclusions

The experiments showed good consistency, but control of equivalence ratio was poor. This was due to heat conduction along the syringe causing premature evaporation of the fuel. This meant that equivalence ratio depended on the volume of fuel to be injected, the temperature, and the volume of the syringe. These problems were circumvented by measuring the combustion products using a lambda sensor.

The combustion model, algorithm to determine burning velocities, and the ther-

modynamic data was shown to work well, and the model was validated against other combustion programs.

Problems were found with the fitting of the experimental correlation to the data. Due to cellular data being excluded, there were many more lean than rich data points, and more at low pressures. This meant that the fit became distorted, as all points counted equally. Hence the data sets were limited using the inequality $p_{\mathrm{u}} \times \phi^2 < k$, where k is some constant. This evened up the data and led to better trends for most fuels.

The fitting process helped to eliminate most of the error in each individual experiment. Sensitivity analyses showed that errors in the four major parameters led to smaller errors in the resulting burning velocities.

Chapter 6

Results

6.1 General Remarks

Experiments were conducted at nominal equivalence ratios of 0.7 to 1.4 (0.8–1.4 for gaseous fuels), in increments of 0.1. Four initial pressures were tested — 0.5, 1, 2 and 4 barA. For the liquid fuels, three initial temperatures were tested (310, 380 and 450 K), but for some fuels, experiments at 310 K were not possible as the temperature was insufficient to guarantee complete evaporation. Liquid fuels were tested with residual mole fractions of 0.1, 0.2 and 0.3, but again this was not possible at 310 K, due to water condensation.

The methane and n-butane results do not include any residuals, as they were performed before the installation of the oven, which was required to prevent condensation of the water vapour in the residuals. The lack of oven also meant that the initial temperature could not be controlled. The ranges measured are given in Table 6.3. They do not include any schlieren image data, since the schlieren system had not been constructed.

For each fuel, a test matrix was generated, allowing tests to be neglected if one more likely to ignite had previously failed. This avoided wasting time on experiments that would never ignite. Tests were less likely to ignite at low pressures, low temperatures, equivalence ratios far from peak burning velocity ($\phi \approx 1.1$) and high residual mole

Table 6.1: Coefficients used to apply data set limiting prior to fitting using the condition $p_u\phi^2 < k$ as described in Section 5.5.2. A lack of a value for k implies no limiting i.e. the data was unchanged.

Fuel	k
Methane	-
n-Butane	-
Iso-octane	3
Ethylbenzene	5
n-Heptane	3
Toluene	5
Ethanol	-

fractions. The pressure effect is due to having fewer molecules in the spark gap, which are required to collide in order to form a continuous reaction wave. The other variables are indicative of a low flame speed, which will be insufficient to overcome the quenching effect of the large stretch rate at low radii.

Most of the current literature data for both liquid and gaseous fuels is at ambient pressure and temperature. As the lowest initial temperature in this study was 310 K (289 K for the gaseous fuels), the lowest initial pressure is 0.5 bar, and no pressure data is used from the early part of combustion, there will be no data at 298 K and little data at 1 bar. Hence a plot of the correlation at ambient temperature would be an extrapolation outside the range of validity, leading to poor results. Far better agreement with the literature was found at the higher temperatures and pressures that are the main focus of this study.

The liquid fuel results showed evidence of the fitting problems described in Section 5.5. Some required data set limiting by the inequality $p_u \times \phi^2 < k$, with values of k given in Table 6.1. This led to reduced ranges of validity, which are given in Table 6.2.

Coefficients were determined for each fuel for the correlation given in Equation (4.37):

$$S_u = \left[S_{u,0} + S_{u,1}(\phi - 1) + S_{u,2}(\phi - 1)^2 + S_{u,3}(\phi - 1)^3 + S_{u,4}(\phi - 1)^4\right] \times T^{\left(\eta_0 + (\phi-1)\eta_1\right)} p^{\left(\beta_0 + (\phi-1)\beta_1\right)} \left(1 - \mu_1 x_r^{\left(\mu_2 + (\phi-1)\mu_3\right)}\right)$$

Table 6.2: Range of validity of the correlation for each fuel, and mixtures (all mixtures had the same range).

	ϕ		p_u (bar)		T_u (K)		x_r	
Fuel	Min	Max	Min	Max	Min	Max	Min	Max
Methane	0.8	1.4	0.8	11	310	470	0	0
n-Butane	0.8	1.4	0.8	10	320	460	0	0
Iso-octane	0.7	1.3	0.7	6	340	640	0	0.3
Ethylbenzene	0.7	1.3	0.7	10	410	640	0	0.3
n-Heptane	0.7	1.4	0.7	6	340	630	0	0.3
Toluene	0.7	1.4	0.8	11	400	640	0	0.3
Ethanol	0.7	1.2	0.7	17	400	630	0	0.3
Mixtures	1	1	0.8	6	400	640	0	0

These coefficients are listed in Table 6.11, valid in the ranges given in Table 6.2. Specifications of the fuels used are given in Table A.6.

6.2 Coil Energy

The effect of ignition energy is a contentious issue with regard to burning velocity measurements (see Section 2.5.7). Calculating the spark energy to compare with known minimum ignition energies is very difficult, as even if HT energy is measured (as in Section 3.4.3), it is difficult to estimate the spark efficiency and hence what proportion of the HT energy is imparted to the mixture. However, the variable dwell time ignition system allows the effect of varying coil energy on burning velocity to be studied.

Experiments were conducted with stoichiometric iso-octane at an initial pressure of 1 bar and an initial temperature of 400 K. The dwell time was varied from 0.35–4 ms, giving coil energies from 2.2–276.0 mJ. Each coil energy was tested twice by a sweep down and then up the coil energies to be tested.

Figure 6.1a shows that there is only a small difference between the burning velocities for the different coil energies. Figure 6.1b shows the burning velocity for each experiment at 2.5 barA. There is a small reduction in burning velocity at ignition energies below 20 mJ.

A very similar trend is shown from the schlieren image data (see Figure 6.2). Impor-

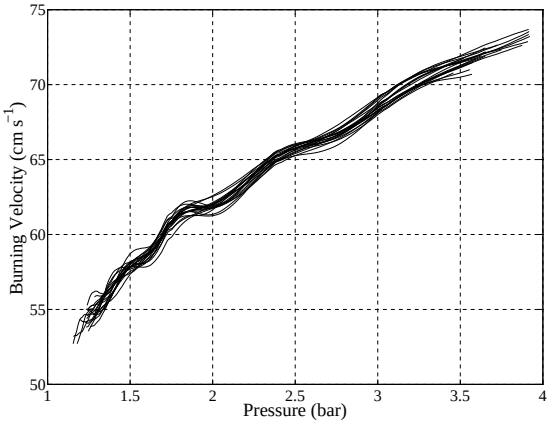

(a) Burning velocity against pressure.

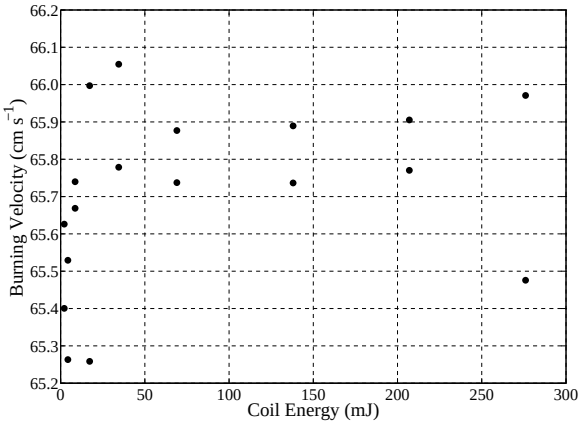

(b) Burning velocity against coil energy at 2.5 barA, 501 K.

Figure 6.1: Effect of dwell time (and hence coil energy, in the range 2.2–276 mJ) on burning velocity for stoichiometric iso-octane with $T_0 = 400$ K, $p_0 = 1$ bar.

Table 6.3: Minimum and maximum conditions in the methane and n-butane data sets.

		Methane		n-Butane	
Property	Unit	Min	Max	Min	Max
T_0	K	289	294	292	298
p_0	barA	0.5	4.0	0.5	4.0
ϕ	-	0.8	1.4	0.8	1.4
p_u	barA	0.760	17.1	0.792	14.2
T_u	K	309	476	319	469
S_u	cm s^{-1}	6.15	49.5	17.9	61.5
S_f	cm s^{-1}	18.9	190	34.5	234
α	s^{-1}	5.38	67.1	9.09	83.6
r_b	mm	43.2	77.2	47.8	77.3
t	ms	26.7	192	21.7	90.8

tantly, there was no evidence of over-driving of the flame at higher coil energies. With this in mind, the dwell time was left at 4 ms, equating to 276 mJ coil energy. Again, it should be noted that the HT energy will be less than this (68 mJ from Section 3.4.3), and the actual spark energy less still.

6.3 Methane

Minimum and maximum values for all parameters in the data set are given in Table 6.3.

Figure 6.3 shows the correlation plotted for constant T_u, p_u and ϕ respectively.

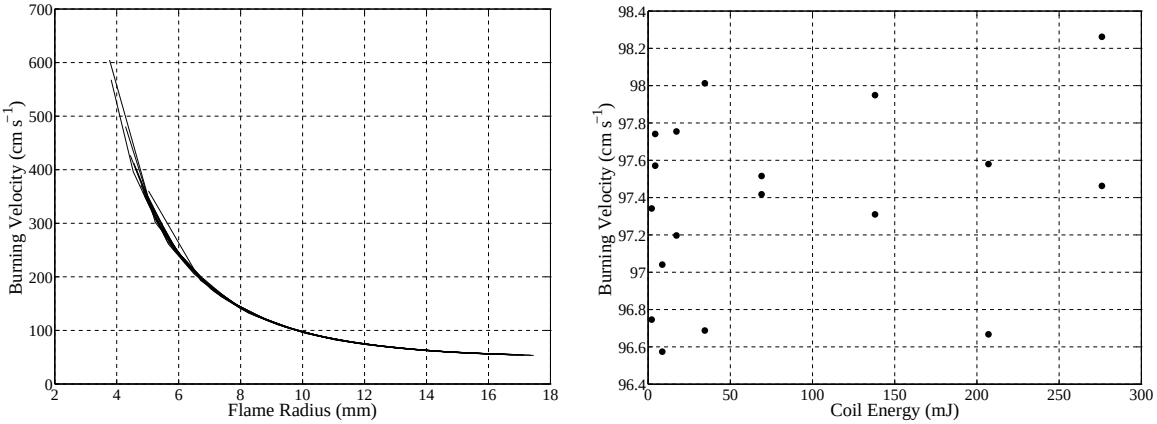

(a) Burning velocity against flame radius (b) Burning velocity against coil energy at 10 mm

Figure 6.2: Effect of dwell time (and hence coil energy, in the range 2.2–276 mJ) on schlieren-derived burning velocity for stoichiometric iso-octane with $T_0 = 400$ K, $p_0 = 1$ bar.

Figure 6.3a shows that burning velocity decreases non-linearly with pressure i.e. the effect of increasing pressure is larger at lower pressures. The equivalence ratio for peak burning velocity shifts closer to stoichiometric as pressure increases, due to decreased dissociation. Figure 6.3b shows that burning velocity increases with temperature. The equivalence ratio for peak burning velocity also increases with temperature due to increased dissociation. The non-linearities in pressure and temperature are shown more clearly in Figures 6.3c and 6.3d. The former shows that burning velocity is roughly linear with pressure at high pressures, but not at low pressures.

Methane has been tested extensively in the literature at 298 K, 1 bar. Unfortunately, this is outside of the range of validity of the correlation, but was included in the modelling data set of Hegheş (2006) used in Section 4.7.2.1. Figure 6.4 shows good agreement with the modern literature, giving a burning velocity of approximately 36 cm s^{-1} at stoichiometric.

Good agreement between the experimental correlation and the literature data at elevated pressure and temperatures can be seen in Figures 6.5, 6.6 and 6.7. At these conditions, the values for the modelling data are lower than the literature data.

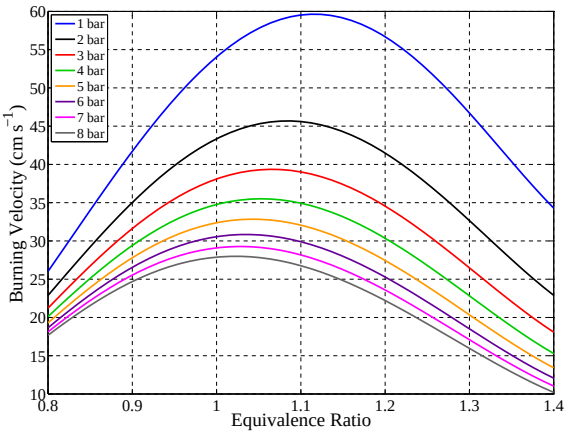

(a) $T_\mathrm{u} = 400$ K, $p_\mathrm{u} = 1$–8 bar

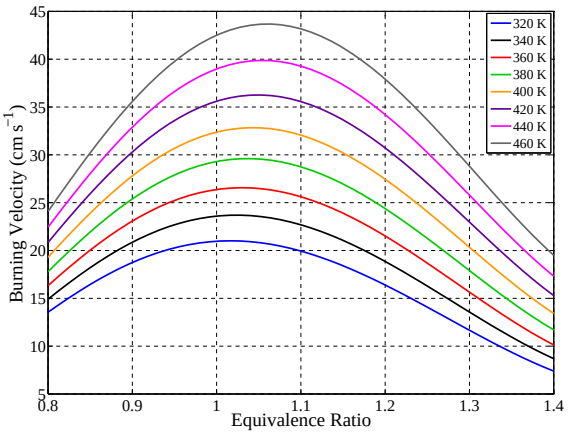

(b) $p_\mathrm{u} = 5$ bar, $T_\mathrm{u} = 320$–460 K

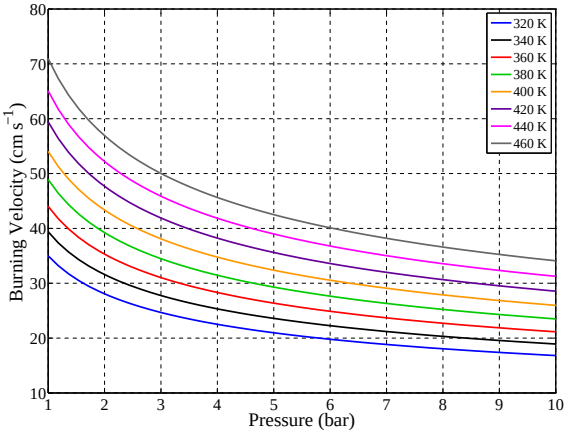

(c) $\phi = 1$, $T_\mathrm{u} = 320$–460 K

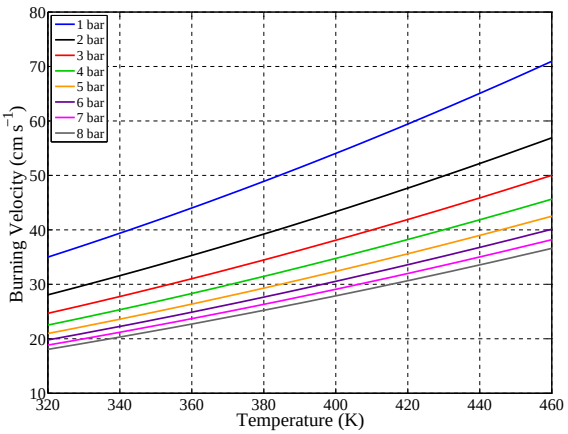

(d) $\phi = 1$, $p_\mathrm{u} = 1$–8 bar

Figure 6.3: The methane experimental correlation.

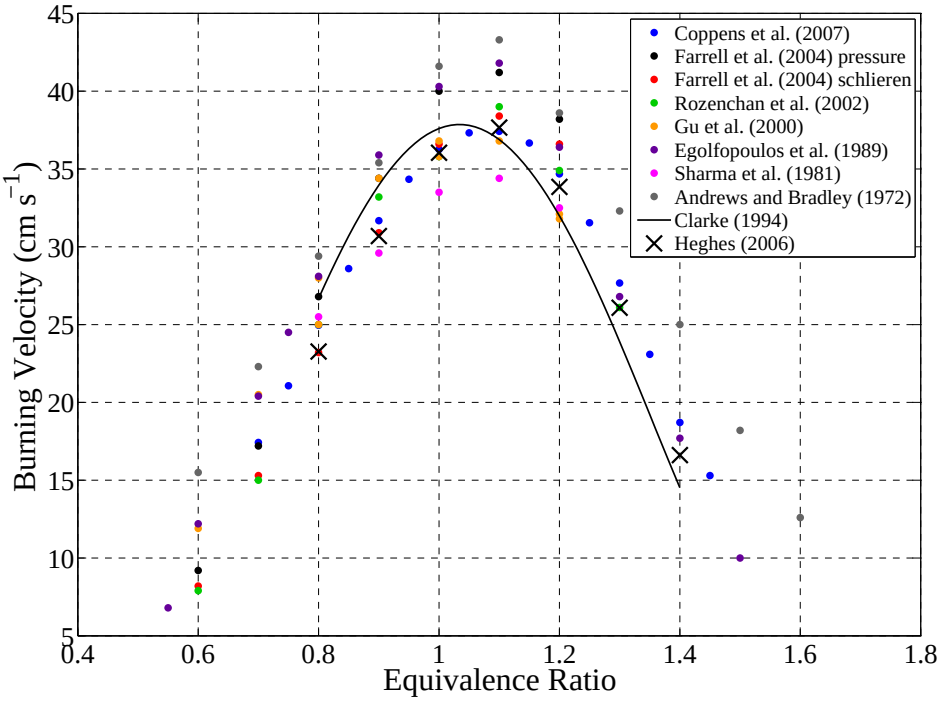

Figure 6.4: Comparison of modelling data of Heghes (2006) with literature data for the burning velocity of methane at $T_0 = 298$ K and $p_0 = 1$ bar.

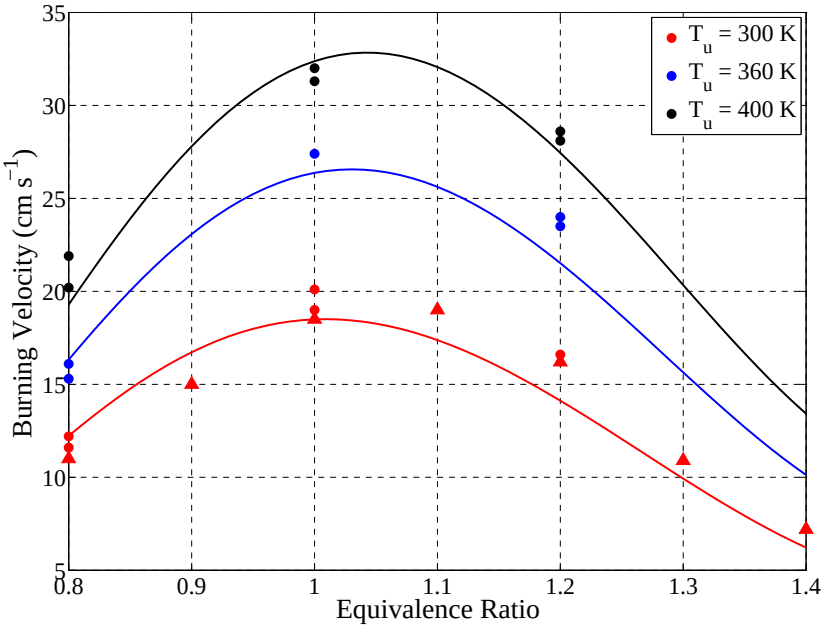

Figure 6.5: Experimental methane data at 5 bar. Lines are current experimental data, circles are from Gu et al. (2000) and triangles from Rozenchan et al. (2002).

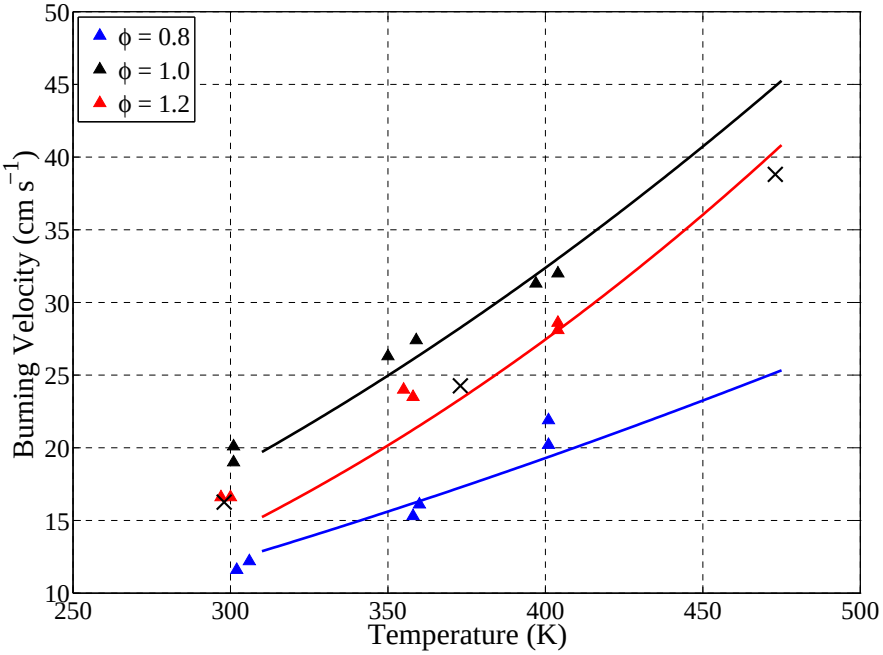

Figure 6.6: Experimental and modelling methane data at 5 bar. Lines are current experimental data, crosses are modelling data from Hegheş (2006) and triangles are experimental data from Gu et al. (2000).

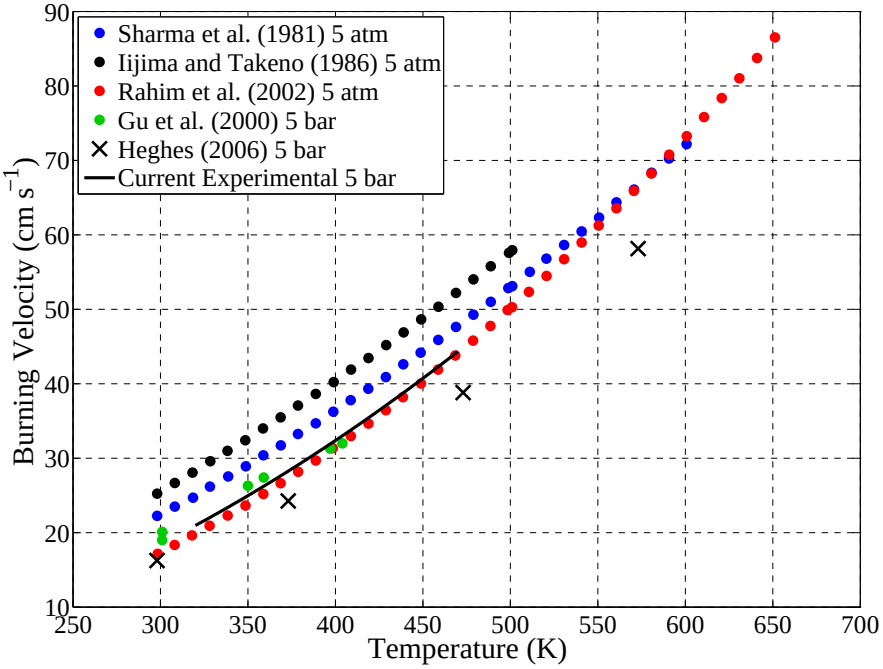

Figure 6.7: Stoichiometric experimental and modelling (Hegheş, 2006) methane data at 5 bar along with experimental results from Sharma et al. (1981), Iijima and Takeno (1986), Rahim et al. (2002) and Gu et al. (2000) at 5 bar and 5 atm.

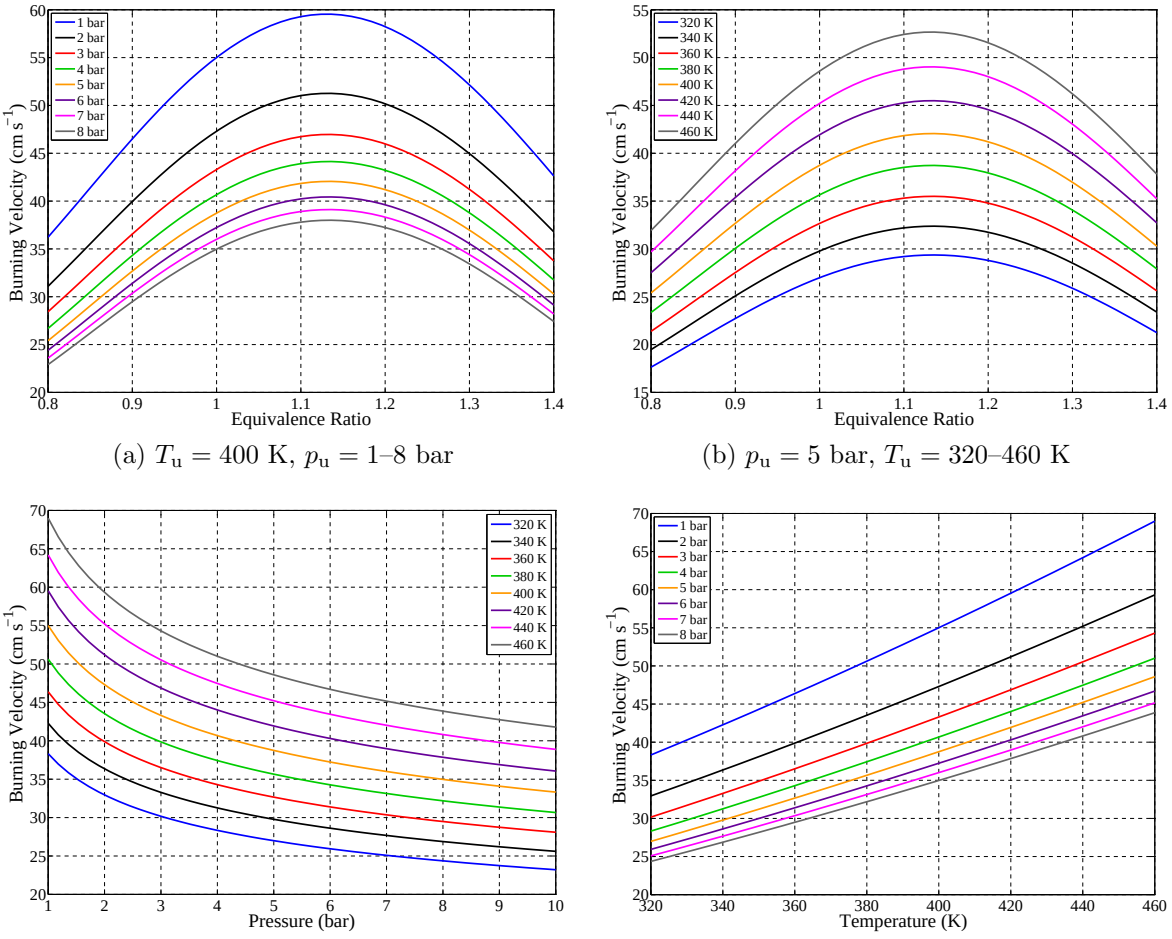

(a) $T_u = 400$ K, $p_u = 1$–8 bar

(b) $p_u = 5$ bar, $T_u = 320$–460 K

(c) $\phi = 1$, $T_u = 320$–460 K

(d) $\phi = 1$, $p_u = 1$–8 bar

Figure 6.8: n-Butane experimental correlation.

6.4 n-Butane

Plots of the correlation for the burning velocity of n-butane are shown in Figure 6.8. Figure 6.8a shows that at low pressure, the burning velocity of n-butane is similar to that of methane, but at high pressure it is greater than methane. The plots show almost no change in the equivalence ratio for peak burning velocity with either pressure or temperature. The only literature data at elevated temperature is from Farrell et al. (2004) (see Figure 6.28). This shows far higher burning velocities than are found from the correlation, but this is also the case for methane, where the pressure-derived results of Farrell et al. (2004) are about 5 cm s^{-1} higher than the modern literature (see Figure 6.4), and they themselves suggest that their values are 20–30% higher than results from other methods.

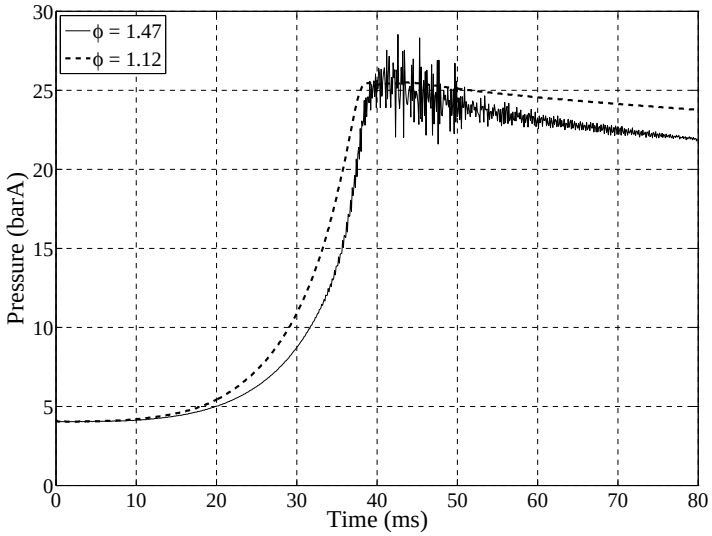

Figure 6.9: Pressure traces from two iso-octane experiments at $T_0 = 450$ K, $p_0 = 4$ bar, $x_r = 0$, showing oscillations in the richer experiment.

6.5 Iso-octane

In high pressure rich mixtures, oscillations were seen on the pressure trace after the maximum pressure had been reached. These corresponded with a clearly audible 'ping' sound. In extreme cases this sound was loud and the oscillations extended to before the point of maximum pressure. These were similar to those noted by Bradley et al. (2000) and Farrell et al. (2004). A frequency of 4 kHz was noted by Farrell et al. (2004) for these oscillations, independent of the fuel. This frequency was linked to the transit time of an acoustic wave across the chamber (diameter 16.5 cm).

Figure 6.9 shows two experiments with different equivalence ratios. The rich experiment shows oscillations with a frequency of approximately 3.9 kHz. This is close to the value measured by Farrell et al. (2004), for a similarly sized vessel. These oscillations could create a lot of noise in the calculated burning velocity data, but since they only occur at rich, high pressure conditions, the flame is always cellular and hence the affected pressure data is discarded.

The experimental correlation is shown in Figure 6.10. The trends in equivalence ratio for peak burning velocity with pressure are the opposite of that expected. Figure 6.10d shows the effect of residuals. A small residual level makes a large difference

Table 6.4: Minimum and maximum conditions in the iso-octane, n-heptane and ethanol data sets.

		Iso-octane		n-Heptane		Ethanol	
Property	Unit	Min	Max	Min	Max	Min	Max
T_0	K	310	450	310	450	310	450
p_0	barA	0.5	4.0	0.5	4.0	0.5	4.0
ϕ	-	0.70	1.43	0.68	1.49	0.67	1.49
x_r	-	0	0.3	0	0.3	0	0.3
p_u	barA	0.533	6.12	0.620	6.48	0.612	17.7
T_u	K	319	649	323	649	367	650
S_u	cm s^{-1}	7.25	114	13.5	127	7.03	125
S_f	cm s^{-1}	15.0	355	47.1	369	17.7	401
α	s^{-1}	5.86	196	13.4	175	5.68	187
r_b	mm	33.5	77.8	36.6	77.7	38.8	77.8
t	ms	11.4	161	11.5	92.9	10.3	221.7

to the burning velocity. A residual mole fraction of approximately 0.17 would cause the burning velocity to halve at these conditions.

Figures 6.11, 6.12 and 6.13 show the correlation in relation to the literature data at elevated pressures and temperatures. The correlation is at the lower end of the spectrum of data, but mostly within the bounds of other data. Figure 6.11 shows a large scatter in the results of Bradley et al. (1998). These are thought to be due to the large error in extrapolating schlieren data to zero stretch. In Figure 6.12, it is likely that the results of Metghalchi and Keck (1982) would have included cellular data. To make a comparison, an iso-octane data set was constructed which also included cellular data. This is shown as a dashed line. At rich equivalence ratios, this correlation is higher than the normal one, and better fits the data of Metghalchi and Keck (1982). For residuals, Figure 6.14 shows results using their simulated residuals (15% CO_2, 85% N_2). These give higher values of burning velocity than the correlation, but similar trends with residual mass fraction.

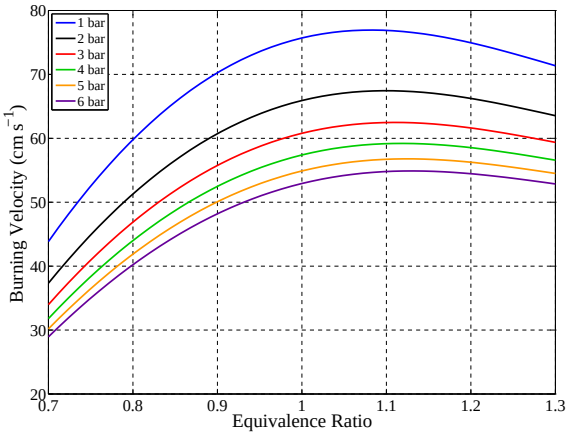

(a) $T_{\mathrm{u}} = 500$ K, $x_{\mathrm{r}} = 0$, $p_{\mathrm{u}} = 1$–6 bar

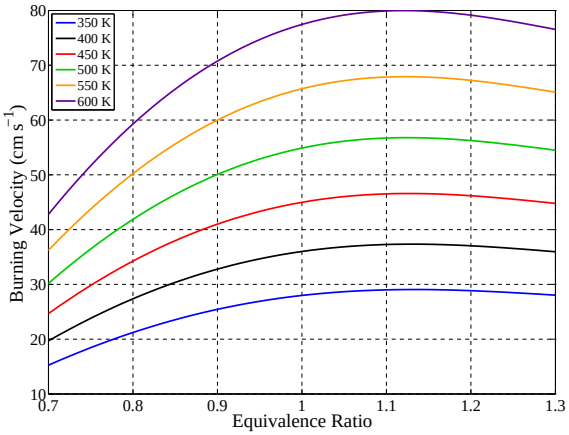

(b) $p_{\mathrm{u}} = 5$ bar, $x_{\mathrm{r}} = 0$, $T_{\mathrm{u}} = 350$–600 K

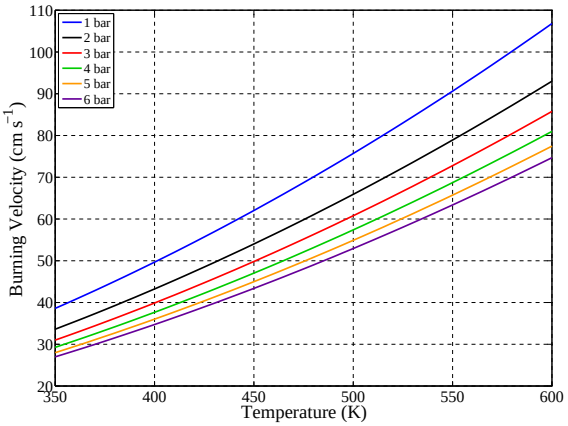

(c) $\phi = 1$, $x_{\mathrm{r}} = 0$, $p_{\mathrm{u}} = 1$–6 bar

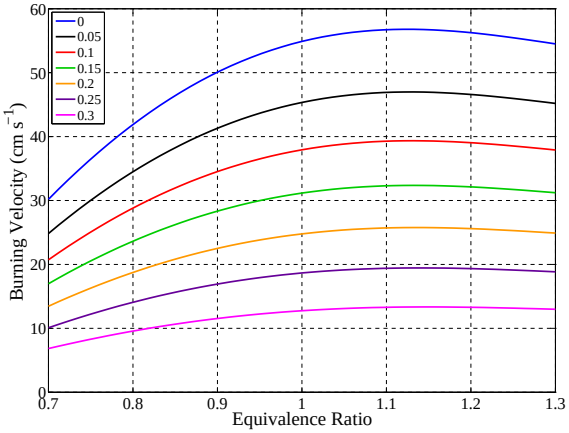

(d) $p_{\mathrm{u}} = 5$ bar, $T_{\mathrm{u}} = 500$ K, $x_{\mathrm{r}} = 0$–0.3

Figure 6.10: Iso-octane experimental correlation.

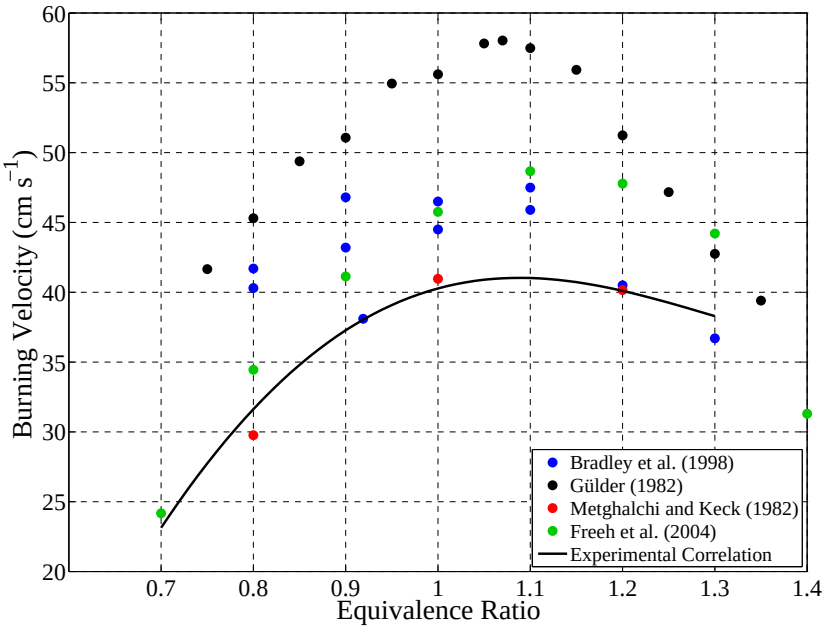

Figure 6.11: Comparison of iso-octane correlation and experimental results of Bradley et al. (1998), Gülder (1984), Metghalchi and Keck (1982) and Freeh et al. (2004) at $T_{\mathrm{u}} \approx 358$ K, $p_{\mathrm{u}} = 1$ bar, $x_{\mathrm{r}} = 0$.

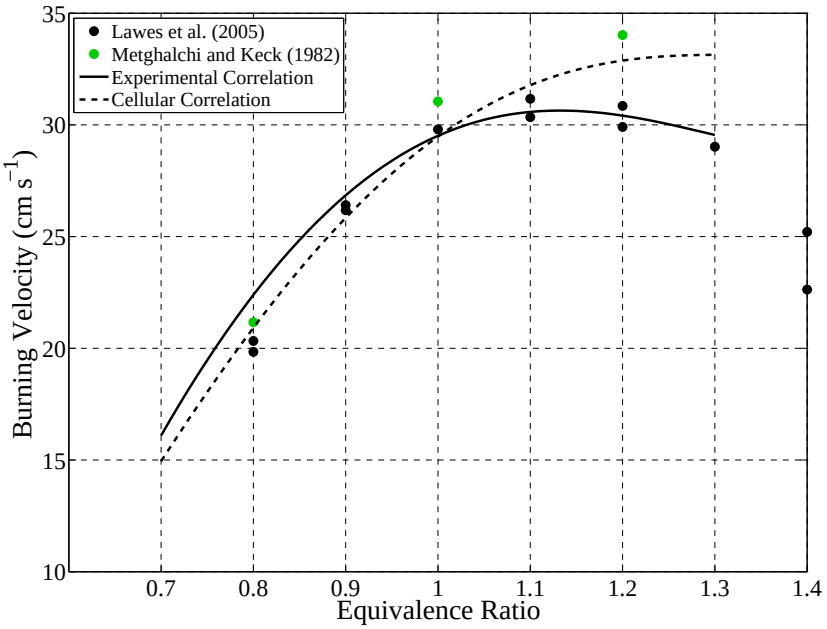

Figure 6.12: Comparison of iso-octane correlation and experimental results of Lawes et al. (2005) and Metghalchi and Keck (1982) at $T_{\mathrm{u}} = 360$ K, $p_{\mathrm{u}} = 5$ bar, $x_{\mathrm{r}} = 0$.

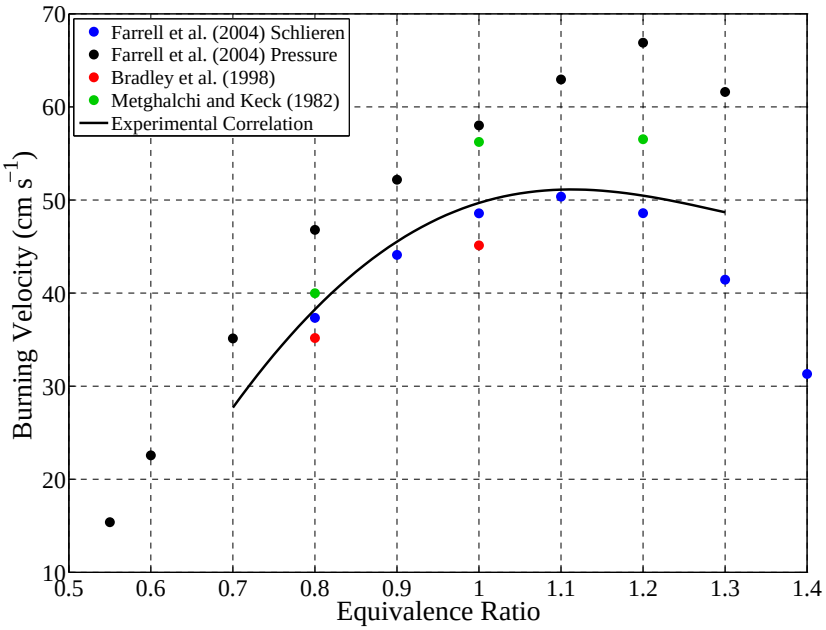

Figure 6.13: Comparison of experimental correlation for iso-octane with experimental results of Farrell et al. (2004), Bradley et al. (1998) and Metghalchi and Keck (1982) at $T_{\mathrm{u}} = 450$ K, $p_{\mathrm{u}} = 3$ atm, $x_{\mathrm{r}} = 0$.

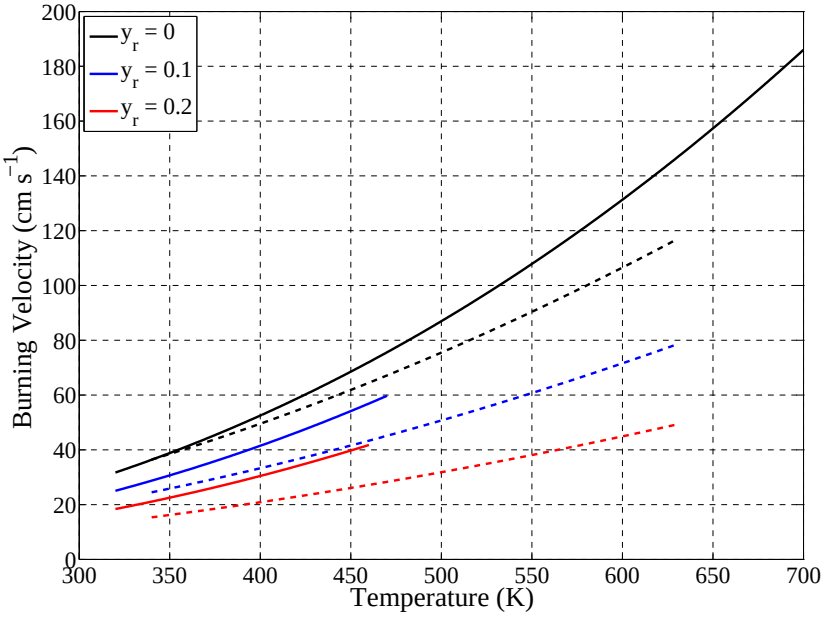

Figure 6.14: Comparison of stoichiometric iso-octane burning velocity correlation of Metghalchi and Keck (1982) (solid lines) and the current experimental correlation (dashed lines) with three different residual mass fractions, at 1 atm.

6.5.1 Onset of Cellularity

For each liquid fuel, the schlieren photography system and MATLAB image analysis allowed automatic detection of cellularity. The conditions at which cellularity is first detected are plotted in Figure 6.15 for iso-octane. Each plot in the figure shows the value of a different parameter at onset. Hence, each dot represents one experiment. Parabolae are fitted to the results for different initial pressures to make trends clearer. Note that these readings will be subject to error, as detecting the exact point of onset is subjective, and image properties such as darkness and thickness of the lines denoting cracks will vary. Also, some variables (such as pressure) will be rapidly increasing when cellularity occurs, so a slight error in time may lead to a large error in other variables.

There are more points at $p_0 = 4$ bar as cellularity is more likely to occur at higher pressures. For pressure and time at onset (Figures 6.15a and 6.15f), the points form a rough band, showing that these variables are not affected greatly by initial pressure. For the other parameters, differing trends are seen for each value of initial pressure, but they always occur in pressure order. Cellularity can occur in weak mixtures at high pressures.

A comparison of Figure 6.15e and Figure 6.16a shows that initial temperature has little effect on the radius at onset of cellularity, while initial pressure has a larger effect. Figure 6.16b shows that residuals delay the onset of cellularity. In some cases, residuals prevent the onset of cellularity entirely, but this is not clear from the figure, as the fact that there were more residuals data points than non-residuals was due to there being fewer experiments undertaken with residuals, and also the fact that residuals led to cracks which did not appear as dark in the schlieren images, and so were less likely to be detected.

6.6 Ethylbenzene

Plots of the correlation for the burning velocity of ethylbenzene are shown in Figure 6.17. Figure 6.17d shows that burning velocity decreases non-linearly with residual

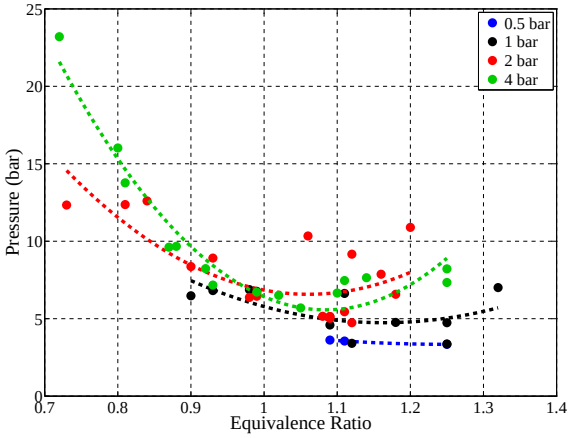

(a) Pressure

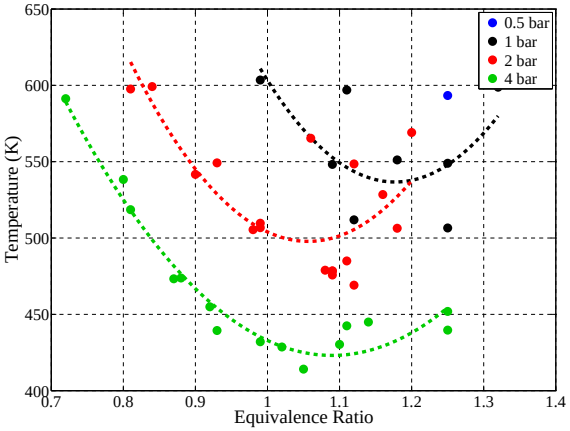

(b) Temperature

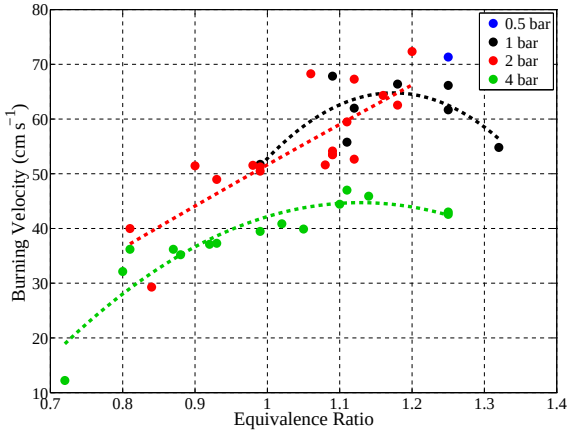

(c) Burning Velocity

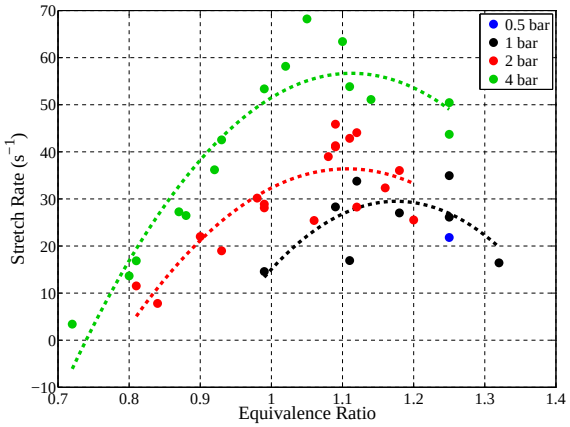

(d) Stretch Rate

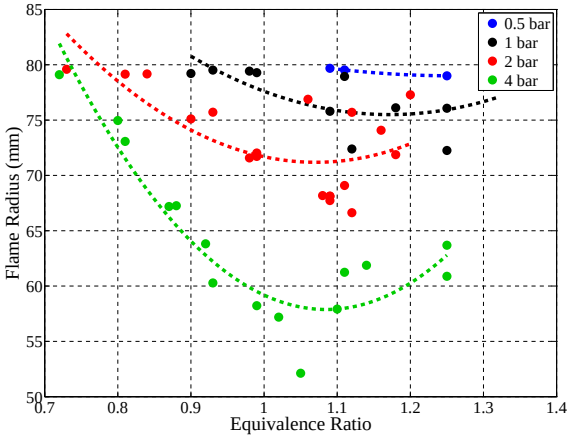

(e) Flame Radius

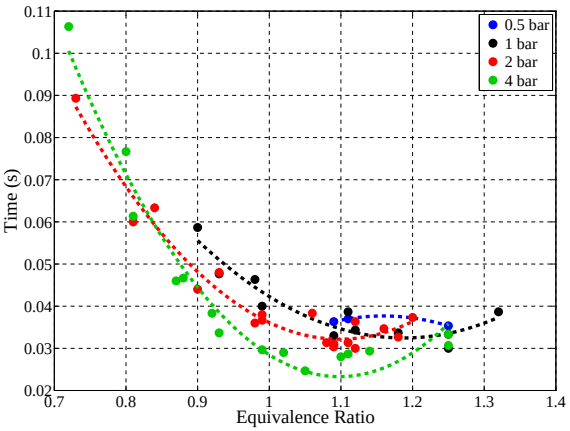

(f) Time

Figure 6.15: Conditions at onset of cellularity against equivalence ratio for different initial pressures, using iso-octane at $T_0 = 380$ K, $x_r = 0$.

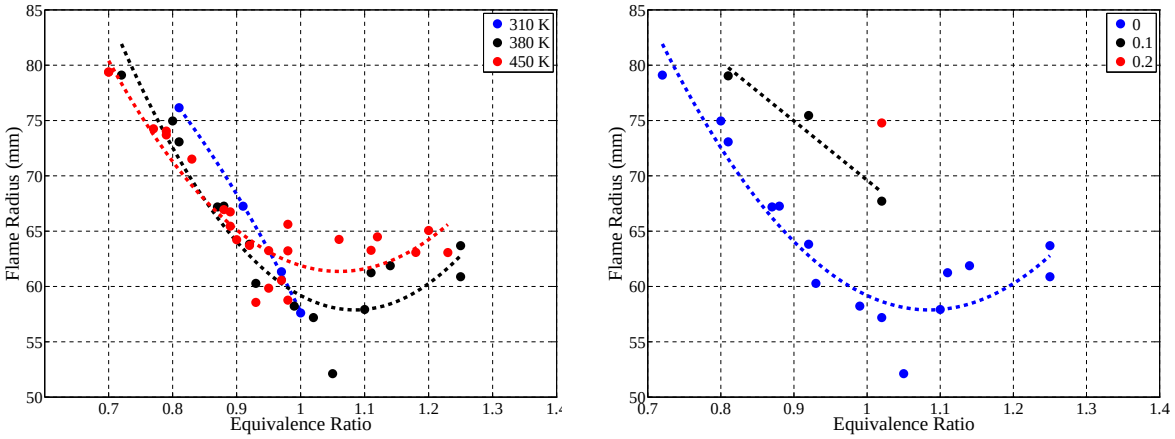

(a) $x_r = 0$, $T_0 = 310$–380 K (b) $T_0 = 380$ K, $x_r = 0$–0.2

Figure 6.16: Flame radius at onset of cellularity against equivalence ratios for different (a) initial temperatures and (b) residual mole fractions for iso-octane at $p_0 = 4$ bar.

mole fraction, particularly for rich mixtures. The equivalence ratio at peak burning velocity decreases with increasing residuals. This would be expected, as increased levels of residuals would lower the flame temperature, leading to less dissociation.

Figure 6.18 shows the only high temperature literature data available. As previously discussed, the results of Farrell et al. (2004) are recognised as being too high, but they do show a similar trend with equivalence ratio to the correlation. The results of Johnston and Farrell (2005) show a similar peak burning velocity to the correlation, but their results peak at stoichiometric.

6.7 n-Heptane

For rich, high pressure experiments, high frequency oscillations were seen on the pressure trace, similar to those observed with iso-octane. Plots of the correlation for the burning velocity of n-heptane are shown in Figure 6.19. The correlation shows a more rounded shape than for the other fuels, without such a distinct peak. The equivalence ratio for maximum burning velocity shifts a lot with pressure.

A comparison of the correlation with the literature data is shown in Figure 6.20. There is reasonable agreement with the results of Smallbone et al. (2009). However, the agreement with Kumar et al. (2007) is poor above $\phi = 0.7$.

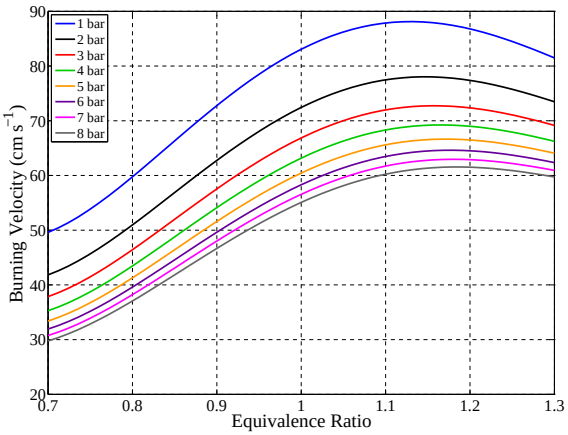

(a) $T_{\mathrm{u}} = 500$ K, $x_{\mathrm{r}} = 0$, $p_{\mathrm{u}} = 1$–8 bar

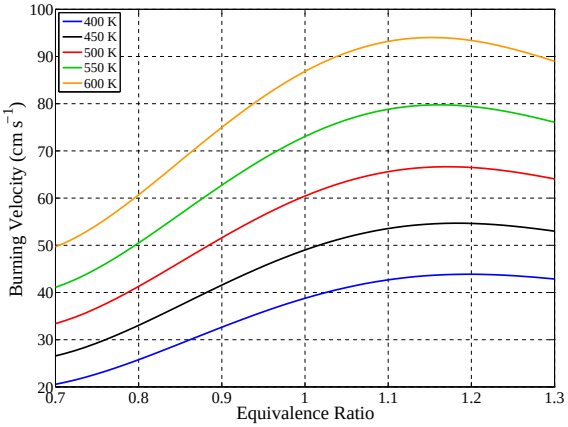

(b) $p_{\mathrm{u}} = 5$ bar, $x_{\mathrm{r}} = 0$, $T_{\mathrm{u}} = 400$-600 K

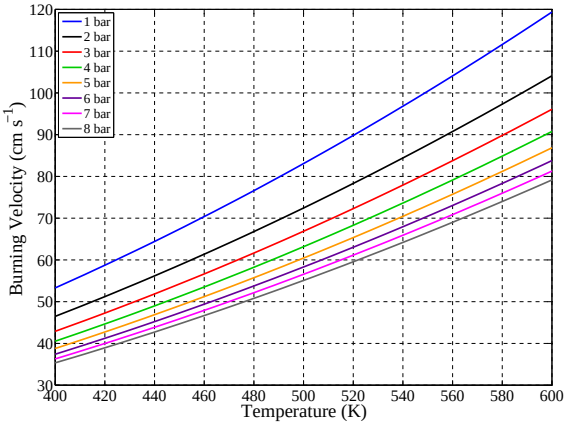

(c) $\phi = 1$, $x_{\mathrm{r}} = 0$, $p_{\mathrm{u}} = 1$–8 bar

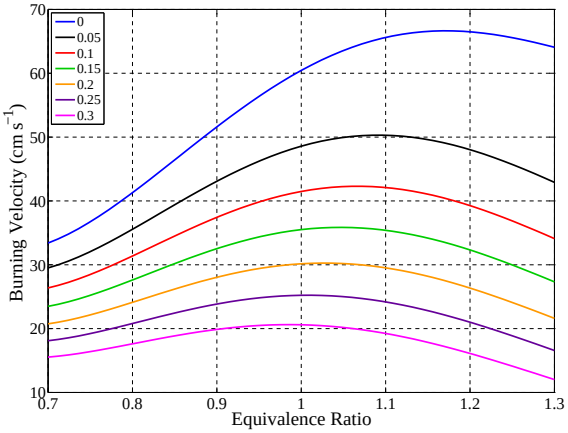

(d) $p_{\mathrm{u}} = 5$ bar, $T_{\mathrm{u}} = 500$ K, $x_{\mathrm{r}} = 0$–0.3

Figure 6.17: Ethylbenzene experimental correlation.

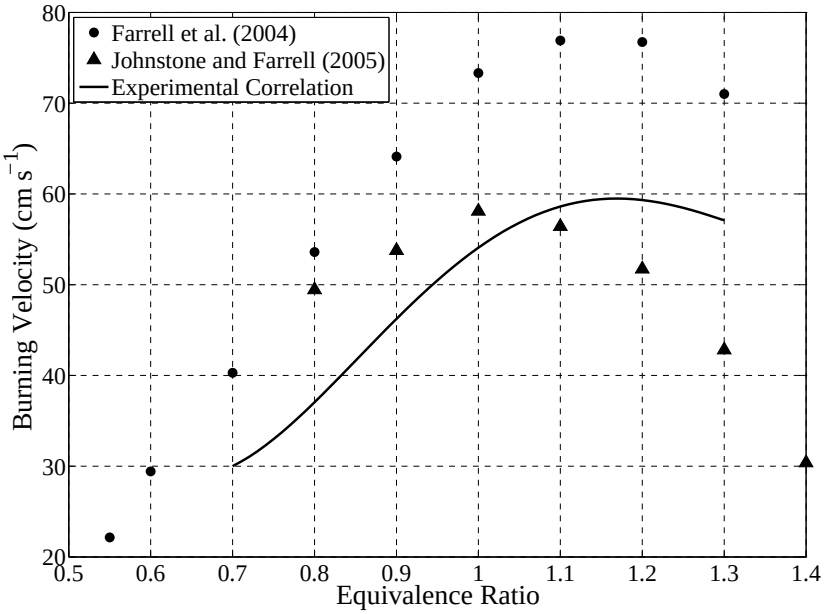

Figure 6.18: Comparison of ethylbenzene experimental correlation and experimental results of Farrell et al. (2004) and Johnston and Farrell (2005) at $p_\mathrm{u} = 3$ atm, $T_\mathrm{u} = 450$ K, $x_\mathrm{r} = 0$.

6.8 Toluene

Plots from the correlation for the burning velocity of toluene are shown in Figure 6.21. These are closer to the expected trends than n-heptane. Although the trends in peak burning velocity are still incorrect (apart from with residual mole fraction, which is correct), the value of the equivalence ratio at peak burning velocity is approximately correct.

Figure 6.22 shows plots of pressure and pressure-derived burning velocities for a single toluene experiment. The attached schlieren images show the growth of the flame and the onset of cellularity, from smooth surface (5 ms) to cracked surface (20 ms) to a fully cellular surface at 24 ms, at which point the automatic cellularity detection algorithm detected cellularity. The cells then split further. It is clear that by the time the flame flame passes out of the viewing diameter of the windows, the pressure rise is still very small.

Similarly to Figure 6.18 for ethylbenzene, Figure 6.23 shows reasonable agreement (particularly for weak mixtures) with Johnston and Farrell (2005), but burning velocities lower than those given by Farrell et al. (2004).

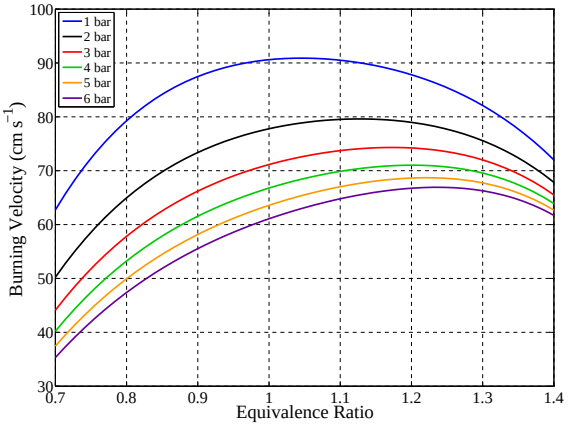

(a) $T_u = 500$ K, $x_r = 0$, $p_u = 1$–6 bar

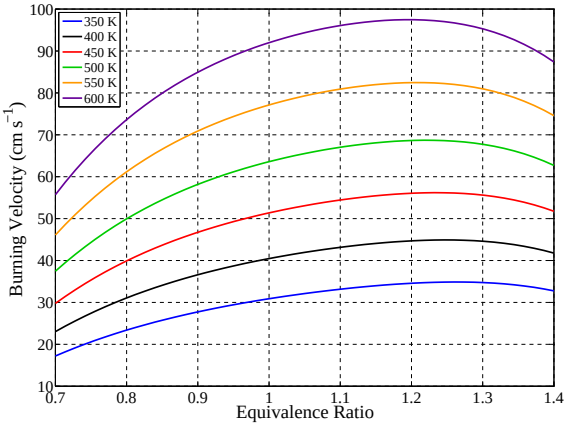

(b) $p_u = 5$ bar, $x_r = 0$, $T_u = 350$–600 K

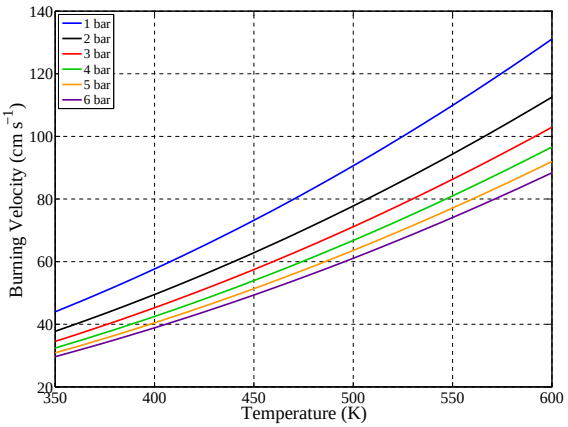

(c) $\phi = 1$, $x_r = 0$, $p_u = 1$–6 bar

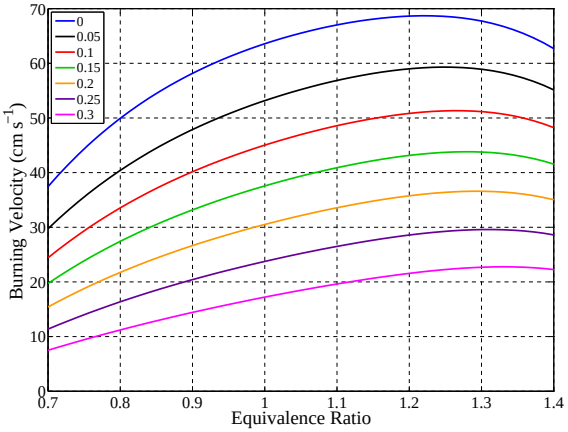

(d) $p_u = 5$ bar, $T_u = 500$ K, $x_r = 0$–0.3

Figure 6.19: n-heptane correlation.

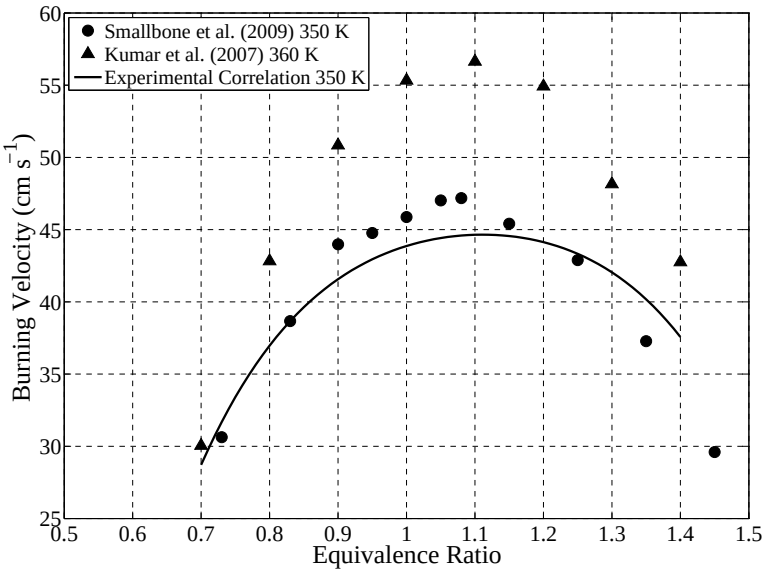

Figure 6.20: Comparison of n-heptane experimental correlation and experimental results of Smallbone et al. (2009) and Kumar et al. (2007) at $p_u = 1$ atm, $T_u \approx 350$ K, $x_r = 0$.

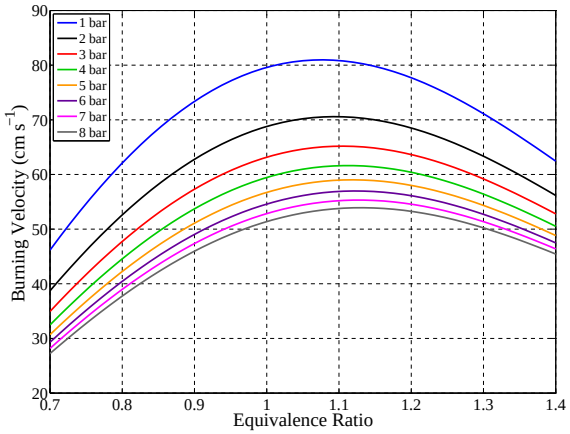

(a) $T_\mathrm{u} = 500$ K, $x_\mathrm{r} = 0$, $p_\mathrm{u} = 1$–8 bar

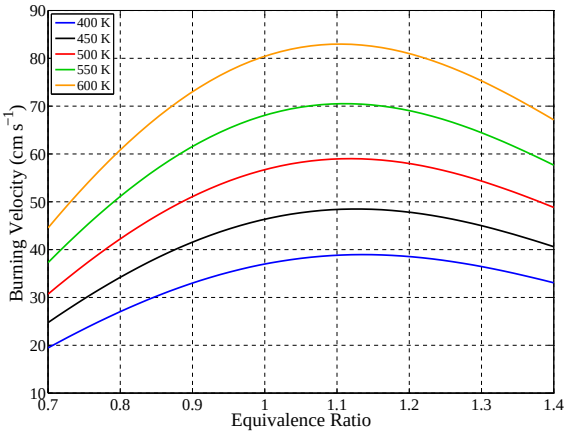

(b) $p_\mathrm{u} = 5$ bar, $x_\mathrm{r} = 0$, $T_\mathrm{u} = 400$–600 K

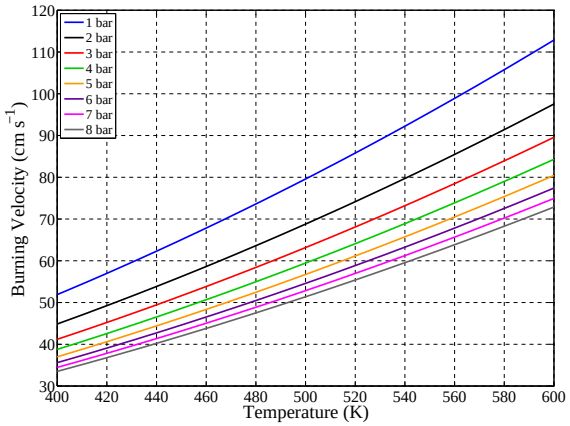

(c) $\phi = 1$, $x_\mathrm{r} = 0$, $p_\mathrm{u} = 1$–8 bar

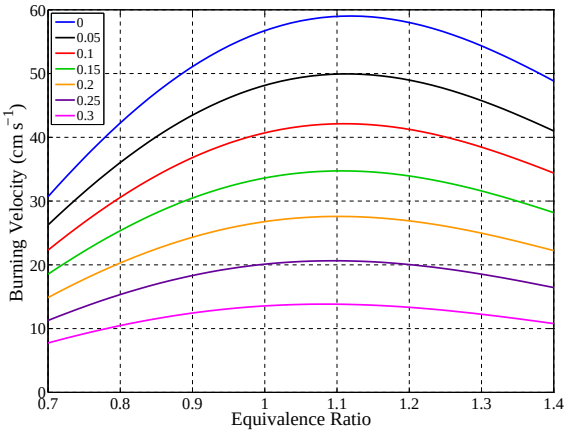

(d) $p_\mathrm{u} = 5$ bar, $T_\mathrm{u} = 500$ K, $x_\mathrm{r} = 0$–0.3

Figure 6.21: Toluene experimental correlation.

Table 6.5: Minimum and maximum conditions in the aromatics data sets.

		Ethylbenzene		Toluene	
Property	Unit	Min	Max	Min	Max
T_0	K	380	450	310	450
p_0	barA	0.5	4.0	0.5	4.0
ϕ	-	0.69	1.52	0.67	1.67
x_r	-	0	0.3	0	0.3
p_u	barA	0.608	10.5	0.675	11.1
T_u	K	397	654	341	657
S_u	cm s^{-1}	5.89	132	12.7	109
S_f	cm s^{-1}	18.9	366	25.5	325
α	s^{-1}	5.19	170	7.08	140
r_b	mm	39.8	78.0	39.5	78.2
t	ms	12.0	206	14.1	132

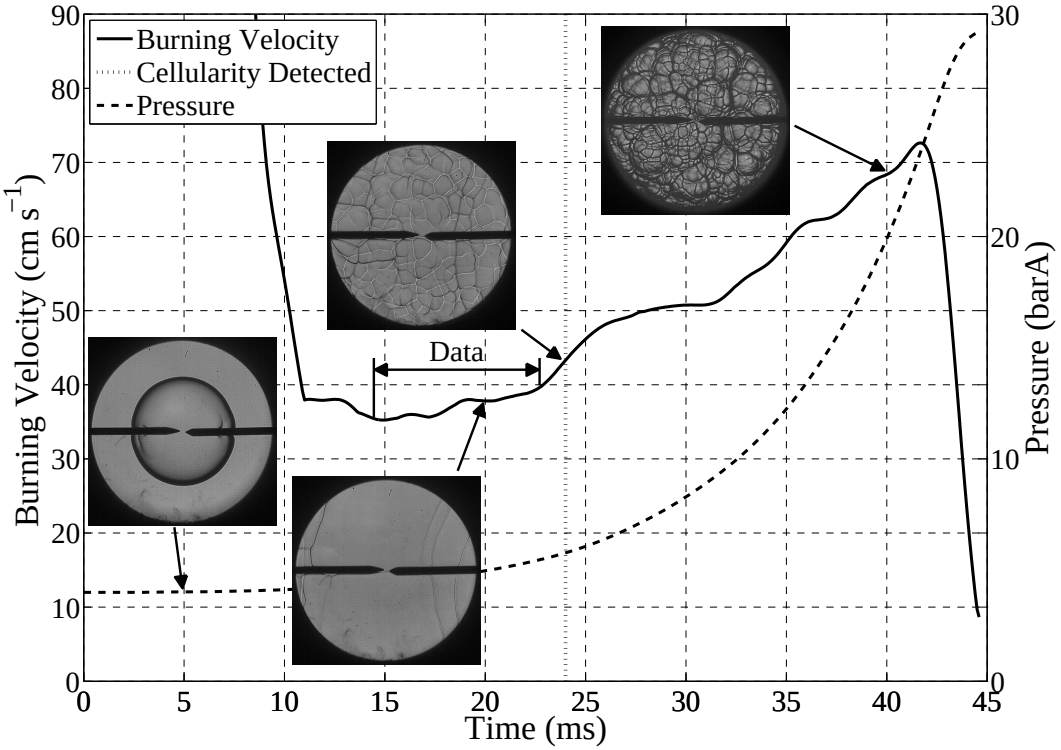

Figure 6.22: Pressure and pressure-derived burning velocity against time for toluene at $\phi = 1.05$, $T_0 = 380$ K, $p_0 = 4$ bar, $x_\mathrm{r} = 0$, with schlieren images showing automatic detection of cellularity. 'Data' arrow shows extent of usable pressure data.

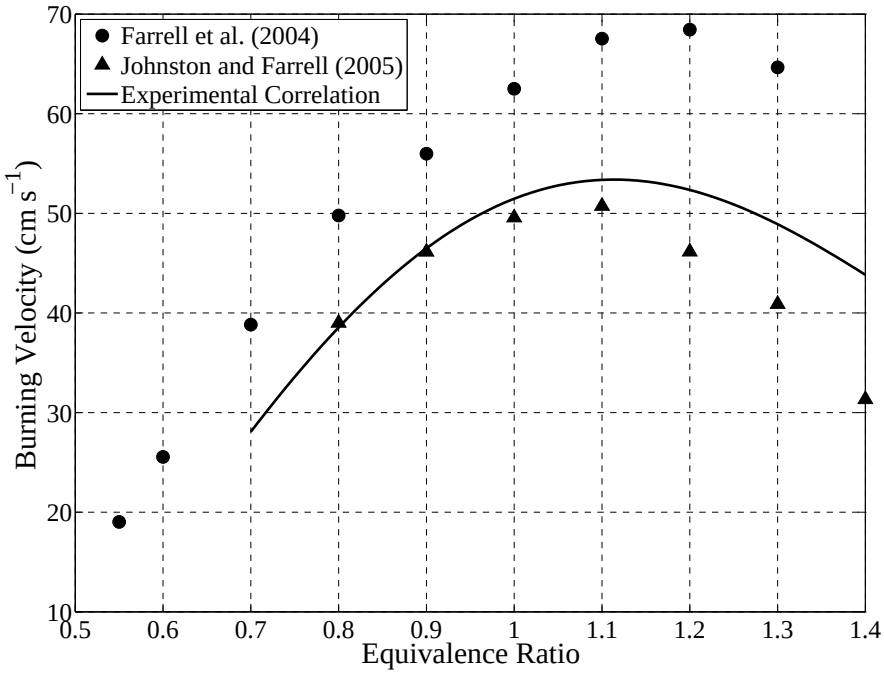

Figure 6.23: Comparison of toluene experimental correlation and experimental results of Farrell et al. (2004) and Johnston and Farrell (2005) at $T_\mathrm{u} = 450$ K, $p_\mathrm{u} = 3$ atm, $x_\mathrm{r} = 0$.

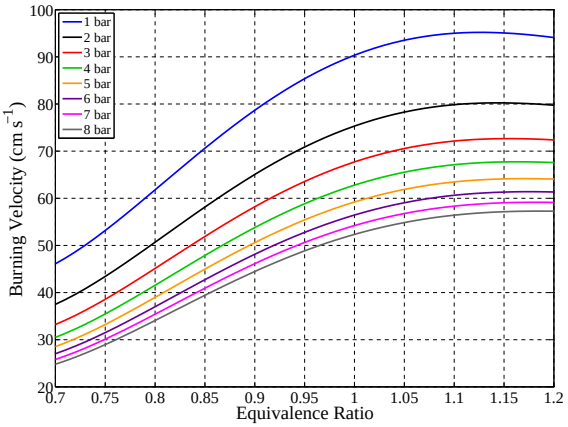

(a) $T_u = 500$ K, $x_r = 0$, $p_u = 1$–8 bar

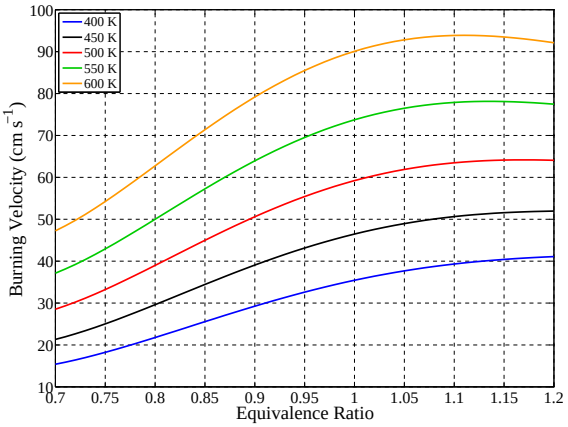

(b) $p_u = 5$ bar, $x_r = 0$, $T_u = 400$-600 K

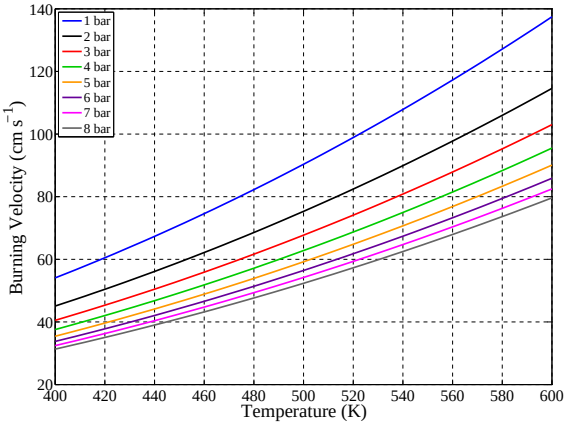

(c) $\phi = 1$, $x_r = 0$, $p_u = 1$–8 bar

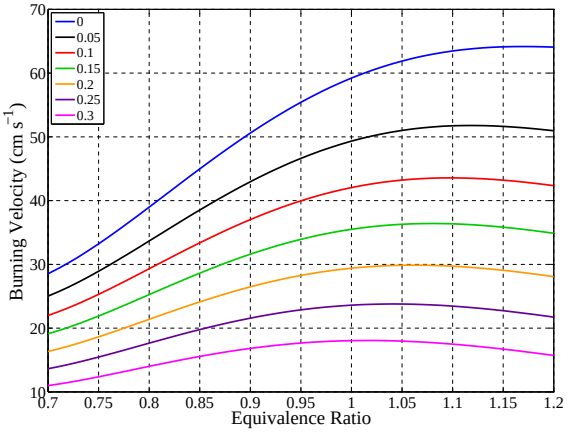

(d) $p_u = 5$ bar, $T_u = 500$ K, $x_r = 0$–0.3

Figure 6.24: Ethanol experimental correlation.

6.9 Ethanol

The ethanol used was kept in a 2.5 litre bottle rather than being decanted into a smaller container so that the effect of water contamination from the atmosphere was minimised.

It is expected that the equivalence ratio at which maximum burning velocity occurs will be higher than for the hydrocarbon fuels, as the oxygen atom in the ethanol molecule will contribute additional oxygen to the reaction at rich equivalence ratios (Egolfopoulos et al., 1992). This attribute can be seen in the plots of the correlation shown in Figure 6.24, but it is not clear whether this is due to this effect, or a problem with the fitting.

Comparisons of the correlation and data from the literature did not show particu-

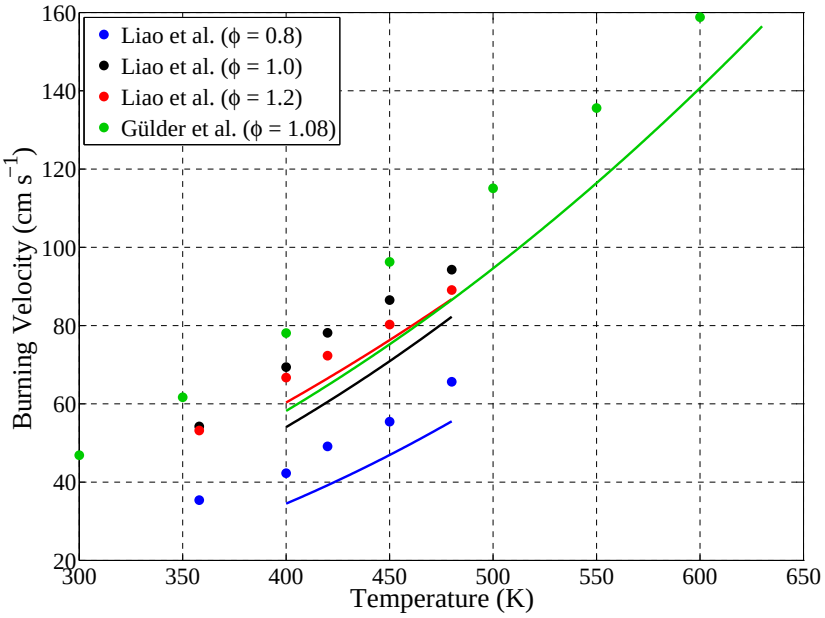

Figure 6.25: Comparison of ethanol experimental correlation at ambient pressure with literature data of Liao et al. (2007) and Gülder (1984).

larly good agreement at ambient temperature (see Figures 6.25 and 6.26), although it should be noted that the results of Gülder (1984) were a lot higher than more modern literature data for iso-octane (see Figure 6.11). Far better agreement for ethanol was found at elevated pressure, compared against the results of Beeckman et al. (2009) (see Figure 6.27).

6.10 Relative Burning Velocities

An important aim of measuring burning velocities is to find which fuels burn the fastest, in order to improve fuel blends. Hence all the fuels tested were compared at the same conditions of $\phi = 1$, $T_u = 450$ K, $p_u = 3$ atm, $x_r = 0$ to compare with the extensive high pressure data set of Farrell et al. (2004). Unfortunately, comparison with other literature results have shown this data set to give very high values of burning velocity (see Figure 6.4). Nevertheless, the order of the burning velocity of the fuels can be compared, and for this purpose Farrell et al. (2004) generally agrees with the low pressure data set of Davis and Law (1998) (see Section 2.5.1).

Figure 6.28 shows the results of Farrell et al. (2004), along with the correlation

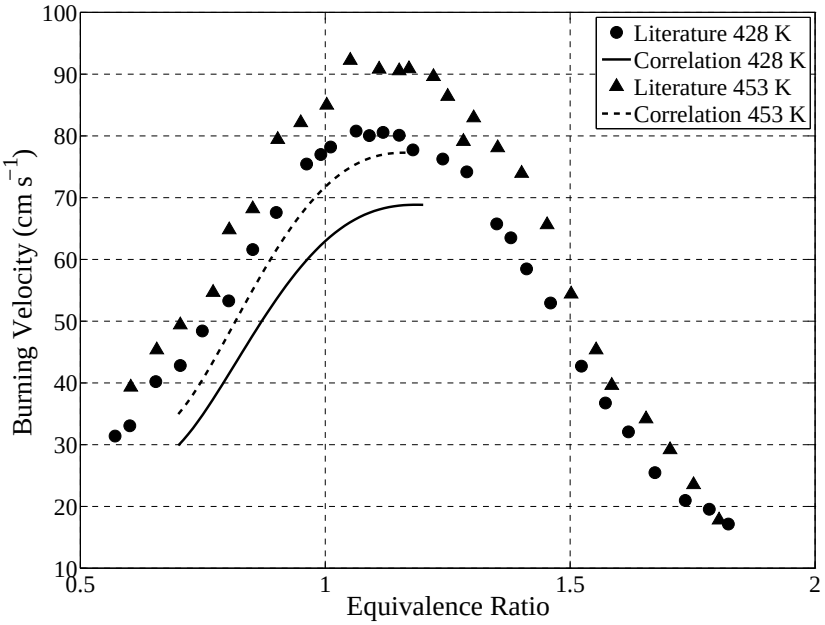

Figure 6.26: Comparison of ethanol experimental correlation and experimental data of Egolfopoulos et al. (1992) at ambient pressure, with no residuals.

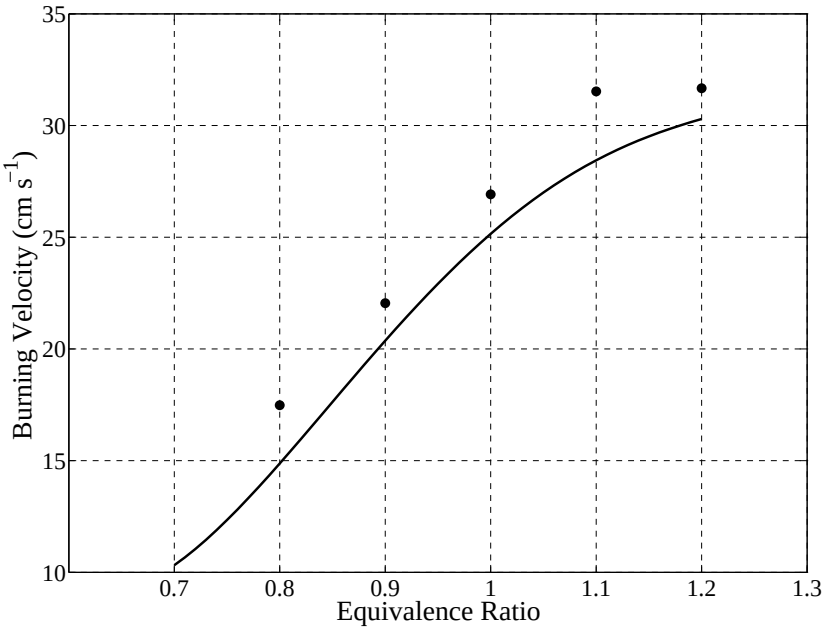

Figure 6.27: Comparison of ethanol experimental correlation with experimental data of Beeckman et al. (2009) at $p_{\mathrm{u}} = 10$ bar, $T_{\mathrm{u}} = 373$ K, $x_{\mathrm{r}} = 0$.

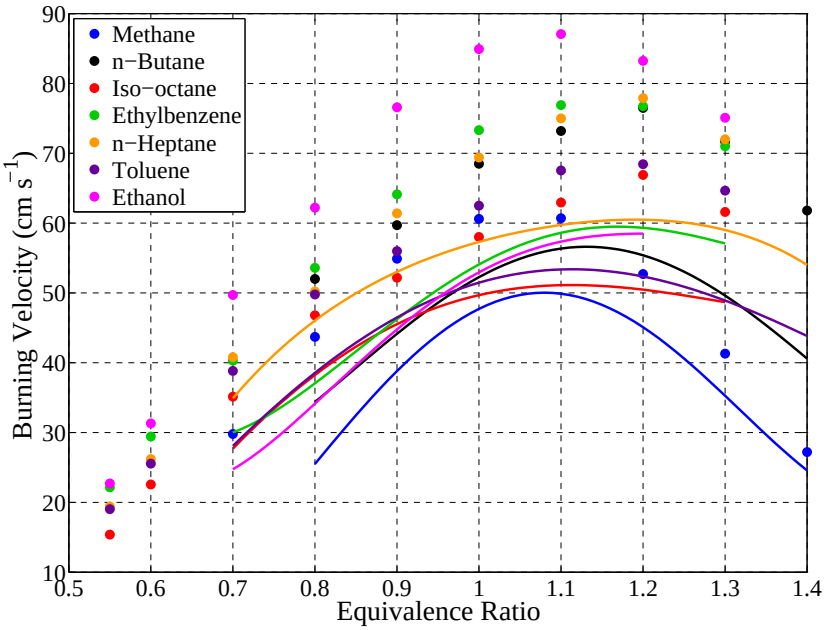

Figure 6.28: Comparison between the pressure-derived results of Farrell et al. (2004) (points) and the correlation from the current study at $T_u = 450$ K, $p_u = 3$ atm, $x_r = 0$.

Table 6.6: Order of burning velocities from the data set of Farrell et al. (2004) and the current correlation, at $\phi = 1.1$, $T_u = 450$ K, $p_u = 3$ atm, $x_r = 0$.

Position	Current Study	Farrell et al. (2004)
Fastest	n-Heptane	Ethanol
	Ethylbenzene	Ethylbenzene
	Ethanol	n-Heptane
	n-Butane	n-Butane
	Toluene	Toluene
	Methane	Iso-octane
Slowest	Iso-octane	Methane

plotted at the same conditions. The order at $\phi = 1.1$ (which should approximately be the peak) for both is given in Table 6.6. Some of the fuels are very close in burning velocity, making slight changes in the order inevitable, but the agreement in order is good, apart from ethanol. Farrell et al. (2004) found that the burning velocity of ethanol exceeded that of the other fuels, but this was not the case for the current correlation.

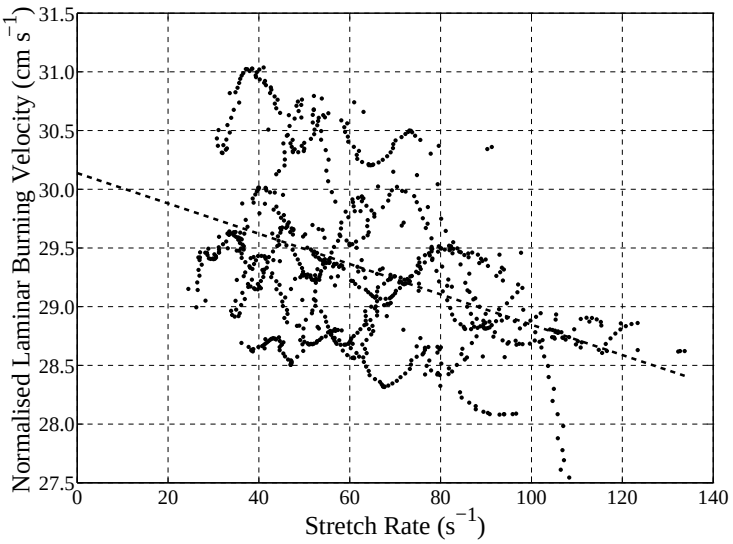

Figure 6.29: Toluene schlieren data normalised to 1 bar, 298 K and extrapolated to zero stretch to give $S_u = 30.1$ cm s^{-1} and $L_b = 0.0129$ cm.

6.11 Unstretched Burning Velocities

Burning velocities for equivalence ratios near to stoichiometric ($0.98 \leq \phi \leq 1.02$) were normalised to standard conditions (298 K, 1 bar), using the values of η_0 and β_0 from the general correlation for that fuel (see Equation 4.33 in Section 4.7.2.5.1). Normalised burning velocity was then plotted against stretch rate to allow linear extrapolation (by least squares fitting) to zero stretch rate to find the unstretched burning velocity and Markstein length (gradient multiplied by minus one). These fits will be rather approximate (see Figure 6.29), as they were in Figure 4.18. For some fuels a small number of points were used for the extrapolation. The values of unstretched burning velocity (S_u) are shown in Table 6.7, along with stretched values from the correlation (S_n) for comparison, and these will be an extrapolation as explained in Section 6.1. Apart from n-heptane, the Markstein lengths are positive, indicating that stretch decreases the burning velocity. Thus it would be expected that the unstretched burning velocities would be higher than the stretched burning velocities, and they are, apart from methane and ethanol.

Table 6.7: Unstretched burning velocities (S_u) and Markstein lengths for near stoichiometric ($0.98 \leq \phi \leq 1.02$) data points normalised to 298 K, 1 bar and stretched burning velocities (S_n) from the correlation.

Fuel	S_n (cm s^{-1})	S_u (cm s^{-1})	L_b (cm)
Methane	30.5	27.5	0.0718
n-Butane	34.1	39.7	0.101
Iso-octane	28.8	30.5	0.0275
Ethylbenzene	29.4	31.4	0.0216
n-Heptane	31.6	33.4	-0.00814
Toluene	29.5	30.1	0.0129
Ethanol	27.5	27.4	0.00161

Table 6.8: Coefficients for parabolic best fit ($S_u = a + bx_{IO} + cx_{IO}^2$) for burning velocities of iso-octane/ethylbenzene mixtures at $\phi = 1$, $T_u = 500$ K, $p_u = 5$ bar, $x_r = 0$.

Coefficient	Volume Fraction	Mole Fraction
a	60.468	60.527
b	-2.4555	-4.7934
c	-5.1906	-2.9664

6.12 Mixtures

Stoichiometric mixtures tests were carried out at two initial temperatures ($T_0 = 380$ K and $T_0 = 450$ K) and the same four initial pressures. No tests with residuals were conducted. Pure components were not re-tested, so their values were found from the previous correlations.

6.12.1 Iso-octane and Ethylbenzene

The volume fractions of iso-octane tested were 12.5%, 25%, 50% and 75%. Density values for the mixtures were found from the model of Davy and Kowsari (2010). Figure 6.30 shows that burning velocity decreases with an increasing volume fraction of iso-octane. Figure 6.31 shows that the burning velocity is non-linear with either volume fraction or mole fraction. A parabola was fitted through the points with fitting residuals of less than 1 cm s^{-1}. The coefficients are shown in Table 6.8. Coefficients for the stoichiometric correlation are given in Table 6.9.

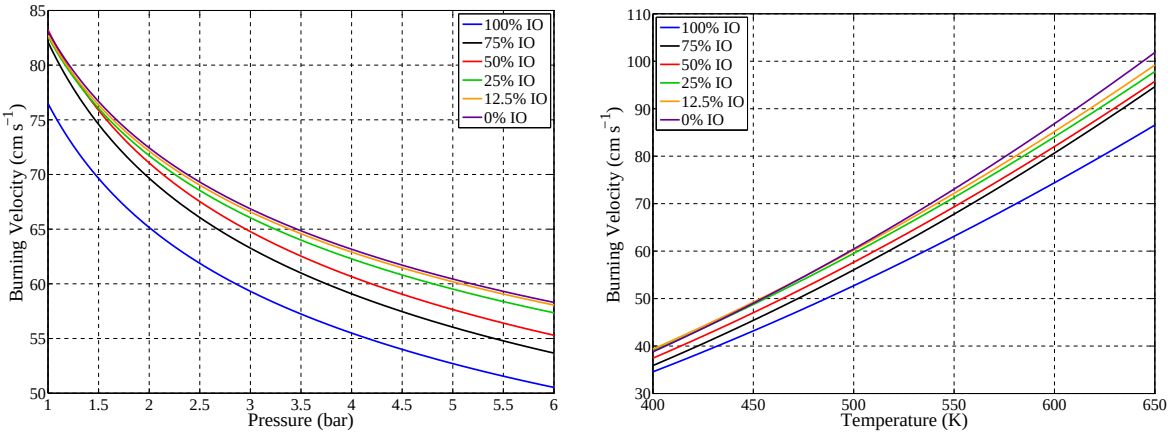

(a) $T_\mathrm{u} = 500$ K (b) $p_\mathrm{u} = 5$ bar

Figure 6.30: Burning velocity of iso-octane/ethylbenzene mixtures at $\phi = 1$, $x_\mathrm{r} = 0$.

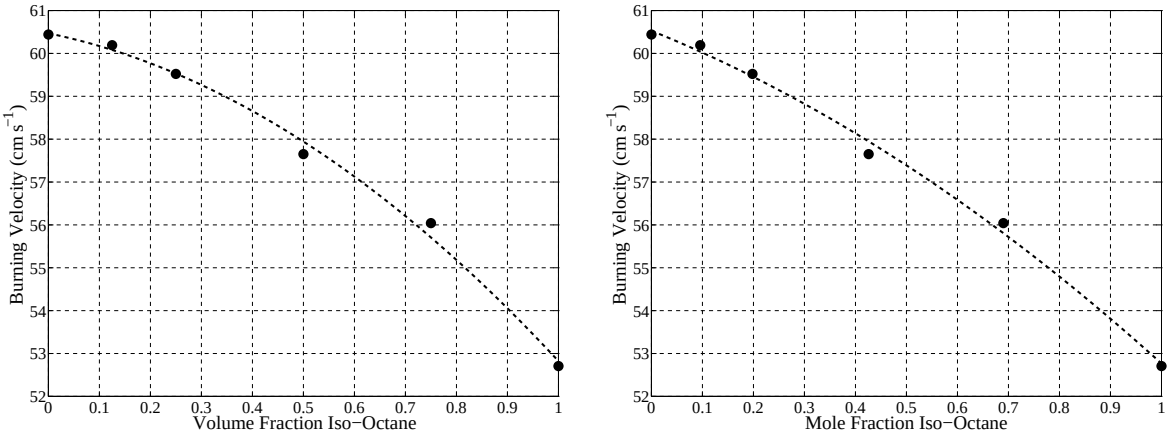

(a) Volume Fraction (b) Mole Fraction

Figure 6.31: Burning velocity of iso-octane/ethylbenzene mixtures at $\phi = 1$, $T_\mathrm{u} = 500$ K, $p_\mathrm{u} = 5$ bar, $x_\mathrm{r} = 0$ against (a) volume fraction and (b) mole fraction.

Table 6.9: Stoichiometric iso-octane/ethylbenzene mixture correlation coefficients.

% Vol. iso-octane	$S_{\mathrm{u},0}$	α_0	β_0
0 (Pure EB)	29.680	1.9887	-0.19758
12.5	30.880	1.9042	-0.19761
25	30.999	1.8937	-0.20356
50	30.591	1.9340	-0.22814
75	29.214	1.9970	-0.23740
100	28.756	1.8905	-0.23142

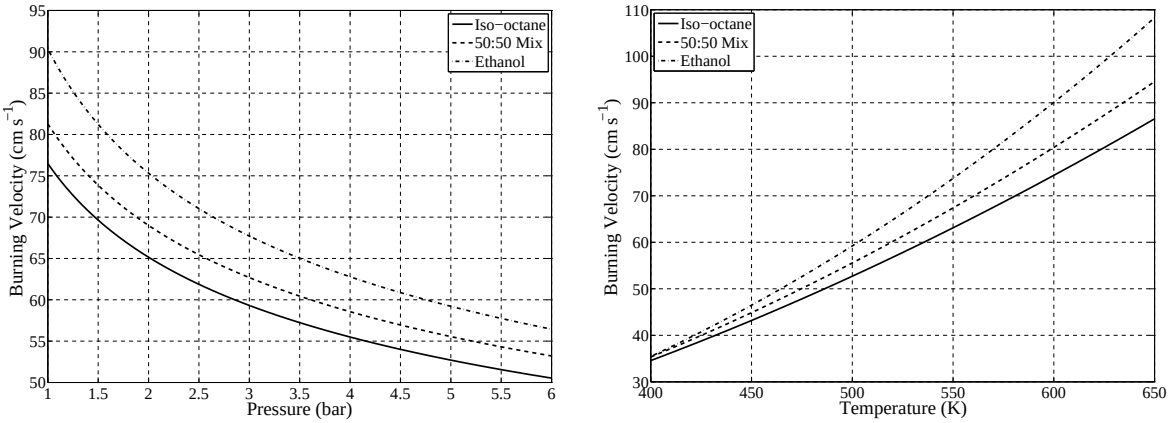

(a) $T_{\mathrm{u}} = 500$ K (b) $p_{\mathrm{u}} = 5$ bar

Figure 6.32: Burning velocity of a 50/50% (by volume) mixture of iso-octane/ethanol at $\phi = 1$, $x_{\mathrm{r}} = 0$ along with the pure components.

Table 6.10: Stoichiometric iso-octane/ethanol mixture correlation coefficients.

% Vol. Iso-octane	$S_{\mathrm{u},0}$	α_0	β_0
0	27.466	2.3009	-0.26254
50	28.479	2.0269	-0.23658
100	28.756	1.8905	-0.23142

6.12.2 Iso-octane and Ethanol

A single mixture of 50% iso-octane, 50% ethanol was tested. Density values for the mixtures were found from interpolations of the experimental data of Ku and Tu (2005).

Figure 6.32 shows that the burning velocity mixture was slightly less than the mean of the two components. Correlation coefficients are given in Table 6.10. Although mixtures of iso-octane and ethanol have been tested by Beeckman et al. (2009) and Gülder (1984), neither tested above 20% ethanol.

6.13 Correlating Burning Velocity with Other Fuel Properties

The wish to develop faster burning fuels has led people to examine the relationship between burning velocity and other fuel properties, to find what causes faster burning

velocities. However, recent studies have started to indicate that the key to burning velocities are the kinetics of the reactions, rather than a property of the fuel. To investigate, burning velocities for each of the seven pure fuels tested were found from the correlation and compared with four other properties of the fuels (see Figure 6.33).

It is known that burning velocity is strongly dependant on temperature. Thus it has been speculated that fuels with higher flame temperatures, or those that release more energy in a standard combustion reaction, would have faster burning velocities. Enthalpies of combustion were found from Goodger (1975). Figure 6.33a shows that enthalpies of combustion per mole of stoichiometric mixture vary very little (apart from ethanol) and hence there are no clear trends.

Adiabatic flame temperatures in air at constant pressure were found at 298 K and 1 bar from the first burned temperature produced by the BOMB program, run with a single zone. This was found to agree well with Gaseq for methane. Figure 6.33b shows that adiabatic flame temperatures of the fuels tested did not vary much, but again there were no clear trends.

Early interest in fuel technology attempted to link burning velocity to octane number. Octane numbers were found from Stone (1999). The fuels tested were of high octane number, except n-heptane, which is the zero reference on the research octane number scale. Figure 6.33c shows that no trends were visible.

Finally, boiling points at standard pressure (found from Poling et al., 2001) were plotted against burning velocity (see Figure 6.33d). Again no clear trend was present.

6.14 Conclusions

Burning velocity decreased slightly at coil energies below 20 mJ. There was no evidence of over-driving of the flame. Although large burning velocities are measured at flame radii less than 10 mm, they do not alter with coil energy. It is possible that they are caused by the high stretch rate, but with Markstein lengths normally positive, this

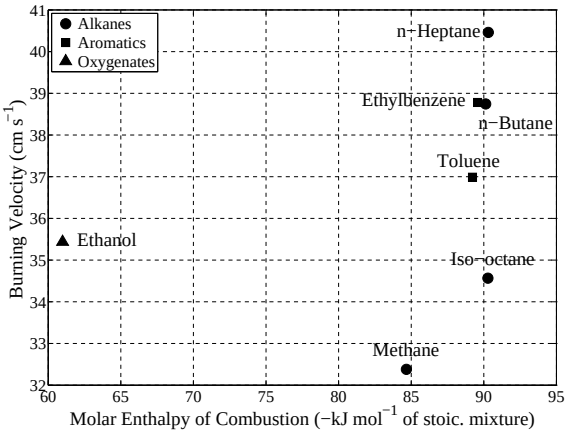

(a) Enthalpy of Combustion

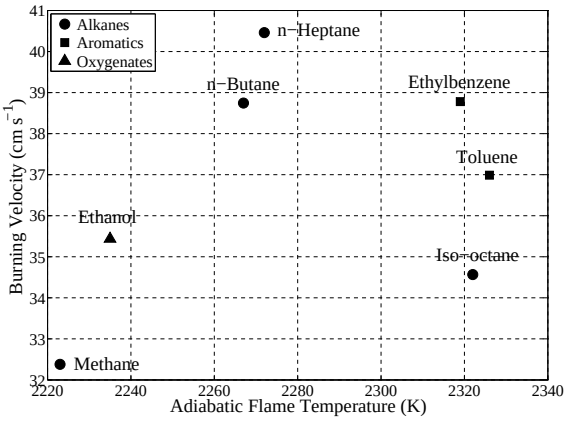

(b) Adiabatic Flame Temperature

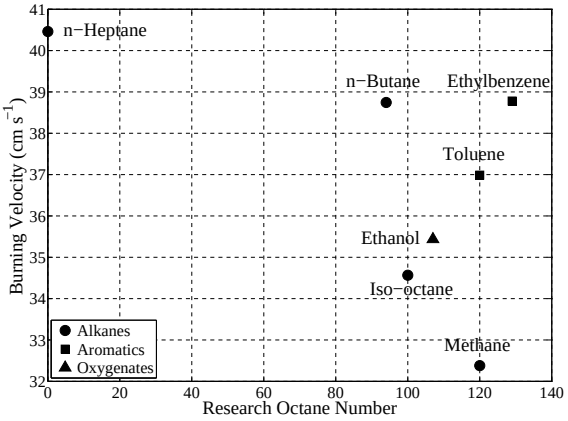

(c) Research Octane Number

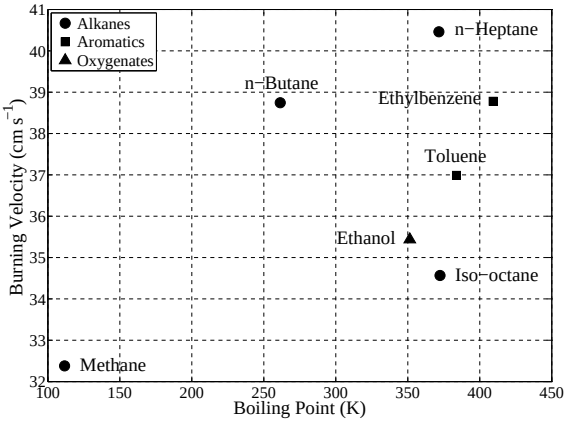

(d) Boiling Point

Figure 6.33: Scatter plots of burning velocities at $\phi = 1$, $T_\mathrm{u} = 400$ K, $p_\mathrm{u} = 5$ bar, $x_\mathrm{r} = 0$ from the correlation against other properties of the fuels.

would be expected to decrease the burning velocity. More probable is that some effect of the ignition or initial combustion does accelerate the flame, but this is not dependent on the spark energy.

Most fuels generally agreed with the literature values, although some literature sources were shown to give very high burning velocities. Agreement was generally better at higher pressures. Some fuels showed unexpected trends in peak burning velocity with equivalence ratio as temperature and pressure were changed, but correct trends for residual mole fraction. n-Heptane was found to be the fastest burning fuel, and iso-octane the slowest. The order showed good agreement with Farrell et al. (2004), with the exception of ethanol, for which the experimental correlation gave lower results than expected.

At the onset of cellularity, some parameters (e.g. flame radius) were found to vary with initial pressure, as others (e.g. pressure) did not change significantly. Only temperature and burning velocity at the onset of cellularity were affected by initial temperature. All the variables were altered by residual level.

Tests with mixtures showed that iso-octane/ethylbenzene mixtures burning velocities had a non-linear dependence on the mixture composition. The addition of a small quantity of ethylbenzene led to a marked increase in burning velocity, but further additions gave diminishing returns.

There was no evidence of any relationships between burning velocities of the fuels tested and the enthalpy of combustion, adiabatic flame temperature, octane number or boiling point.

Table 6.11: Coefficient values to find burning velocities from the correlation (Equation 4.37), within the parameter bounds given by Table 6.2.

Fuel	$S_{u,0}$	$S_{u,1}$	$S_{u,2}$	$S_{u,3}$	$S_{u,4}$	η_0	η_1	β_0	β_1	μ_1	μ_2	μ_3
Methane	30.464	36.396	-221.62	-135.50	575.00	1.9474	1.8150	-0.31829	-0.66153	-	-	-
n-Butane	34.145	42.314	-134.06	-187.03	353.60	1.6202	-0.077368	-0.21780	0.013490	-	-	-
Iso-octane	28.481	13.110	-80.048	56.593	57.734	1.8889	-0.084562	-0.19970	0.10737	2.0808	0.82827	0.021031
Ethylbenzene	29.680	37.460	-91.292	-120.04	323.40	1.9887	-0.62423	-0.19758	0.16047	1.4875	0.67601	-0.57887
n-Heptane	31.763	12.989	-52.453	56.582	-161.18	2.0256	-0.51112	-0.22010	0.33502	1.9899	0.83374	0.25516
Toluene	29.528	20.126	-89.019	1.2224	73.252	1.9159	-0.42356	-0.21046	0.14415	2.2543	0.90195	-0.048952
Ethanol	27.466	46.798	-81.892	-71.437	374.64	2.3009	-1.5482	-0.26254	0.11856	1.8132	0.79607	-0.34009

Chapter 7

Conclusions and Future Work

7.1 Conclusions

Laminar burning velocities are an important fuel parameter, with links to burn duration in internal combustion engines. There is a lack of data at high temperatures and pressures, particularly for liquid fuels. Existing data using some methods may erroneously include cellular data, which causes error.

Burning velocities are affected by many parameters, including fuel, oxidant, pressure, temperature, equivalence ratio, stretch rate and the presence of any diluents. Mixtures of fuels are known to sometimes mix non-linearly (Section 2.5.5).

There are many methods of calculating laminar burning velocities, of which the constant volume vessel is the most versatile, allowing the burning velocity to be measured over a range of pressures and temperatures, due to the isentropic compression of the unburned gas. However, it requires a combustion model to allow calculation of burning velocities from the pressure record in the vessel (Section 2.2.2.3). These were examined in detail. In some circumstances, flames have been observed to have surface instabilities, leading to a rough surface (Section 2.8). This can have implications for measurements which assume a smooth surface.

A spherical combustion vessel with oven has been refurbished and augmented with new systems for fuel injection, ignition, LabView control, data acquisition and high

speed schlieren photography (Chapter 3).

Analysis code has been written to run an existing multi-zone combustion model and use the output to analyse both pressure and schlieren data to calculate burning velocities, stretch rates and conditions at the onset of cellularity (Chapter 4). A correlation for burning velocity in terms of pressure, temperature, equivalence ratio and residual mole fraction was validated using modelling data for methane. The burning velocity data was then fitted to this correlation for each fuel.

For some liquid fuels, problems arose due to unequally distributed experimental data points (Section 5.5). It was thought that these caused bias in the fitting process, leading to poor fits in regions of the parameter space in which data points were sparse. Methods for removing this problem were investigated and concluded by limiting the data sets so as to remove points at high equivalence ratio and pressure before fitting. Many other tests were carried out to ensure accuracy in both hardware and software (Chapter 5).

Experiments were conducted with two gaseous (methane and n-butane) and five liquid pure fuels (iso-octane, ethylbenzene, n-heptane, toluene and ethanol). Burning velocities were calculated from 0.7–17 bar, 310–640 K and equivalence ratios from 0.7–1.4 (Chapter 6). The liquid fuel experiments included the effect of real residuals at mole fractions up to 0.3, as opposed to synthetic residuals employed by previous experimentalists. Stoichiometric mixtures tests were also performed at two initial temperatures and four initial pressures. For mixtures of iso-octane and ethylbenzene, percentage volumes of 12.5, 25, 50 and 75% iso-octane were tested. It was found that the the percentage of iso-octane affect burning velocity non-linearly. For iso-octane/ethanol, a single 50:50 mixture was tested. Finally, burning velocities were correlated with other fuel properties, but no clear relationships were found.

7.2 Future Work

7.2.1 Cellularity

A lot of data recorded at high pressures had to be discarded as it was cellular. This then led to problems evaluating burning velocities at high pressures, and through the fitting process, the lack of data influenced values at lower pressures as well. Unstable burning velocities due to cellularity can become several times larger than laminar burning velocities (Bradley, 2008).

The ratio of flame speeds with instabilities to those without is simply equal to the ratio of their surface areas (Bradley, 2008). Hence if some estimation of the surface area of a cellular flame could be made, burning velocities could be estimated even for cellular conditions. This could involve simultaneous schlieren photography through two orthogonal pairs of windows. If the front and side of the flame can be recorded at the same time, computational geometry may be used to estimate the surface area.

This would also allow comparison with the method of Al-Shahrany et al. (2005), who showed that the ratio of flame speeds with instabilities to those without is also equal to the cube root of the ratio of the largest unstable wave number to the smallest unstable wave number. These wave numbers refer to the size of the cells on the unstable flame surface and were derived from the theory of Bechtold and Matalon (1987). This allowed the prediction of laminar burning velocities from measurements of unstable burning velocities of two inwardly propagating flame kernels in a spherical bomb.

Also of interest would be an estimate of the number of cells on the flame surface. This is difficult due to the overlaid patterns representing cracks on the front and rear surfaces of the sphere. However, these could be differentiated as one creates lighter lines and the other darker lines on the schlieren image.

Data has been presented showing various conditions at the onset of cellularity. Although this data is far from exact, some trends are clear. It may be of interest to fit equations to these points to provide data for engine modellers, as the onset of cellularity in an engine can be important. If estimations of flame thickness were made, then the

Péclet number can be calculated as a ratio of the flame thickness to the flame radius. Critical Péclet numbers have been linked to the onset of cracks and full cellularity (see Section 2.8.4). Calculation of Lewis numbers may also be important.

7.2.2 Window Diameter

The bomb is primarily used to derive burning velocity measurements from the pressure record. However, it also has a high speed schlieren photography system installed. Although this is useful for detecting cellularity, it can also be used for finding pre-pressure burning velocities. This is limited at present, as the small diameter windows mean data cannot be acquired with stretch rates less than 200 s^{-1} (see Section 4.5.1). This could be solved by installing larger windows. However, this would require a new bomb shell, which would be expensive and require a lot of work to design and install.

7.2.3 Sphericity of Flame

Dimples can be seen in the flame surface where it is in contact with the electrodes. If the alignment of the electrodes is known, the distance of these dimples from the centre can be compared with the radius of the flame front to calculate the sphericity of the flame. The electrodes are not actually in the image plane — they appear to be because their projection onto the image plane is barely distorted by perspective.

7.2.4 Following Isentropes

The unburned temperature and pressure in each experiment in the bomb follows an isentrope until conduction to the walls occurs. Burning velocity measurements could be validated by starting a second experiment at an initial temperature and pressure that lay part way along the isentrope of the first experiment. The second experiment should then continue along the same path, but for each temperature-pressure data point, the two experiments would have different stretch rates, allowing investigation of the effect of stretch rate.

Bibliography

Addabbo, R., Bechtold, J. K., and Matalon, M. (2002). Wrinkling of spherically expanding flames. In *Proceedings of the Combustion Institute*, volume 29, pages 1527–1535.

Agnew, J. T. and Graiff, L. B. (1961). The pressure dependence of laminar burning velocity by the spherical bomb method. *Combustion and Flame*, 5:209–219.

Al-Shahrany, A. S., Bradley, D., Lawes, M., and Woolley, R. (2005). Measurement of unstable burning velocities of iso-octane - air mixtures at high pressure and the derivation of laminar burning velocities. In *Proceedings of the Combustion Institute*, volume 30, pages 225–232.

Andrews, G. E. and Bradley, D. (1972a). The burning velocity of methane - air mixtures. *Combustion and Flame*, 19:275–288.

Andrews, G. E. and Bradley, D. (1972b). Determination of burning velocities: A critical review. *Combustion and Flame*, 18(1):133–153.

Atkins, P. W. (1994). *Physical Chemistry*. Oxford University Press.

Aung, K. T., Hassan, M. I., and Faeth, G. M. (1998). Effects of pressure and nitrogen dilution on flame/stretch interactions of laminar premixed $H_2/O_2/N_2$ flames. *Combustion and Flame*, 112(1):1–15.

Babkin, V. S., V'yun, A. V., and Kozachenko, L. S. (1967). Determination of burning velocity from the pressure record in a constant-volume bomb. *Combustion, Explosion, and Shock Waves*, 3(3):362–370.

Battino, R., Rettich, T. R., and Tominaga, T. (1984). The solubility of nitrogen and air in liquids. *Journal of Physical and Chemical Reference Data*, 13(2):563–600.

Baulch, D. L., Bowman, C. T., Cobos, C. J., Cox, R. A., Just, T., Kerr, J. A., Pilling, M. J., Stocker, D., Troe, J., Tsang, W., Walker, R. W., and Warnatz, J. (2005). Evaluated kinetic data for combustion modeling: Supplement II. *Journal of Physical and Chemical Reference Data*, 34(3):757–1398.

Bechtold, J. K. and Matalon, M. (1987). Hydrodynamic and diffusion effects on the stability of spherically expanding flames. *Combustion and Flame*, 67(1):77–90.

Beeckman, J., Röhl, O., and Peters, N. (2009). Experimental and numerical investigation of iso-octane, methanol and ethanol laminar burning velocity at elevated pressure and temperature. SAE Paper No. 2009-01-1774.

Bonatesta, F. and Shayler, P. (2008). Factors influencing the burn rate characteristics of a spark ignition engine with variable valve timing. *Proceedings of the Institution of Mechanical Engineers, Part D: Journal of Automobile Engineering*, 222(11):2147–2158.

Bosschaart, K. J. and de Goey, L. P. H. (2003). Detailed analysis of the heat flux method for measuring burning velocities. *Combustion and Flame*, 132(1-2):170–180.

Bradley, D. (2008). Fundamentals of lean combustion. In Dunn-Rankin, D., editor, *Lean Combustion: Technology and Control*, chapter 2, pages 19–53. Academic Press.

Bradley, D., Cresswell, T. M., and Puttock, J. S. (2001). Flame acceleration due to flame-induced instabilities in large-scale explosions. *Combustion and Flame*, 124(4):551–559.

Bradley, D., Gaskell, P. H., and Gu, X. J. (1996). Burning velocities, Markstein lengths and flame quenching for spherical methane-air flames : A computational study. *Combustion and Flame*, 104:176–198.

Bradley, D., Habika, S. E.-D., and El-Sherif, S. A. (1991). A generalization of laminar burning velocities and volumetric heat release rates. *Combustion and Flame*, 87:336–345.

Bradley, D. and Harper, C. M. (1994). The development of instabilities in laminar explosion flames. *Combustion and Flame*, 99:562–572.

Bradley, D., Hicks, R. A., Lawes, M., Sheppard, C. G. W., and Woolley, R. (1998). The measurement of laminar burning velocities and Markstein numbers for iso-octane-air and iso-octane-n-heptane-air mixtures at elevated temperatures and pressures in an explosion bomb. *Combustion and Flame*, 115:126–144.

Bradley, D., Sheppard, C. G. W., Woolley, R., Greenhalgh, D. A., and Lockett, R. D. (2000). The development and structure of flame instabilities and cellularity at low Markstein numbers in explosions. *Combustion and Flame*, 122:195–209.

Bresenham, J. E. (1965). Algorithm for computer control of a digital plotter. *IBM Systems Journal*, 4(1):25–30.

Castleman, K. R. (1996). *Digital Image Processing*. Prentice Hall.

Chen, Z., Burke, M. P., and Ju, Y. (2009). Effects of Lewis number and ignition energy on the determination of laminar flame speed using propagating spherical flames. In *Proceedings of the Combustion Institute*, volume 32, pages 1253–1260.

Clarke, A. (1994). Measurement of laminar burning velocity of air/fuel/diluent mixtures in zero gravity. DPhil Thesis, University of Oxford.

Conan, H. R. and Linnett, J. W. (1951). Burning velocity determinations. Part V —The use of schlieren photography in determining burning velocities by the burner method. *Transactions of the Faraday Society*, 47:981–988.

Coppens, F. H. V., de Ruyck, J., and Konnov, A. A. (2007). Effects of hydrogen enrichment on adiabatic burning velocity and NO formation in methane + air flames. *Experimental Thermal and Fluid Science*, 31(5):437–444.

Coward, H. F. and Hartwell, F. J. (1932). Studies in the mechanism of flame movement. Part II — the fundamental speed of flame in mixtures of methane and air. *Journal of the Chemical Society*, 1:2676–2684.

Daubert, T. E. and Danner, R. P. (1997). *Physical and Thermodynamic Properties of Pure Chemicals*. Taylor & Francis.

Davis, S. G. and Law, C. K. (1998). Determination of and fuel structure effects on laminar flame speeds of C1 to C8 hydrocarbons. *Combustion Science and Technology*, 140:427–449.

Davy, M. H. and Kowsari, R. (2010). Effect of ethanol content and fuel temperature on the macroscopic spray characteristics of a multi-hole DISI fuel injector. *Fuel*, In Press.

Egolfopoulos, F. N., Cho, P., and Law, C. K. (1989). Laminar flame speeds of methane-air mixtures under reduced and elevated pressures. *Combustion and Flame*, 76:375–391.

Egolfopoulos, F. N., Du, D. X., and Law, C. K. (1992). A study on ethanol oxidation kinetics in laminar premixed flames, flow reactors, and shock tubes. In *Proceedings of the Combustion Institute*, volume 24, pages 833–841.

Elia, M., Ulinski, M., and Metghalchi, M. (2001). Laminar burning velocity of methane-air-diluent mixtures. *Journal of Engineering for Gas Turbines and Power*, 123(1):190–196.

Ellis, O. C. and Wheeler, R. V. (1927). The movement of flame in closed vessels: after-burning. *Journal of the Chemical Society*, 1:310–322.

Farrell, J. T., Johnston, R. J., and Androulakis, I. P. (2004). Molecular structure effects on laminar burning velocities at elevated temperature and pressure. SAE Paper No. 2004-01-2936.

Farrell, J. T., Weissman, W., Johnston, R. J., Nishimura, J., Ueda, T., and Iwashita, Y. (2003). Fuel effects on SIDI efficiency and emissions. SAE Paper No. 2003-01-3186.

Ferguson, C. R. (1986). *Internal Combustion Engines*. John Wiley & Sons.

Fiock, E. F., Marvin, Jr, C. F., Caldwell, F. R., and Roeder, C. H. (1940). Flame speeds and energy considerations for explosions in a spherical bomb. Technical Report NACA-TR-682, National Advisory Committee on Aeronautics.

Freeh, J. E., Kumar, K., Huang, Y., and Sung, C. J. (2004). Laminar flame speeds of preheated iso-octane/air and n-decane/air flames using digital particle image velocimetry. In *40th AIAA/ASME/SAE/ASEE Joint Propulsion Conference and Exhibit*, Fort Lauderdale, Florida. AIAA 2004-3709.

Garforth, A. M. (1976). Unburnt gas density measurement in a spherical combustion bomb by infinite-fringe laser interferometry. *Combustion and Flame*, 26:343–352.

Garforth, A. M. and Rallis, C. J. (1978). Laminar burning velocity of stoichiometric methane-air: pressure and temperature dependence. *Combustion and Flame*, 31:53–68.

Gaydon, A. G. and Wolfhard, H. G. (1960). *Flames - Their Structure, Radiation and Temperature*. Chapman and Hall.

Gibbs, G. J. and Calcote, H. F. (1959). Effect of molecular structure on burning velocity. *Journal of Chemical and Engineering Data*, 4(3):226–237.

Gonzalez, R. C. and Woods, R. E. (1993). *Digital Image Processing*. Addison-Wesley.

Goodger, E. M. (1975). *Hydrocarbon Fuels*. Macmillan, London.

Gouy, M. (1879). Recherches photométriques sur les flammes colorées. *Annales de chimie et de physique*, 18:5–101.

Griffiths, J. F. and Barnard, J. A. (1995). *Flame and Combustion*. Blackie Academic & Professional.

Groff, E. G. (1982). The cellular nature of confined spherical propane-air flames. *Combustion and Flame*, 48:51–62.

Gu, X. J., Haq, M. Z., Lawes, M., and Woolley, R. (2000). Laminar burning velocity and Markstein lengths of methane-air mixtures. *Combustion and Flame*, 121:41–58.

Gülder, O. L. (1983). Laminar burning velocities of methanol, isooctane and isooctane/methanol blends. *Combustion Science and Technology*, 33(1–4):179–192.

Gülder, O. L. (1984). Burning velocities of ethanol-isooctane blends. *Combustion and Flame*, 56(3):261–268.

Harris, M. E., Grumer, J., von Elbe, G., and Lewis, B. (1949). Burning velocities, quenching, and stability data on nonturbulent flames of methane and propane with oxygen and nitrogen: Application of theory of ignition, quenching, and stabilization to flames of propane and air. In *Proceedings of the Combustion Institute*, volume 3, pages 80–89.

Heghes, C. I. (2006). *C1-C4 Hydrocarbon Oxidation Mechanism*. PhD thesis, University of Heidelberg.

Heghes, C., Karbach, V., and Warnatz, J. (2005). Evaluation of new data for hydrocarbon kinetics. In *Proceedings of the European Combustion Meeting*, volume 2, Louvain-la-Neuve, Belgium.

Heywood, J. B. (1988). *Internal Combustion Engine Fundamentals*. McGraw Hill.

Hirasawa, T., Sung, C. J., Joshi, A., Yang, Z., Wang, H., and Law, C. K. (2002). Determination of laminar flame speeds using digital particle image velocimetry: Binary fuel blends of ethylene, n-butane, and toluene. In *Proceedings of the Combustion Institute*, volume 29, pages 1427–1434.

Holder, D. W. and North, R. J. (1963). *Schlieren Methods*. Number 31 in Notes on Applied Science. Her Majesty's Stationery Office.

Hopkinson, B. (1906). Explosions of coal-gas and air. *Proceedings of the Royal Society of London. Series A, Containing Papers of a Mathematical and Physical Character*, 77(518):387–413.

Hough, P. V. C. (1962). Method and means for recognizing complex patterns. US Patent No. 3,069,654.

Iijima, T. and Takeno, T. (1986). Effects of temperature and pressure on burning velocity. *Combustion and Flame*, 65(1):35–43.

Illingworth, J. and Kittler, J. (1988). A survey of the Hough transform. *Computer Vision, Graphics and Image Processing*, 44:87–116.

Jerzembeck, S., Sharma, A., and Peters, N. (2008). Laminar burning velocities of nitrogen diluted standard gasoline-air mixture. SAE Paper No. 2008-01-1075.

Johnston, R. J. and Farrell, J. T. (2005). Laminar burning velocities and Markstein lengths of aromatics at elevated temperature and pressure. In *Proceedings of the Combustion Institute*, volume 30, pages 217–224.

Kadowaki, S. (2001). The body-force effect on the cell formation of premixed flames. *Combustion and Flame*, 124(3):409–421.

Kadowaki, S. (2005). The effects of heat loss on the burning velocity of cellular premixed flames generated by hydrodynamic and diffusive-thermal instabilities. *Combustion and Flame*, 143(3):174–182.

Karlin, V. and Sivashinksy, G. (2007). Asymptotic modelling of self-acceleration of spherical flames. In *Proceedings of the Combustion Institute*, volume 31, pages 1023–1030.

Karlovitz, B., Denniston, Jr, D. W., Knapschaefer, D. H., and Wells, F. E. (1953). Studies on turbulent flames. In *Proceedings of the Combustion Institute*, volume 4, pages 613–620.

Kelley, A. P. and Law, C. K. (2007). Nonlinear effects in the experimental determination of laminar flame properties from stretched flames. In *Meeting of the Eastern States Section of the Combustion Institute*, University of Virginia.

Kitagawa, T., Ogawa, T., and Nagano, Y. (2004). The effects of pressure on unstretched laminar burning velocity, Markstein length and cellularity of spherically propagating laminar flames. In *The 6th International Symposium on Diagnostics and Modeling of Combustion in Internal Combustion Engines*, volume 6, pages 575–582.

Kretschmer, C. B., Nowakowska, J., and Wiebe, R. (1946). Solubility of oxygen and nitrogen in organic solvents from -25 to 50°C. *Industrial and Engineering Chemistry*, 38(5):506–509.

Ku, H.-C. and Tu, C.-H. (2005). Densities and viscosities of binary and ternary mixtures of ethanol, 2-butanone, and 2,2,4-trimethylpentane at T = (298.15, 308.15, and 318.15) K. *Journal of Chemical and Engineering Data*, 50(2):608–615.

Kumar, K., Freeh, J., Sung, C., and Huang, Y. (2007). Laminar flame speeds of preheated iso-octane/O_2/N_2 and n-heptane/O_2/N_2 mixtures. *Journal of Propulsion and Power*, 23:428–436.

Kwon, O. C., Rozenchan, G., and Law, C. K. (2002). Cellular instabilities and self-acceleration of outwardly propagating spherical flames. In *Proceedings of the Combustion Institute*, volume 29, pages 1775–1783.

Landau, L. (1944). On the theory of slow combustion. *Acta Physiochimica U.R.S.S.*, 19(1):77–85.

Law, C. K. (2006). *Combustion Physics*. Cambridge University Press.

Lawes, M., Ormsby, M. P., Sheppard, C. G. W., and Woolley, R. (2005). Variation of turbulent burning rate of methane, methanol, amd iso-octane air mixtures with equivalence ratio at elevated pressure. *Combustion Science and Technology*, 177(7):1273–1289.

Lewis, B. and von Elbe, G. (1934). Determination of the speed of flames and the temperature distribution in a spherical bomb from time-pressure explosion records. *Journal of Chemical Physics*, 2:283–290.

Lewis, B. and von Elbe, G. (1943). Stability and structure of burner flames. *Journal of Chemical Physics*, 11(2):75–97.

Lewis, B. and von Elbe, G. (1961). *Combustion, Flames and Explosions of Gases*. Academic Press Inc., London, UK.

Liao, S. Y., Jiang, D. M., Gao, J., and Huang, Z. H. (2004). Measurements of Markstein numbers and laminar burning velocities for natural gas-air mixtures. *Energy & Fuels*, 18(2):316–326.

Liao, S. Y., Jiang, D. M., Gao, J., and Huang, Z. H. (2005). Measurements of Markstein numbers and laminar burning velocities for natural gas-air mixtures. *Energy & Fuels*, 19(1):328.

Liao, S. Y., Jiang, D. M., Huang, Z. H., Zeng, K., and Cheng, Q. (2007). Determination of the laminar burning velocities for mixtures of ethanol and air at elevated temperatures. *Applied Thermal Engineering*, 27(2–3):374–380.

Lindström, F., Ångström, H.-E., Kalghatgi, G., and Möller, C. A. (2005). An empirical SI combustion model using laminar burning velocity correlations. SAE Paper No. 2005-01-2106.

Linnett, J. W. (1953). Methods of measuring burning velocities. In *Proceedings of the Combustion Institute*, volume 4, pages 20–35.

Low, A. (1991). *Introductory Computer Vision and Image Processing*. McGraw-Hill.

Luijten, C. C. M. and de Goey, L. P. H. (2007). New, accurate, analytical relations for fractional pressure rise, laminar burning velocity, and the cubic root law in constant volume combustion. In *Proceedings of the European Combustion Meeting*, volume 3.

Luijten, C. C. M., Doosje, E., and de Goey, L. P. H. (2009). Accurate analytical models for fractional pressure rise in constant volume combustion. *International Journal of Thermal Sciences*, 48(6):1213–1222.

Mallard, E. and Le Chatelier, A. (1883). Combustion des mélanges gazeux explosifs. *Annales des Mines*, 4(8):274–381.

Mandilas, C., Ormsby, M. P., Sheppard, C. G. W., and Woolley, R. (2007). Effects of hydrogen addition on laminar and turbulent premixed methane and iso-octane – air flames. In *Proceedings of the Combustion Institute*, volume 31, pages 1443–1450.

Markstein, G. H. (1964). *Nonsteady Flame Propagation*. Pergamon.

Matalon, M., Cui, C., and Bechtold, J. K. (2003). Hydrodynamic theory of premixed flames: effects of stoichiometry, variable transport coefficients and arbitrary reaction orders. *Journal of Fluid Mechanics*, 487:179–210.

Metghalchi, M. and Keck, J. C. (1982). Burning velocities of mixtures of air with methanol, isooctane and indolene at high pressures and temperatures. *Combustion and Flame*, 48:191–210.

Michelson, D. M. and Sivashinsky, G. I. (1982). Thermal-expansion induced cellular flames. *Combustion and Flame*, 48:211–217.

Michelson, W. (1889). Ueber die normale entzündungsgeschwindigkeit explosiver gasgemische. *Annalen der Physik und Chemie*, 37(5):1–24.

Morley, C. (2005). Gaseq - a chemical equilibrium program for Windows. http://www.gaseq.co.uk/.

Otsu, N. (1979). A threshold selection method from gray-level histograms. *IEEE Transactions on Systems, Man and Cybernetics*, 9(1):62–66.

Payman, W. and Wheeler, R. V. (1922). The combustion of complex gaseous mixtures. *Journal of the Chemical Society. Transactions*, 121(1):363–379.

Poling, B. E., Prausnitz, J. M., and O'Connell, J. P. (2001). *The Properties of Gases and Liquids*. McGraw-Hill, 5 edition.

Powling, J. (1949). A new burner method for the determination of low burning velocities and limits of inflammability. *Fuel*, 28(2):25–29.

Rahim, F., Ulinksi, M., and Metghalchi, M. (2002). Burning velocity measurements of methane-oxygen-argon mixtures and an application to extend methane-air burning velocity measurements. *International Journal of Engine Research*, 3(2):81–92.

Raine, R. R., Stone, C. R., and Gould, J. (1995). Modeling of nitric oxide formation in spark ignition engines with a multizone burned gas. *Combustion and Flame*, 102:241–255.

Rallis, C. J. and Garforth, A. M. (1980). The determination of laminar burning velocity. *Progress in Energy and Combustion Science*, 6:303–329.

Rasmussen, C. E. and Williams, C. K. I. (2006). *Gaussian processes for machine learning*. MIT Press.

Reid, R. C., Prausnitz, J. M., and Poling, B. C. (1987). *The Properties of Gases and Liquids*. Mc-Graw Hill Book Company, 4th edition.

Reynolds, W. C. (1986). The element potential method for chemical equilibrium analysis: Implementation in the interactive program STANJAN. Technical report, Department of Mechanical Engineering, Stanford University.

Rozenchan, G., Zhu, D. L., Law, C. K., and Tse, S. D. (2002). Outward propagation, burning velocities, and chemical effects of methane flames up to 60 atm. In *Proceedings of the Combustion Institute*, volume 29, pages 1461–1469.

Ryan, T. W. and Lestz, S. S. (1980). The laminar burning velocity of isooctane, n-heptane, methanol, methane, and propane at elevated temperature and pressures in the presence of a diluent. SAE Paper No. 800103.

Saeed, K. (2002). Laminar burning velocity measurements. (2002) DPhil Thesis, University of Oxford.

Saeed, K. and Stone, C. R. (2004). The modelling of premixed laminar combustion in a closed vessel. *Combustion Theory and Modelling*, 8:721–743.

Settles, G. S. (2001). *Schlieren and Shadowgraph Techniques*. Springer.

Sharma, S. P., Agrawal, D. D., and Gupta, C. P. (1981). The pressure and temperature dependence of burning velocity in a spherical combustion bomb. In *Proceedings of the Combustion Institute*, volume 18, pages 493–501.

Singer, J. M. (1953). Burning-velocity measurements on slot burners; comparison with cylindrical burner determinations. In *Proceedings of the Combustion Institute*, volume 4, pages 352–358.

Sivashinsky, G. I. (2002). Some developments in premixed combustion modeling. In *Proceedings of the Combustion Institute*, volume 29, pages 1737–1761.

Smallbone, A. J., Liu, W., Law, C. K., You, X. Q., and Wang, H. (2009). Experimental and modeling study of laminar flame speed and non-premixed counterflow ignition of n-heptane. In *Proceedings of the Combustion Institute*, volume 32, pages 1245–1252.

Smith, F. A. and Pickering, S. F. (1928). Bunsen flames of unusual structure. *Industrial and Engineering Chemistry*, 20(10):1012–1013.

Sobel, I. and Feldman, G. (1968). A 3×3 isotropic gradient operator for image processing. Presented at a talk at the Stanford Artificial Project in 1968. Often cited, orig. in Duda, R. and Hart, P. (1973) "Pattern Classification and Scene Analysis", John Wiley and Sons, pp271–2.

Spalding, D. B. (1956). A mixing rule for laminar flame speed. *Fuel*, 35:347–351.

Stevens, F. W. (1926). The rate of flame propagation in gaseous explosive reactions. *Journal of the American Chemical Society*, 48(7):1896–1906.

Stone, R. (1999). *Introduction to Internal Combustion Engines*. Palgrave, 3rd edition.

Strahle, W. C. (1993). *An Introduction to Combustion*. Gordon and Breach Science Publishers.

Taylor, S. (2008). Radius detection of a spherical flame observed with schlieren photography. EPSRC summer placement report, University of Oxford.

Tse, S. D., Zhu, D., and Law, C. K. (2004). Optically accessible high-pressure combustion apparatus. *Review of Scientific Instruments*, 75(1):233–239.

Tse, S. D., Zhu, D. L., and Law, C. K. (2000). Morphology and burning rates of expanding spherical flames in H_2/O_2/inert mixtures up to 60 atmospheres. In *Proceedings of the Combustion Institute*, volume 28, pages 1793–1800.

Turns, S. R. (1996). *An Introduction to Combustion*. McGraw-Hill.

Vagelopoulos, C. M. and Egolfopoulos, F. N. (1998). Direct experimental determination of laminar flame speeds. In *Proceedings of the Combustion Institute*, volume 27, pages 513–519.

Verhelst, S., Woolley, R., Lawes, M., and Sierens, R. (2005). Laminar and unstable burning velocities and Markstein lengths of hydrogen-air mixtures at engine-like conditions. In *Proceedings of the Combustion Institute*, volume 30, pages 209–216.

Warnatz, J. (1978a). Calculation of the structure of laminar flat flames I: Flame velocity of freely propagating ozone decomposition flames. *Berichte der Bunsen-Gesellschaft für Physikalische Chemie*, 82(2):193–200.

Warnatz, J. (1978b). Calculation of the structure of laminar flat flames II: Flame velocity and structure of freely propagating hydrogen-oxygen and hydrogen-fluorine flames. *Berichte der Bunsen-Gesellschaft für Physikalische Chemie*, 82(6):643–649.

Warnatz, J. (1978c). Calculation of the structure of laminar flat flames III: Structure of burner-stabilised hydrogen-oxygen and hydrogen-fluorine flames. *Berichte der Bunsen-Gesellschaft für Physikalische Chemie*, 82(8):834–841.

Wu, C. K. and Law, C. K. (1984). On the determination of laminar flame speeds from stretched flames. In *Proceedings of the Combustion Institute*, volume 20, pages 1941–1949.

Yuan, J., Ju, Y., and Law, C. K. (2006). Pulsating and hydrodynamic instabilities at large Lewis numbers. *Combustion and Flame*, 144:386–397.

Yumlu, V. S. (1967). Prediction of burning velocities of carbon monoxide - hydrogen - air flames. *Combustion and Flame*, 11(3):190–194.

Yumlu, V. S. (1968). The effects of additives on the burning velocities of flames and their possible prediction by a mixing rule. *Combustion and Flame*, 12(1):14–18.

Appendix A

Fuel Properties

Various fuel properties are required by the LabView program or the thermodynamic input file for the BOMB program. These are given in the following tables.

A.1 General Data

The molar mass is required to calculate gravimetric calorific values for the BOMB program (see Section 4.3.1.1). The numbers of C, H and O atoms are required by the LabView program and the BOMB program. These are both given in Table A.1.

Table A.1: General properties of the fuels tested.

Fuel	Formula	M (kg kmol^{-1})
Methane	CH_4	16.043
Butane	C_4H_{10}	58.124
n-Heptane	C_7H_{16}	100.204
Iso-octane	C_8H_{18}	114.231
Toluene	C_7H_8	92.141
Ethylbenzene	C_8H_{10}	106.167
Ethanol	C_2H_5OH	46.069

Table A.2: Coefficients for an equation of liquid density for varying temperature from Daubert and Danner (1997), given in Equation (3.58).

Fuel	A	B	C	D
n-Heptane	6.1259E-01	2.6211E-01	5.4020E+02	2.8141E-01
Iso-octane	5.8860E-01	2.7373E-01	5.4396E+02	2.8460E-01
Toluene	8.7920E-01	2.7136E-01	5.9175E+02	2.9241E-01
Ethylbenzene	7.0041E-01	2.6162E-01	6.1715E+02	2.8454E-01
Ethanol	1.6480E+00	2.7627E-01	5.1392E+02	2.3310E-01

A.2 Liquid Density

The liquid density Y is required to determine the volume of fuel to be injected. It is defined as (see Equation (3.54)):

$$\begin{aligned} Y &= \frac{n}{V} \\ &= \frac{\rho}{M} \end{aligned}$$

An equation for liquid density with varying temperature is given by Daubert and Danner (1997):

$$Y = \frac{A}{B^{\left(1+\left(1-\frac{T}{C}\right)^{D}\right)}}$$

The coefficients are given in Table A.2. For a temperature in Kelvin this gives the liquid density in units of kmol m^{-3}.

A.3 Specific Heat Capacity

The specific heat is required for the BOMB program (see Section 4.3.1.1). This is found from a cubic equation in Reid et al. (1987) and the coefficients given in Table A.3.

$$c_{\mathrm{p}} = A + BT + CT^2 + DT^3 \tag{A.1}$$

For a temperature in Kelvin this gives the specific heat capacity in J mol^{-1} K^{-1}.

Table A.3: Coefficients for Equation (A.1) for specific heat capacity with varying temperature from Reid et al. (1987).

Fuel	A	B	C	D
Methane	1.925E+01	5.213E-02	1.197E-05	-1.132E-08
n-Butane	9.487E+00	3.313E-01	-1.108E-04	-2.822E-09
n-Heptane	-5.146E+00	6.762E-01	-3.651E-04	7.658E-08
Iso-octane	-7.461E+00	7.779E-01	-4.287E-04	9.173E-08
Toluene	-2.435E+01	5.125E-01	-2.765E-04	4.911E-08
Ethylbenzene	-4.310E+01	7.072E-01	-4.811E-04	1.301E-07
Ethanol	9.014E+00	2.141E-01	-8.390E-05	1.373E-09

Table A.4: Coefficients for an equation of vapour pressure for varying temperature from Reid et al. (1987).

Fuel	T_c (K)	p_c (bar)	A	B	C	D
Methane	190.4	46.0	-6.00435	1.18850	-0.83408	-1.22833
n-Butane	408.2	36.5	-6.88709	1.15157	-1.99873	-3.13003
n-Heptane	540.3	27.4	-7.67468	1.37068	-3.53620	-3.20243
Iso-octane	544.0	25.7	-7.38890	1.25294	-3.16606	-2.22001
Toluene	591.8	41.0	-7.28607	1.38091	-2.83433	-2.79168
Ethylbenzene	617.2	36.0	-7.48645	1.45488	-3.37538	-2.23048
Ethanol	513.9	61.4	-8.51838	0.34163	-5.73683	8.32581

A.4 Vapour Pressure

The vapour pressure of the fuel is calculated in real time by the LabView program to ensure that the bomb temperature is high enough to avoid condensation of the fuel (see Section 3.8.1). An equation from Reid et al. (1987) is used along with the critical temperature and pressure of the fuel and the coefficients given in Table A.4.

$$a = 1 - \frac{T}{T_c}$$

$$p_{vp} = p_c \times \exp\left((1-a)^{-1}\left(Aa + Ba^{1.5} + Ca^3 + Da^6\right)\right)$$

For a temperature in Kelvin this gives the vapour pressure in bar.

Table A.5: Thermodynamic data from Daubert and Danner (1997).

Fuel	H (MJ kmol^{-1})	G (MJ kmol^{-1})	S (kJ kmol^{-1} K^{-1})
Methane	-74.52	-50.49	186.27
n-Butane	-125.79	-16.70	309.91
n-Heptane	-187.65	8.165	427.98
Iso-octane	-224.01	13.93	422.96
Toluene	50.17	122.20	320.99
Ethylbenzene	29.92	130.73	360.63
Ethanol	-234.95	-167.85	280.64

Table A.6: Manufacturer and minimum purity of fuels tested.

Fuel	Minimum Purity (%)	Manufacturer
Methane	99.5	BOC
n-Butane	99.0	BOC
n-Heptane	99	Fisher Scientific
Iso-octane	99.75	Chevron Phillips
Toluene	99.8	Fisher Scientific
Ethylbenzene	99.80	Acros Organics
Ethanol	99.86	Hayman

A.5 Thermodynamic Properties

The enthalpy of formation, Gibbs energy of formation and absolute entropy are required for the BOMB program (see Section 4.3.1.1). These are found from Daubert and Danner (1997) and are given in Table A.5.

A.6 Fuel Specifications

Gaseous fuels were supplied in cylinders. Liquid fuels were kept in dark, dry conditions. The manufacturers and purities are given in Table A.6.